Damage mechanics of composites under fatigue loads

Master Thesis

by

René Rieser, BSc

conducted at

Material Science and Testing of Polymers at

Montanuniversität Leoben, Austria

supervision: Dipl.-Ing. Dr.mont. Steffen Stelzer

appraisal: Univ.-Prof. Dipl.-Ing. Dr.mont Gerald Pinter

Leoben, June 2016

AFFIDAVIT

I declare in lieu of oath, that I wrote this thesis and performed the associated research myself, using only literature cited in this volume.

EIDESSTATTLICHE ERKLÄRUNG

Ich erkläre an Eides statt, dass ich diese Arbeit selbstständig verfasst, andere als die angegebenen Quellen und Hilfsmittel nicht benutzt und mich auch sonst keiner unerlaubter Hilfsmittel bedient habe.

LEOBEN, June 2016 **(René Rieser)**

ACKNOWLEDGMENTS

I want to express my sincere appreciation to my supervisor Dipl.-Ing. Dr. Steffen Stelzer, for his valuable support during the entire time of this study. His enthusiasm for fibre-reinforced polymers and his thirst for knowledge is a source of motivation. I am very grateful to Univ.-Prof. Dipl.-Ing. Dr.mont. Gerald Pinter (Montanuniversität Leoben) to make it possible to conduct this study. The pleasant working environments that he creates, makes possible, the achievement of good results.

Many thanks to Ass.Prof. Dipl.-Ing. Dr. mont. Ewald Fauster and Univ-Prof. Dr. Ing. Ralf Schledjewski for the possibility of the laminate production, which was essential for this work, since the reproducibility of the results is linked to a good quality of the manufactured plates.

Special thanks go to all NDT-specialists who investigated the selected specimens quick and in such an uncomplicated way. Thank you!

I do not want to miss the opportunity to thank my family for their incredible support in the recent years.

ABSTRACT

This study investigates the fatigue behaviour of glass fibre reinforced polymer (GFRP) laminates. Unidirectional layups (UD), biaxial layups from ±15° to ±75° in 15° steps and a 0° dominated multiaxial layup were manufactured. Specimens were produced with the vacuum pressing technology. Damage evolution was observed in detail during the cyclic tension-tension fatigue test. It was linked to the decreasing cycle-dependent linear-elastic properties. Damage initiation and growth until specimen failure were observed using a camera system and transmitted light. It was found, that some layups do not develop a characteristic damage state (CDS) because delaminations evolved before crack accumulation in the entire specimen. The applied stresses in the fatigue tests were calculated with the classical laminate theory (CLT) and Puck's failure criterion for static loads. It was used to show the unsuitability of a static approach under cyclic loads. Non-destructive testing (NDT) methods were evaluated for their applicability to damage monitoring during fatigue tests.

KURZFASSUNG

Diese Studie untersucht das Ermüdungsverhalten von endlosglasfaserverstärkten Laminaten. Dafür wurden unidirektionale (UD) Lagenaufbauten, bidirektionale Lagenaufbauten mit einen Winkel von ±15° bis ±75° in 15° Schritten hergestellt. Die Schädigungsentwicklung wird während der Ermüdungsversuche mit hoher Detailauflösung aufgezeichnet und mit den abnehmenden linear-elastischen Eigenschaften in Verbindung gebracht. Ergebnisse der Untersuchungen sind unter anderem die Visualisierung des Risswachstums und der Schädigungsentwicklung, die letztlich zum Versagen des Prüfkörpers führten. Die Studie zeigt, dass neben Schädigungsmechanismen, die zur Rissdichtensättigung (characteristic damage state CDS) führen, auch rein delaminations-basierte Schädigungsmechanismen existieren. Dabei entstehen Delaminationen bevor sich Risse im gesamten Bauteil ausbreiten können. Die maximalen Spannungen in den Ermüdungsversuchen wurden mit Hilfe der klassischen Laminattheorie (classical laminate theory CLT) errechnet, damit ein definierter Reservefaktor für statische Lasten nach Puck erreicht wird. Damit soll der Fehler gezeigt werden, der entstehen könnte, wenn ein Bauteil dynamisch beansprucht wird, das rein statisch ausgelegt ist. Des Weiteren wurden zerstörungsfreie Prüfmethoden (ZfP, non-destructive testing NDT) bezüglich ihrer Eignung für online Schädigungsbeurteilung bei Ermüdungsversuchen bewertet.

TABLE OF CONTENTS

SYMBOLS AND ABBREVIATIONS

CFRP	Carbon fibre reinforced plastics
CDS	Characteristic damage state
CLD	Constant life diagram
CLT	Classical laminate theory
CT	Computed tomography
DIC	Digital image correlation
FF	Fibre failure
FRP	Fibre reinforced polymers
GFRP	Glass fibre reinforced plastics
HM	High modulus
HT	High tenacity
IM	Intermediate modulus
IFF	Inter fibre failure
NDT	Non-destructive testing
PAN	Polyacrylonitrile
RF	Factor of safety for static loads
RTM	Resin transfer molding
UCS	Ultimate compression strength
UHM	Ultra-high modulus
UT	Ultrasonic testing
UTS	Ultimate tensile strength
VI	Vacuum infusion technology

Designation	**Unit**	**Description**
N	[cylces]	Number of applied cycles in fatigue test
E_{11}	[MPa]	Modulus of elasticity according to ISO 527-4
$E_{11,rel,ct}$	[%]	Relative modulus form cyclic tensile tests
R	[-]	Ratio of minimum force to maximum force in a cyclic test
$\alpha_{\|\|f}$	[K^{-1}]	Thermal fibre expansion
ε_{11}	[%]	Strain longitudinal to load direction
ε_{22}	[%]	Strain transversal to load direction
ε_k	[%]	Strain longitudinal to load direction, measured by the Keyence camera system
$\varepsilon_{piston,korr}$	[%]	Calibrated piston strain
σ_{11}	[MPa]	Normal stress longitudinal to direction of the applied load
σ_{22}	[MPa]	Normal stress transversal to direction of the applied load
σ_{max}	[MPa]	Nominal maximum stress, highest stress in a cyclic test
τ	[MPa]	Shear stress
ω	[°]	Angle between fibre and load direction
$\Delta\omega$	[°]	Angle deviation

CONTENTS OF GRAPHS

1 INTRODUCTION AND OBJECTIVES

Composite materials have received much attention in recent years. Their promising mechanical properties are offering important economic benefits. Since the BMW AG introduced, as a forerunner of the automotive industry, the i3-series and the i8-series, carbon composites have arrived in the large-scale production of the automotive industry. Even apart prestigious projects as the BMW i-series, carbon composites are applied to components of high-price standard vehicles like the BMW 7-series (BMW Group 6/10/2015). The global carbon composite market showed a strong growth with a turnover of 16.6 billion US$ in 2014 and an output of 83 thousand tonnes. The market is driven by aerospace, wind energy industry and the increasing use of CFRP in automotive industry. The growth rate is expected to be 11% for the next years (Carbon Composites e.V. 2015). Besides carbon fibre reinforced polymers (CFRP), glass fibre reinforced polymers (GFRP) are from strong economic interest as well. The European CFRP market showed a continuous growth of 2.5% in 2015 with an output of 1069 million tonnes, which is the largest volume of the last eight years. The GFRP market is driven by the transport industry and construction industry (AVK - Industrievereinigung Verstärkte Kunststoffe e.V. 2015). Due to the widespread use of composites, it is essential to know about their behaviour under cyclic conditions.

Much research in the field of GFRP and CFRP has been done in recent years. Quaresimin et al. focused on damage evolution under multiaxial stress states (Quaresimin et al. 2014). In their studies, glass fibre reinforced polymers were used, due to their semi-transparency. Using a light source, it was possible to observe crack initiation and growth during fatigue tests. An alternative approach was developed by a research group at the Montanuniversität Leoben (Brunbauer et al. 2014). They presented a test procedure to measure the stiffness degradation during fatigue tests. In another study, they calculated the fatigue stiffness properties of CFRP using cycle-dependent input parameters of unidirectional plies (Brunbauer und Pinter 2015). For an even better understanding of the damage mechanisms, it is required to evaluate the damage evolution during fatigue tests. An effective NDT-method is required for an experimental online damage monitoring. Böhm and Hufenbach compared NDT methods under static loads in 2010; however, their suitability for online damage monitoring during fatigue tests is still unclear.

In this study, GFRP laminates with different fibre angles were tested under cyclic loads in cyclic tension-tension tests. It focuses on GFRP, due to the possibility of the damage

observation in an adapted way of the transmitted light approach, as presented in Quaresimin et al. (2014). The used approach aims to achieve a detailed observation of the damage evolution in high resolution. Several laminates with unidirectional and biaxial layups $[\Theta/-\Theta]_s$ were studied to identify different damage mechanisms. Since the fatigue life depends on the applied stress, a maximum stress was needed to be determined for each layup. In this study, the fatigue load levels were calculated using the static failure criteria after Puck (1997), so that the factor of safety equalled two for each laminate. A static approach was used, because the fatigue lifetime estimation is a recent research topic and static failure criteria are implemented in common composite calculation software. Thus, this study shows the differences in the fatigue behaviours of statically equivalent loaded laminates.

Because the transmitted light damage monitoring approach could not be applied to CFRP. State of the art NDT methods were checked for the suitability of damage monitoring during fatigue tests. Therefore, six specimens with a multiaxial stacking were tested in cyclic tension-tension tests. The tests were stopped at different damage states, to compare the NDT-methods.

2 FUNDAMENTALS

2.1 Continuously fibre reinforced polymers

The overall aim of composite materials is to combine various materials in order to achieve improved properties and synergies. In the case of fibre-reinforced polymers (FRP), the material behaviour gets anisotropic due to the fibre orientation within the polymeric matrix (Ehrenstein 2006). G. Slayter found out that composite materials absorb greater stresses than the failure stress of the weakest component and the stronger component take a higher proportion of strength of its theoretical strength (G. Slayter 1962).

The fibre orientation determines the mechanical properties. In the case of in load direction oriented fibres, the strengths of fibres and matrix are like a parallel connection of fibre- and matrix-strengths. In the case of transversal to load direction oriented fibres, the strengths of fibres and matrix are like a serial connection, so that the ultimate tensile strength of the composite equals approximately the matrix's strength. **Fig. 2.1** illustrates the angle-dependent ultimate tensile strength. The different mechanical properties of the fibre and matrix lead to a complex stress state, which is analysed by micromechanical models (Ehrenstein 2006).

Laminates are usually built by using a multiaxial layout. Multiaxial layouts have useful mechanical properties in more than one direction. The layout should always be symmetrical. Positive off-axis plies should be compensated with negative off-axis plies, which have the same but negative angle. To avoid undesirable deformations under load and through residual stresses, it is important to choose compatible materials, to prevent a weak fibre-matrix bounding which eases damage initiation, (Ehrenstein 2006).

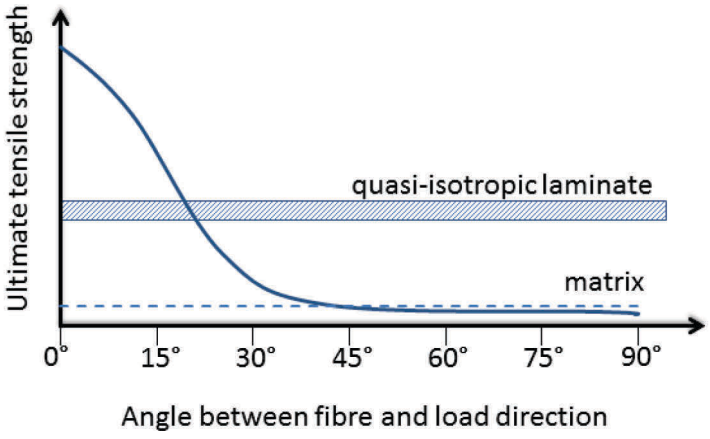

Fig. 2.1: Schematic representation of the fibre orientation dependency of the ultimate tensile strength according to (Ehrenstein 2006).

The polymer matrix

The main purpose of a polymer matrix is to preserve, initiate and transfer loads into fibres. It additionally fixes the fibre in its position and keeps the shape of the component. This requires a strong fibre-matrix bounding. A differentiation is made between thermoplastic and resin based matrix systems. The most frequent resins-matrix-systems are unsaturated polyester resins, vinyl ester resins and epoxy resins. Epoxy resins need a sufficient number of epoxide groups for the curing process. Epoxide groups are functional groups, which allow the chemical reaction with the hardener. Epoxy resins have excellent mechanical properties. Therefore, they are applicable for high-quality fibres, like carbon fibres. The chemical resistance depends on the hardener (Henning und Moeller 2011).

Reinforcement fibres

Reinforcement fibres have a significant influence on the composites material properties, like stiffness, strength, impact resistance and creep. For most technical issues carbon, aramid and glass fibres are appreciable due to their high specific mechanical properties and their outstanding potential for lightweight constructions. There are different technical approaches for the use of fibres in a composite, as shown in **Fig. 2.2** (Henning und Moeller 2011).

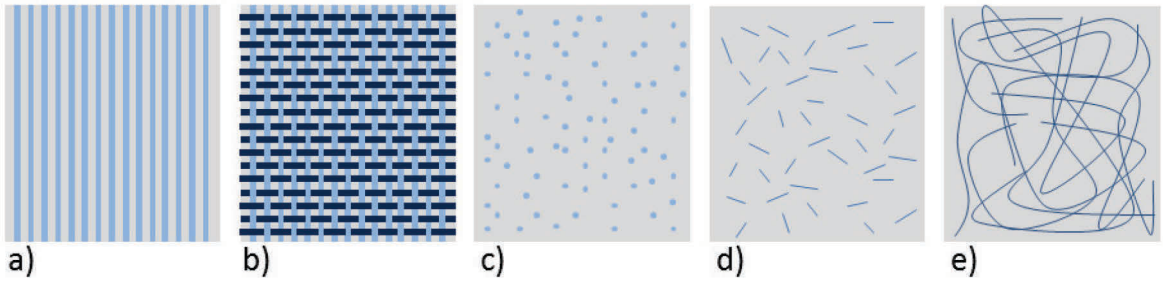

Fig. 2.2: Schematic representation of different types of reinforced composites a) unidirectional bounded fabric; b) woven fabric; c) particle; d) short fibres; e) long fibres according to Henning und Moeller (2011).

Glass fibres

Glass fibres are synthetic, inorganic fibres. Their high strength results from the strong covalent bonds between silicon and oxygen. Based on the amorphous structure without orientation, glass fibres have isotropic mechanical properties. The diameter range is between 3.5 and 24 microns. The most important advantage of glass fibres, compared to other fibres, is a low price combined with suitable mechanical properties. Those are very

high longitudinal tensile strength and high longitudinal compressive strength. Air-void free glass fibre laminates are semi-transparent, since the refractive index of glass is similar to transparent resin. A disadvantage is the low Young's modulus compared to high modulus fibres as carbon fibres. Hence, glass fibres are not applicable for some high performance applications. The elastic modulus of the composite equals approximately to the half of the fibres elastic modulus. However, there are applications where a low elastic modulus, compared to carbon fibres, and a large linear-elastic deformability is desired (Schürmann 2007).

Carbon fibres

Carbon fibres have extremely high strengths and stiffnesses and low ultimate tensile strains; the diameter range is between 5 and 10 microns. Raw materials are cellulose and polyacrylonitrile (PAN). PAN is the standard raw material for the C-fibre production today. The elastic modulus and ultimate tensile strength can vary within wide ranges. They depend on the degree of fibres that are oriented in load direction and on fibre imperfections. Fibre imperfections arise during the manufacturing process. Unlike glass fibres are carbon fibres highly anisotropic. Hence, there is even a slightly negative thermal expansion in fibre direction ($\alpha_{||f} = -0{,}1 * 10^{-6}\, K^1\ till - 1{,}5 * 10^{-6}\, K^1$). They have, in contrast to polymers, a progressive stress-strain-behaviour; the elastic modulus increases with load. For carbon fibres, there is a classification to make. One distinguishes between high tenacity (HT), intermediate modulus (IM), high modulus (HM) and ultra-high modulus fibres (UHM). An outstanding characteristic is the good fatigue behaviour of carbon fibres, compared with traditional materials such as steel and aluminium (Ehrenstein 2006).

To reprocess carbon fibres to textile semi-finished products, such as woven fabrics or unidirectional bounded fabrics, the filaments are combined to rovings. A designation of 3K for example, characterizes a roving with 3000 filaments. 1K, 3K, 6K, 12K and 24K rovings are conventionally available. For cost sensitive areas, such as the automotive industry, usually 12K or 24K types are used. Due to the increasing productivity of those types, large-scale production is feasible (Henning und Moeller 2011).

The classical laminate theory (CLT)

The classical laminate theory describes the stress state and the strain state of each layer within a laminate. For the validity of the theory, several assumptions must be met. The laminate thickness ought to be constant and small, compared to the main dimensions. Each individual layer should to be plane and parallel to the laminates central plane. The individual layers have to stick ideally together, so that the composite deforms equally under load and the cross-sections remain plane. This results in different cross-contractions of the individual laminas, which lead to interlaminar stresses. However, the CLT is well suited for lamina stress calculation. Therefore, it is necessary to know the number of plies, the fibre orientation, the fibre volume ratio, the ply thickness, the ultimate tensile strength (UTS) and ultimate compression strength (UCS), the Young's and shear modulus and the Poisson's ratio. **Fig. 2.3** illustrates the different lamina stresses according to the different lamina stiffnesses. However the different stress levels in the laminate do not imply that shear stresses between the layers occur, but they result from the laminates cross-section that remains plane and perpendicular to its central plane (Schürmann 2007).

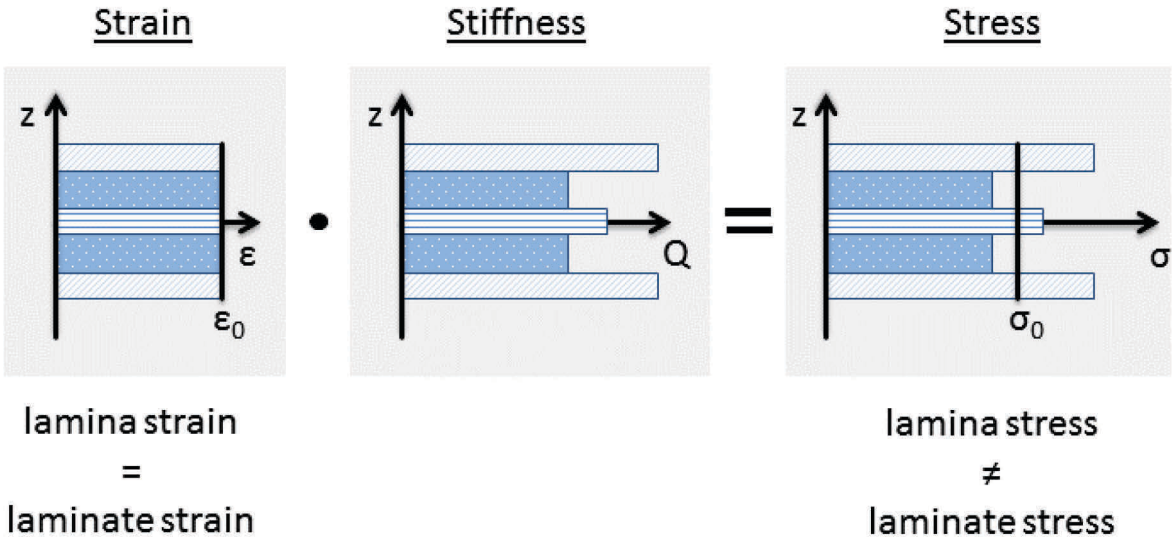

Fig. 2.3: Comparison of the laminate strain and stress to the local lamina strain and stress according to Schürmann (2007) and Moser (1992).

2.2 Fatigue

Fatigue can be defined as the damage and the failure of a material or component under time-dependent stress and cyclic stress. Failure often occurs at stress levels which are below the static ultimate stress. The description of the fatigue strength is a multi-parameter problem. The parameters usually cannot be decoupled. This problem leads to large scattering in investigations, and hampers the desired precise of life predictions. For fatigue investigations, there is a classification to make. One distinguishes between cyclic compression-compression tests, cyclic tension-compression tests and cyclic tension-tension tests (Radaj 2003). **Fig. 2.4** illustrates this differentiation. It is essential to note, that there are different shapes and dimensions for the test specimens to be used, according to the chosen test method.

International Organisation for Standardization 13003 defines the procedures for fatigue testing of fibre-reinforced plastic composites under cyclic loadings. It cites the main terms, designations and defines the test procedures such as the test frequency. To avoid an excessive rise in the specimen temperature through self-generated heating, it is essential to choose an appropriate test frequency (ISO 13003:2003 (EN)).

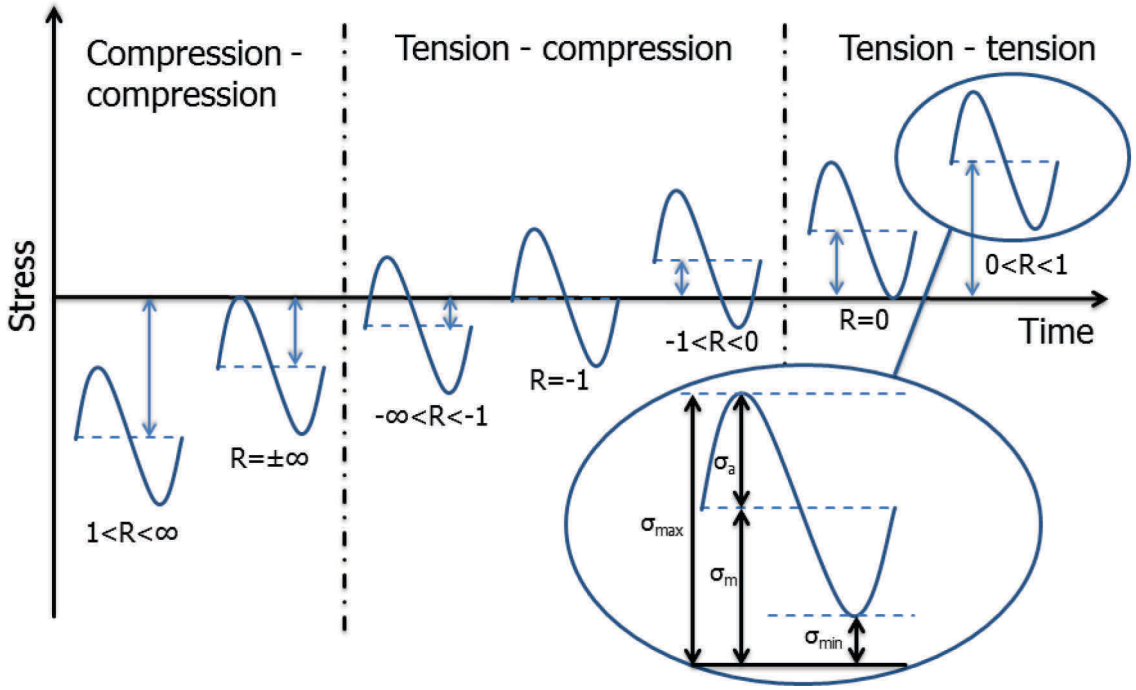

Fig. 2.4: Stress ranges under fatigue loads according to (Radaj 2003).

Material behaviour of homogeneous materials can be predicted by combining disciplines of mechanics, mathematics, physics and empiric investigations. For composite materials, it is much more challenging. Their material behaviour is per definition inhomogeneous. Since composite materials are also anisotropic, their properties such as stiffness and strength become a tensor array of independent properties. These can change during cyclic mechanical loading or due to physical aging or chemical aging. However, composite materials show a better fatigue resistance compared to any other class of materials. Hence, it is important to understand the damage evolution in composites under fatigue loads to get the most out of it (Reifsnider 1991).

2.2.1 Theories describing composite fatigue

August Wöhler created the basis for fatigue testing. His approach is well known as Wöhler-lines or S-N curves. Wöhler investigated un-notched and notched specimens under cyclic loads. He performed tests with constant mean stress until the occurrence of a defined failure criterion. Defined failure criterions are specimen fracture or a defined strength reduction (Radaj 2003). S-N curves are a common way to describe the fatigue behaviour of composites. The testing effort is moderate but it is impossible to account for some relationships between damage events in the fatigue process (Reifsnider 1991). To increase the information value, it is necessary to perform several tests at different mean stresses. The life locus is then defined by the specimen failures at different mean stresses. Failure prior to 10^6 cycles is not unusual for composites, even at stress levels that are wildly under the static ultimate strength (Reifsnider 1991).

In International Organisation for Standardization 13003:2003 Wöhler plots, respectively S-N plots, are defined as a test method for composite. S-N diagrams are usually plotted for constant R-values. The definition of R can be seen in **Eq. 2.1**. Since the S parameter is used as a generic term, it is defined as stress or strain. It depends on the control mode (Vassilopoulos 2010).

$$R = \frac{S_{min}}{S_{max}} \tag{2.1}$$

Haigh-diagram or constant life diagram (CLD)

The Haigh-diagram, also known as CLD presents the influence of the stress ratio and the mean stress on the fatigue behaviour. For metal materials, it can be enhanced to a long-life-fatigue-strength-chart and short-life-fatigue-strength-chart. Thus, it presents the entire information's of Wöhler-lines for different stress states (Haibach 2006).

Much research on this subject was done by Vassilopoulos in recent years. He has focused on the fatigue life prediction of composites and used the CLDs to describe the fatigue behaviour. **Fig. 2.5** shows the schematic concept for the construction of a constant life diagram. In this example, three fatigue tests for each R-value were performed at different stress levels until fatigue failure. According to the different ultimate numbers of cycles for each test, an interpolation of the collected data is necessary to combine the data in a CLD for constant numbers of cycles. CLD helps in the derivation of S-N curves, thus it is a good instrument for fatigue data analysis. The constant life lines are not mandatory linear, they can be as well asymmetric and piecewise nonlinear predicted (Vassilopoulos 2010).

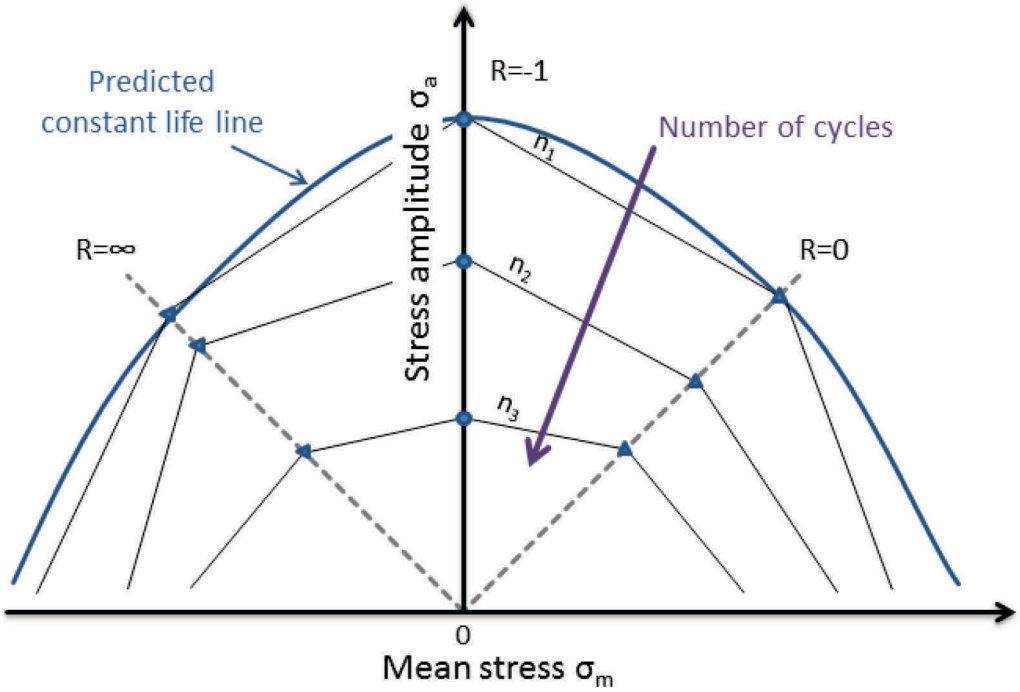

Fig. 2.5: Construction of a constant life diagram according to (Vassilopoulos 2010).

Hysteresis evaluation

Approaches like hysteresis evaluation are more informative than common S-N curves. The shape and the slope of the hysteresis provide information about the inner state of the specimen (Ehrenstein 1995). Since polymers and fibre reinforced polymers have viscoelastic material properties, there is a phase shift between strain and stress under cyclic loads (see **Fig. 2.6a**). Time-dependent stresses and strains are plotted in a strain-stress diagram. This generates a hysteresis that is characteristic for the inner state of the material (see **Fig. 2.6b**). In terms of the hysteresis evaluation, a secant modulus E_s and a dynamic modulus E_{dyn} are distinguished. Both moduli are decreasing due to cyclic loads. The stiffness reduction and a change in the mechanical damping have influence on the hysteresis shape and position. The secant modulus indicates viscoelastic effects and damage accumulation, the dynamic modulus indicates damage accumulation. A hysteresis shifting identifies in general damage evolution. Hence, it is for laminates a suitable approach for the determination of limits of applicability under fatigue loads (Ehrenstein 1995).

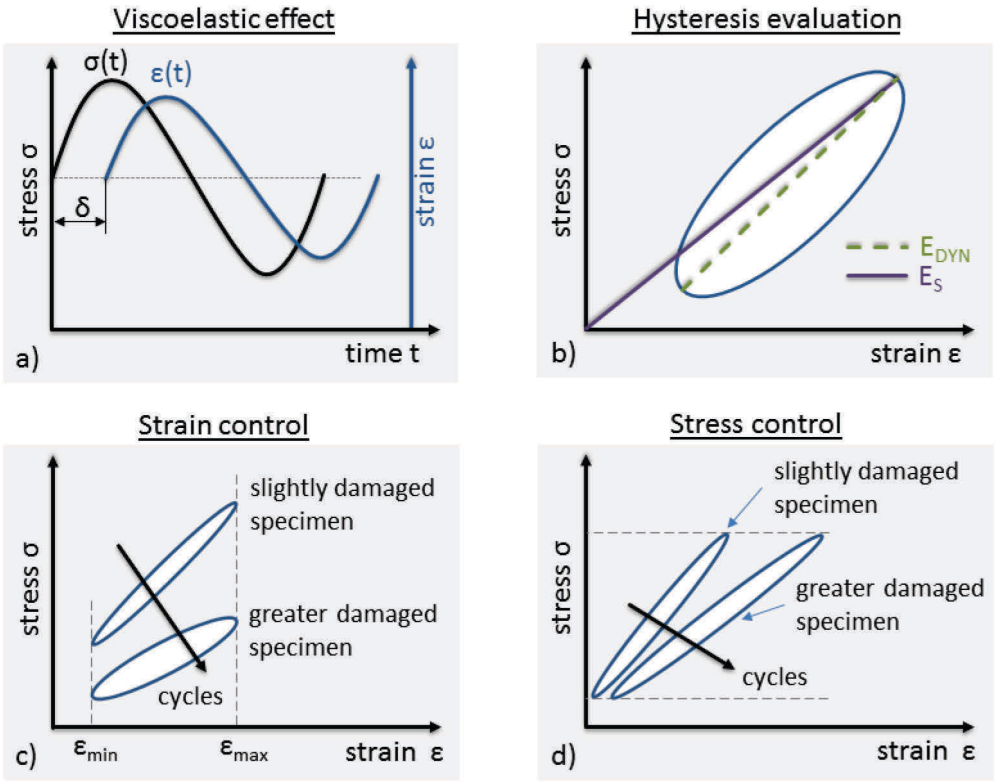

Fig. 2.6: Concept of hysteresis evaluation according to Ehrenstein (1995) and Reifsnider (1991); a) phase shift between stress and strain; b) hysteresis in stress-strain diagram; c) and d) display the differences between strain control and stress control in terms of hysteresis evaluation.

The occurrence of damage in a composite laminate causes changes in the load-carrying ability near the damaged regions. For fatigue investigations in laboratories, there are classifications to make. One distinguishes between strain-controlled tests and load-controlled tests. In strain-controlled tests, the strain R-value remains constant. The associated stiffness reduction occurs as fatigue damage develops; less load is required to reach the strain limits. Thus, the hysteresis loops reflect the changes in the strain-stress behaviour during the test, as indicated in **Fig. 2.6c**. Load-controlled tests are often performed in laboratories. For this method, it is not necessary to measure the specimens strain. **Fig. 2.6d** displays the differences between strain-controlled tests and load-controlled tests in a stress-strain diagram. Damage development is limited in strain-controlled conditions; the introduced load reduces during the test due to a lower required load, which is necessary to reach the strain-value in the damaged specimen. This leads apparently to greater fatigue life of specimens, as evident by **Fig. 2.7**. Hence, a second failure-criterion like a defined stiffness reduction is recommended (Reifsnider 1991).

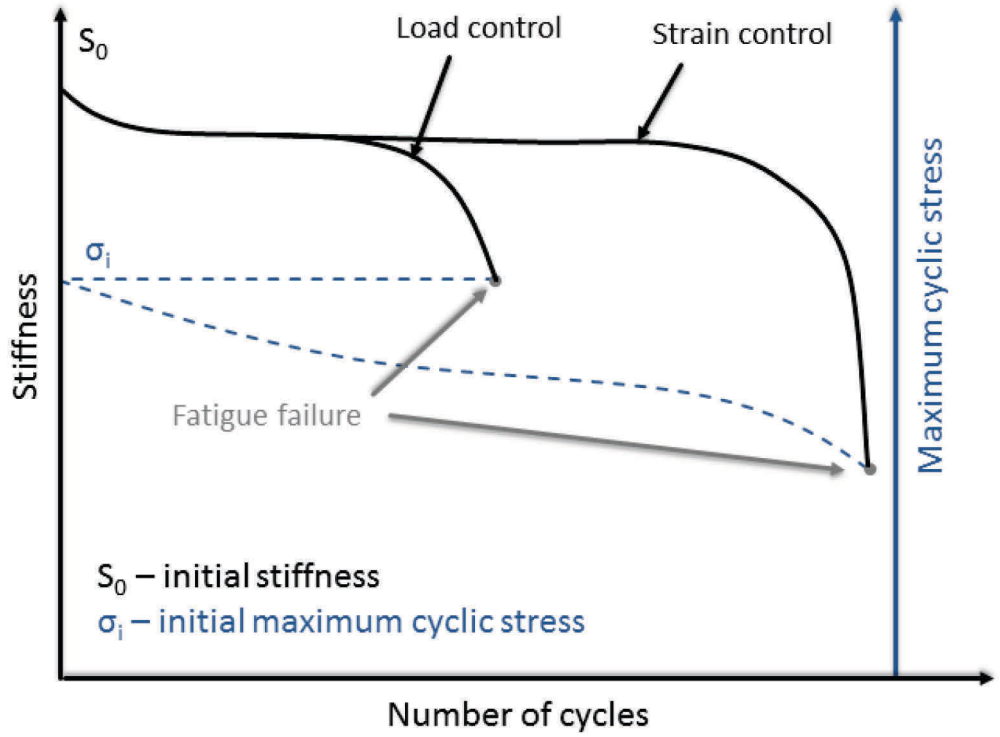

Fig. 2.7: Stiffness reduction during cyclic loading as influenced by test control modes according to Reifsnider (1991)

2.2.2 Damage mechanisms

Reifsnider defines "fatigue effect" in general terms as the reduction of remaining strength or stiffness, and possible failure, after a finite number of applied load cycles. Since load amplitudes are smaller, than the required load for failure under quasi-static conditions, fatigue damage lowers the strength of the component. This cycle-dependent behaviour is caused by some non-conservative deformation that changes the ability to respond to continuing loads. The dissipated energy, which is responsible for the changes in the internal nature of the material, is the driving force for the development of micro-cracks and other internal processes. For composite materials, it is common to speak of damage accumulation instead of damage propagation. Because it is uncommon for a single crack to dominate the damage development. The anisotropy of the laminate and the complex stress state has a major influence on the damage development (Reifsnider 1991). **Fig. 2.8** illustrates the subject of damage mechanics. It shows the relationship between the load history and the damage mechanism. The increasing damage induces the stiffness reduction during the fatigue life, as displayed in **Fig. 2.7**.

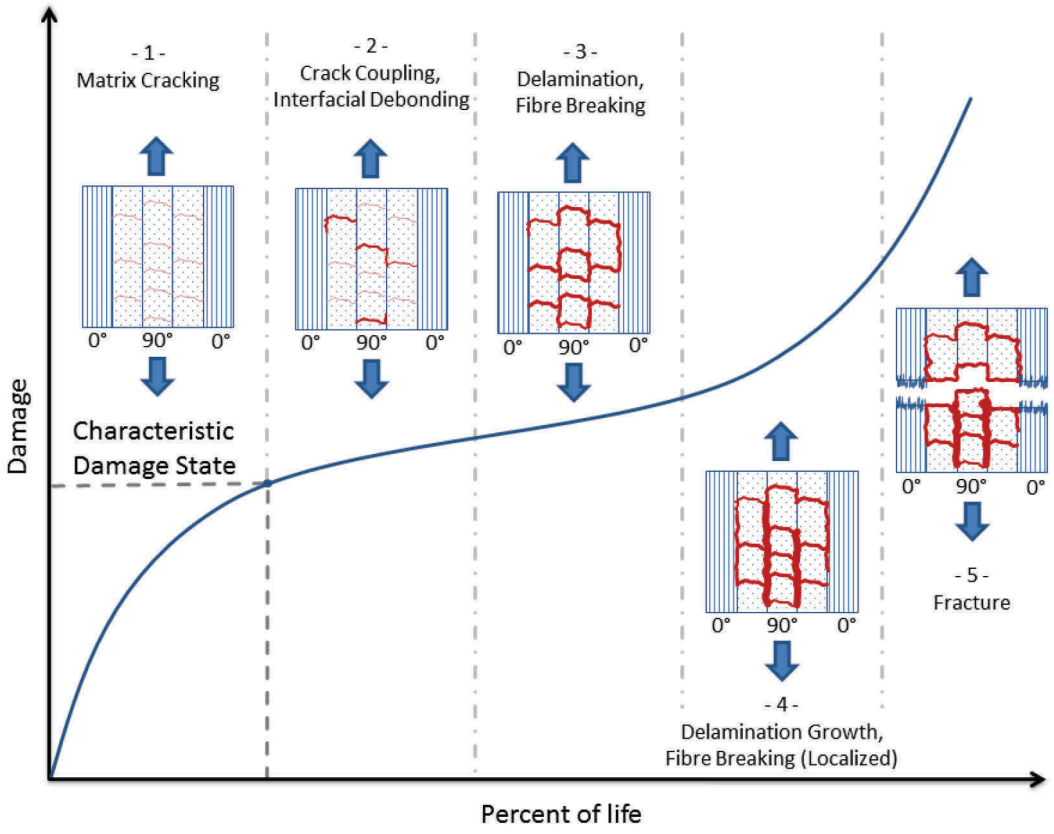

Fig. 2.8: Damage development during the fatigue life of a composite according to Reifsnider (1991).

Primary cracks in off-axis plies initiate a damage process, as shown in **Fig. 2.9**. Cracks occur in composites with brittle matrix materials and composites with ductile matrix materials. The experimental detection of initiated transverse cracks is difficult in composite laminates. It has little relevance in the engineering sense; a small number of micro-cracks will not cause a large reduction in the laminates stiffness. However, these cracks change the stress state in the laminate and those cracks are part of an irreversible sequence of damage events. Under quasi-static or cyclic loads, a saturation of cracks and a stable pattern of regularly spaced cracks can be observed. Reifsnider established this generic pattern of cracks 1977 as the "characteristic damage state" (CDS). The CDS and the shear lag concept for stress distribution within the laminate is detailed in **Fig. 2.9**. A defined stress level is required for crack accumulation, so the CDS is a well-defined laminate property. It depends on the properties of the individual layers, the stacking sequence on the laminate and of the layer thickness. Hence, it is important for the analysis of a damage development process. The CDS is the beginning of a sequence of critical damage processes, which lead to a significant reduction of the stiffness, strength and life of a component (Reifsnider 1991).

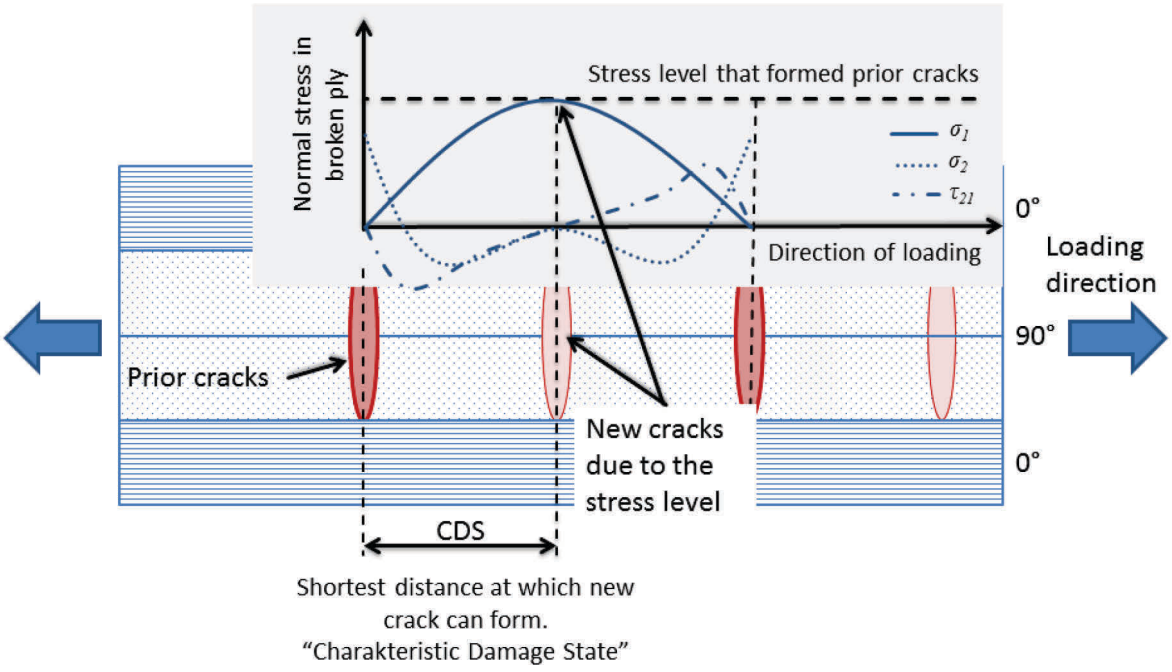

Fig. 2.9: Illustration of CDS and the shear lag concept for stress distribution within a laminate according to Reifsnider (1991) and Puck (1997).

Reifsnider defined the "mechanics of damage development" as: *"those philosophies and analytical formulations based on principles of mechanics which are associated with states of stress and states of material that are peculiar to high-modulus fibrous composite laminates which endure loading histories known to cause changes in laminate strength, stiffness and life because of micro-failure events collectively called "damage"".* Micro-failure events are micro-cracks for instance. The occurrence of micro-cracks is a result of energy introduction into the material due to non-conservative deformation. It cannot be stored as strain energy under cyclic loads. Any non-conservative material response contributes a local load-history near a crack tip. This could cause progressive growth of cracks that change the associated state of the material and state of stress. To predict the remaining strength after a number of cycles, it is necessary to know the damage development in the material for the expected failure mode. A rational approach must include micro-mechanical as well as macro-mechanical information. The rate of development on micro-mechanical models is limited by the availability of experimental methods and experimental data (Reifsnider 1991).

2.2.3 Damage criteria

Puck's damage criterion is based on physics and an advancement of Hashin's approach for quasi-static failure prediction. For the Puck's theory, there is a significant classification to make. One distinguishes between inter fibre failure (IFF) and fibre failure (FF). Those have an entirely different effect and type of fracture. Evaluating the damage potential of IFF modes, it is essential to distinguish between the relative harmless transverse tension stress, as illustrated in **Fig. 2.10** (Mode A) , and harmful transverse compression stress due to its explosive effect (Mode C). A summary of the failure modes according to Puck can be found in **Fig. 2.10**. Crack formation caused by IFF results in a gradual stiffness reduction instead of sudden component fracture. Cracks in off axis plies are stopped by the adjacent ply because it requires more energy for a fibre failure. However, they cause notch stresses that have a negative impact under fatigue loads (Puck 1997).

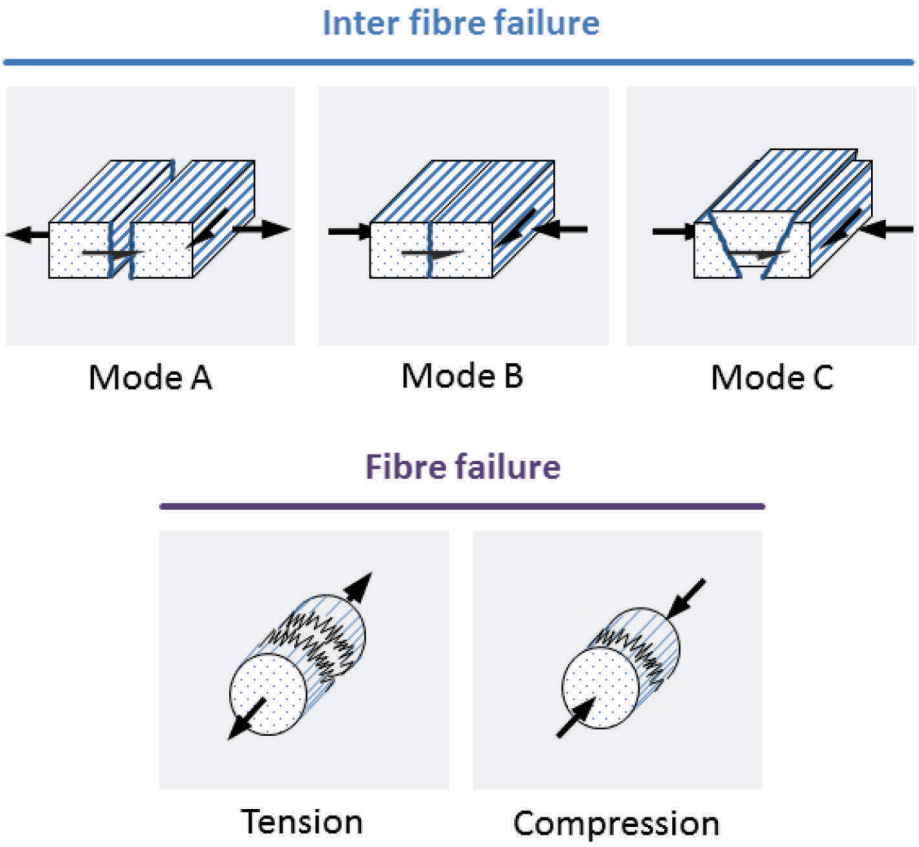

Fig. 2.10: Distinction of damage criteria in composite laminates referring to Puck (1997).

It is based on Mohr's fracture hypothesis, which is a physical approach. Normal stresses σ and shear stresses τ are considered (**Eq. 2.2**). Material properties are tensile and compression strengths R_σ and shear strengths R_τ, measured in quasi-static tension and compression tests (Puck 1997).

$$F(\sigma, \tau, R_\sigma, R_\tau) \leq 1 \quad OR \quad \geq 1 \tag{2.2}$$

In the case of, the failure criterion is less or equal one, the achieved normal stresses σ and shear stresses τ at specimen failure are lower than the assumed stresses. Specimen failure occurs bevor the assumed stresses are achieved. For material design, it is necessary to proof evidence of safety. The factor of safety (RF) is a positive factor. The assumed stresses can be increased by the factor of safety. Thus, the failure criterion equals one. RF equals one signifies a stress-level that barley leads to failure of the specimen or component (**Eq. 2.3**) (Puck 1997).

$$RF(\sigma, \tau, R_\sigma, R_\tau) = 1 \tag{2.3}$$

For residual stress free specimens or components, the factor of safety is clearly defined, as presented in **Eq. 2.4**.

$$RF(\sigma, \tau, R_\sigma, R_\tau) = \frac{length\ of\ the\ stress\ vector\ that\ leads\ to\ failure}{length\ of\ the\ stress\ vector\ of\ the\ present\ stresses} \tag{2.4}$$

The advantage of the Puck's failure criterion is the failure-mode differentiation, as mentioned before. The envelope curve of the stress-vectors that lead to failure is similar to the shape of a cigar. The so-called puck-cigar is illustrated in **Fig. 2.11** (Puck, 1997).

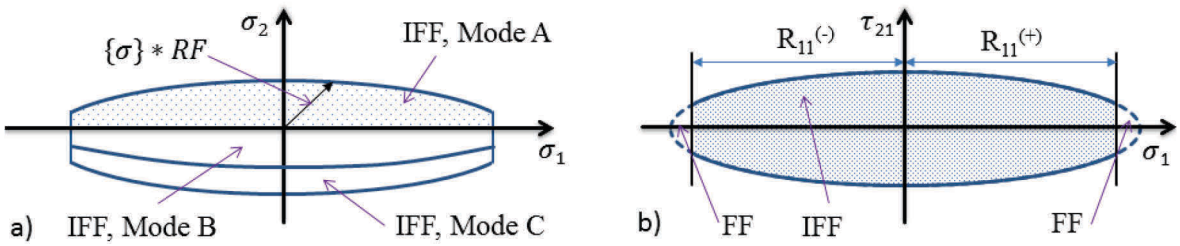

Fig. 2.11: 2D fracture analysis using the Pucks criterion. A differentiation is made between inter fibre failure (IFF) modes a) and between fibre failure (FF) and IFF b), according to Puck (1997).

2.3 Non-destructive testing

The aim of non-destructive testing (NDT) is to determine information about the state of material and to describe the damage state of a component. Since polymers, especially fibre-reinforced polymers, have various failure modes and different physical properties, many NDT-methods evolved in the past decades. There are differences in technical maturity, resolution, performance and investment cost. NDT-methods are distinguished between the coupling methods. One distinguishes between contact / contactless and one side / on both sides access. NDT methods have no damaging effect on the considered specimen or component. Thus, costs can be saved because components can still be used after the assessment of their properties. For the aerospace industry, it is important that components can be replaced before failure. The power generation and automotive industry have also a special interest in NDT-methods for lifetime-predictions and quality assurances. NDT is mostly linked with an indirect measuring method. The desired characteristic value is recalculated; thus, the quality of the characterization depends on the response sensitivity of the measured variable. The NDT principle is indicated in **Fig. 2.12** (Grellmann und Seidler 2011). NDT has received much attention in recent years and numerous publication were presented (Busse 2007; Döring 2011; Hillger 2014; Helfen 2014; Rheinfurth et al. 2011). This had raised the question of whether it is possible to establish an online damage monitoring system with commercially available NDT systems. The aim of the NDT part of this study is to compare performance of those NDT systems.

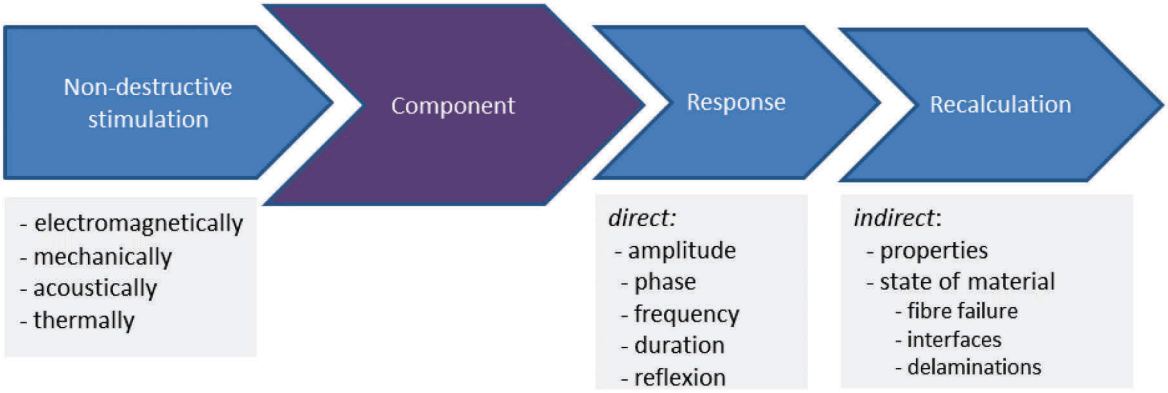

Fig. 2.12: Principle of non-destructive testing methods according to Grellmann and Seidler (2011).

Applicability of NDT methods for damage assessment

The evaluation of the Modulus of Elasticity during fatigue tests can be used for a qualitative assessment of damage events. It is a contacting NDT method, which correlates stiffness degradation with damage development. It is difficult to identify a specific damage mechanism, but it is possible to verify its effect (Brunbauer and Pinter 2015). The quality of the results is linked to the accuracy of the strain measurement. Brunbauer and Pinter (2014) recommended to combine the piston displacement with optical measurements, to enable an evaluation of the entire fatigue test.

Ultrasonic inspections of components with fatigue damage can identify delaminations, matrix cracks and other defects, due to the attenuation of the acoustic waves. In addition to the defect identification, the speed of the acoustic pulses can be used to determine the Young's modulus of a composite (Harris 2003). Rheinfurth et al. (2011) showed even by using air-coupled guided waves, that the change in wave velocity caused by fatigue damage correlates closely with the stiffness degradation of the composite.

The damage assessment in terms of X-ray Computed Tomography (CT) is challenging by using standard X-ray radiographs, due to the low contrast between fatigue-caused damage and the undamaged material. Cracks and delamination are not easily detectable. To enhance this contrast, radio-opaque liquids can be applied, which penetrate into the material. By using a high voltage CT equipped with a high resolution detector, it is possible to detect damage less than 1mm. The degree of resolution is then much higher, compared to ultrasonic C-Scans (Harris 2003).

Thermography is a contactless NDT method that can be used to determine the presence of fabrication defects like large voids and foreign objects. One distinguishes between active thermography and passive thermography. Active thermography can be used during fatigue tests. It identifies damage within the specimen due to the generated internal heat, by using an Infrared-camera. Passive thermography introduces the heat by using an external heat source (Harris 2003). Steinberger et al. (2006) showed for CFRP, that thermography is applicable for fatigue damage assessment.

Ultrasonic testing (UT)

The frequency range for UT varies between 400 kHz and 5 MHz. The lower limit is defined by the resolution; the resolution decreases with decreasing frequency. The upper frequency limit is restricted due to ultrasound damping in the material; the signal damping increases with increasing frequency. For UT, there is a classification to make. One distinguishes between signal coupling techniques and acoustic wave modes. To introduce the ultrasonic signal into the specimen, water, gel, aqualene and air are usually used. There are display options for UT results with different information-values. A-scans provide only 1D information. B-scans make 2D information about the inner state available. Thus, a damage assessment is possible. C-scans provide 3D information about the component's inner state. It is generated from UT, using the pulse-echo method (Grellmann and Seidler 2011).

Water is an excellent coupling medium for UT. It is used to avoid high reflection losses. Water-coupled UT is usually performed in an immersion bath, when components are small and easy to handle. Ultrasonic water jet systems are used for components that are large and hard to handle. Those require double-sided accessibility; ultrasound transmission with sensor and emitter are used. Beside the transmission method, the pulse-echo method is a relevant UT method. It provides information about the damage depth and allows one-sided accessible investigations. The emitter sends tightly focused ultrasonic waves into the specimen, to increase the damage-detection precision. However, the resolution of transmission UT scans are better, compared to pulse-echo investigations, when a significant ultrasound damping occurs in the material (Grellmann and Seidler 2011).

For the sake of coupling-media avoidance, air-ultrasound systems are used. Air-UT systems couple ultrasound directly through air. Moisture adsorption is prevented therefore. The resolution of Air-UT is still limited due to high ultrasound damping in air. The high surface echo loses the defect depth information. The irradiation is perpendicular in normal transmission mode (NTM). The signal level in NTM is quite low. The air-coupled focused slanted transmission mode (FSTM) is an adaption of NTM. Higher signal levels are achieved through the generation of lamb waves. The velocity of lamb waves is higher than the velocity of the speed of sound in air (Grellmann and Seidler 2011). A research group of the University of Stuttgart did much research on this field. They used guided waves for fatigue monitoring in biaxially loaded composite tubes (Rheinfurth et al. 2011).

X-ray Computed Tomography (CT)

X-Ray radiation requires high voltage acceleration of electrons; these electrons collide with high velocity at the anode. This leads to an energy release in terms of a continuous broad band X-ray radiation, when electrons falling from outer shells in inner shells gaps (Grellmann and Seidler 2011).

An X-ray source irradiates a test sample and projects onto a detector. The geometric magnification depends on the ratio of focus-detector distance and focus-sample distance, as illustrated in **Fig. 2.13**. The achieved resolution is linked to the focal spot; the resolution is inversely proportional to the focal spot. The focal spot of micro CT systems is as small as 3 microns. Nano-focus CT systems are used for even higher resolution investigations due its focal spot of 0.2 microns. CT create 3D images of an investigated sample. 2D images are taken systematically from a sample in a slow rotary motion. The 3D model is then derived from the acquired 2D data. The resolution of the 3D model is linked to a voxel size. The 3D model consists of a data set of small cuboids so-called voxels. A voxel has a defined size (voxel size) and a grey value. The voxel resolution (V) depends on the objects diameter or on the size of the region of interest (ROI) and on the detector resolution (see **Eq. 2.5**) (GE Measurement & Control Solutions 2010).

$$V = \frac{(pixel\ size\ of\ the\ detector) * (sample\ diameter)}{detector\ width} \quad [\mu m] \tag{2.5}$$

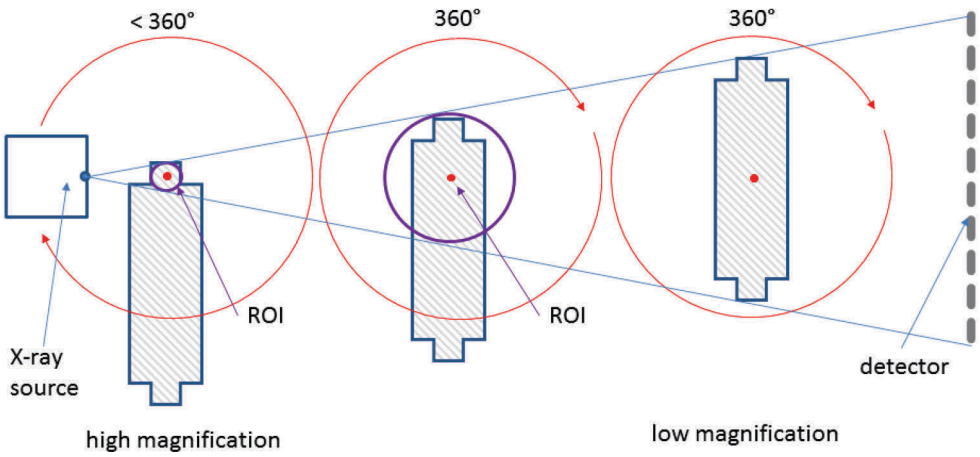

Fig. 2.13: Region of interest (ROI) and geometric magnification in CT (GE Measurement & Control Solutions 2010).

3 MATERIALS AND METHODS

In this study, all specimens were constructed with a unidirectional glass fibre fabric by Lange+Ritter GmbH (Gerlingen, Germany), with an area weight of 220 g/m². The chosen resin system is characterised by a low mix viscosity, curing at room temperature and the ability of laminate demoulding at room temperature without tempering. The EPIKOTE™ Resin MGS® LR160 with curing agent EPIKURE™ MGS® LH160, is approved for aerospace applications after tempering at 80°C for 15h. Specimens were finally produced with the vacuum pressing technology, due to the high air-void content in laminates that were produced with the vacuum infusion technology.

3.1 Test specimen production

Stacking sequences were chosen as detailed in **Table 3.1**. The bidirectional laminates were produced to investigate the off-axis-angle dependency in terms of fatigue. 0° dominated multiaxial stack were produced to compare common non-destructive testing methods. It was antisymmetrical due to a mistake in the stack laying process.

Table 3.1: Name and stacking sequence of the preforms for specimen production

Name	Plies	Stacking sequence
A	12	$[0_{12}]$
B	12	$[90_{12}]$
C	12	$[45_{12}]$
D	12	$[15_3\|\text{-}15_3]_s$
E	12	$[30_3\|\text{-}30_3]_s$
F	12	$[45_3\|\text{-}45_3]_s$
G	12	$[60_3\|\text{-}60_3]_s$
H	12	$[75_3\|\text{-}75_3]_s$
I	20	$[0_2\|45_2\|90_2\|\text{-}45_2\|0_2]_2$

For cutting, a digital cutter G3 by Zünd Systemtechnik AG (Altstätten, Switzerland) was used. A power rotary cutting tool is applied instead of a pneumatic oscillating cutting tool due to the rectangular cutting pattern. The cutter is equipped with a vacuum table to

provide optimal material hold-down on a working area of 1600 mm x 1330mm. It is especially necessary for a precise cutting of off axis plies. Since fibre fabrics are air-permeable, fabrics were covered by a plastic film to guarantee a material hold-down. The cutter and the cutting pattern can be seen in **Fig. 3.1**.

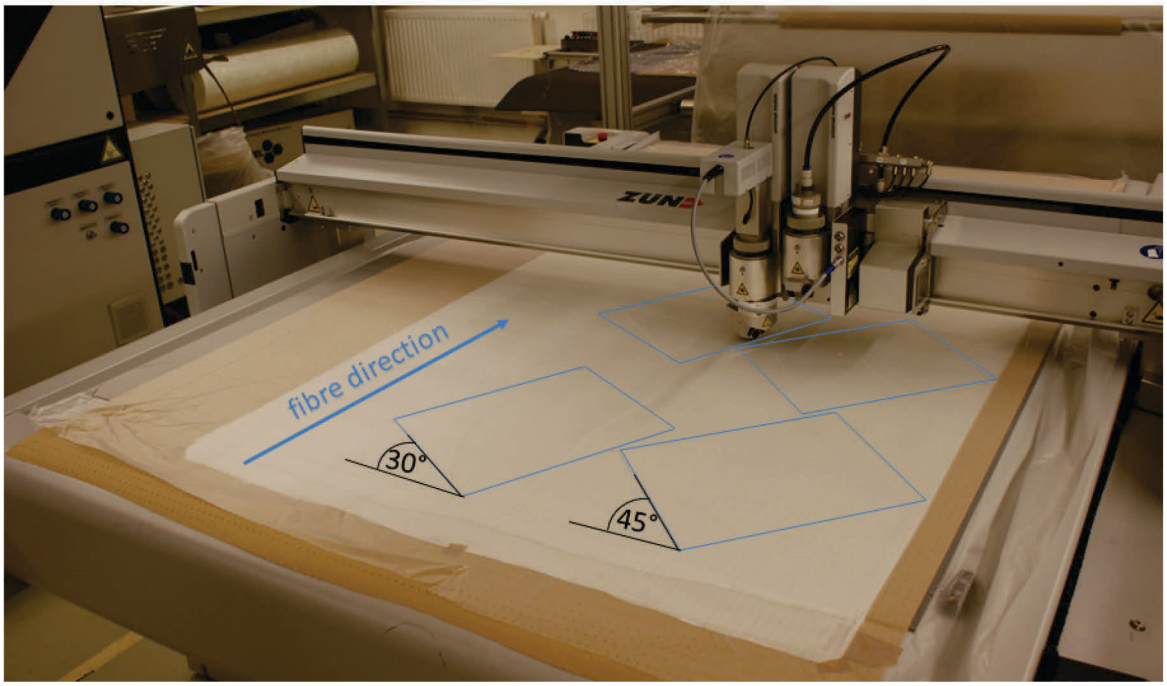

Fig. 3.1: Digital cutter G3 by Zünd Systemtechnik AG cutting a unidirectional glass fibre fabric.

Vacuum infusion technology

The vacuum infusion technology (VI) was chosen first for specimen production, due to the easy adaptability of different plate dimensions that allows production of several stacks with a low material usage. The VI is not limited by the tool geometry compared to resin transfer molding (RTM).

The release agent Spacewax 300 by Jost Chemicals Gmbh (Laudenbach, Germany) was used to ensure a problem-free demoulding of cured plates from the vacuum-desk. The release agent was applied on the desk's surface before the stacks were laid down. A peel ply was draped over the laminate, to remove processing aids from the cured plate. Flow aids were added, to guarantee resin distribution over the entire preform. The resin was bleeding through the peel ply and flow aids, due to their high permeability. Processing aids like tacky tape, spiral tubes and the vacuum film were added additionally, as shown in **Fig. 3.2a** and **Fig. 3.2b**.

After a vacuum-leak-test, the resin inlet valve had been opened to start the vacuum infusion process, as presented in **Fig. 3.2c**. The flow front was not distributed equally over the laminate's width; the spiral tube was not positioned parallel to the laminate's edge. The laminate was demoulded after a curing time of 24h at room temperature. Since glass fibre reinforced polymers are translucent, manufacturing imperfections were detected by visual inspection, as evident from **Fig. 3.2d**. The useable part was limited of the first produced laminate with a $[0_{12}]$ stacking sequence. Possible error causes were the long flow paths perpendicular to the fibre direction or a vacuum leakage during the curing time of 24h.

A second laminate was produced with the $[0_2|45_2|90_2|\text{-}45_2|0_2]_2$ stacking sequence. Uniformly distributed air voids were found within the laminate after a precise visual inspection. Even an increased diligence during the manufacturing process had not been sufficient to prevent air voids. This laminate could be interesting for an additional investigation about the influence of the void content on the mechanical properties. However, the achieved laminate quality was not satisfactory for meaningful fatigue-life investigations, which is the aim of this thesis. Thus, the vacuum pressing technology was chosen as an alternative manufacturing method for the required laminate plates.

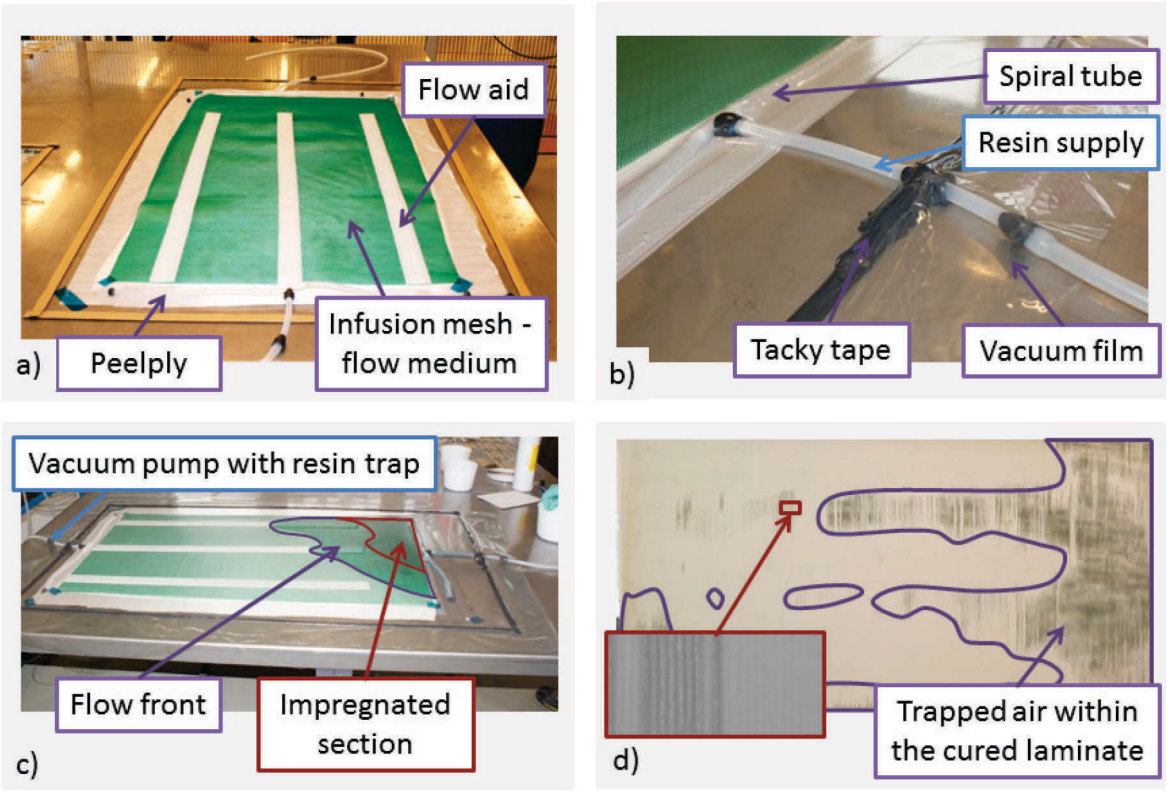

Fig. 3.2: Laminate-manufacturing process with the vacuum infusion technology.

Vacuum pressing technology

The advantages of the vacuum pressing technology compared to the VI are separately heatable toolings and the vacuum bell. This leads to smooth surfaces on both sides of the laminate. An excellent vacuum quality that is achieved by the vacuum bell, is responsible for air void free laminates. The heatable tool was cleaned with a Chemlease® Mold Cleaner EZ by Chem-Trend. A semi-permanent mold release Chemlease® R&B EZ by Chem-Trend was applied. Thermalimide release films were added on both sides to simplify the demoulding process and to reduce the cleaning effort. The preform and the tacky tape, which is limiting the resin outlet into the remaining mold, can be seen in **Fig. 3.3a** and **Fig. 3.3b**. The vacuum bell of the press is displayed in **Fig. 3.3c**. Before the resin system and the preform were pressed, vacuum was drawn for 5 minutes to avoid air voids in the cured laminate. The laminate was pressed for 3 hours at 100kN, which is measured at the cylinder piston by the machine. To accelerate the curing process that is specified with 24h at room temperature, the tooling was heated up to 80 degrees Celsius. The achieved laminate quality was excellent and without manufacturing imperfections in most cases, as shown in **Fig. 3.3d**.

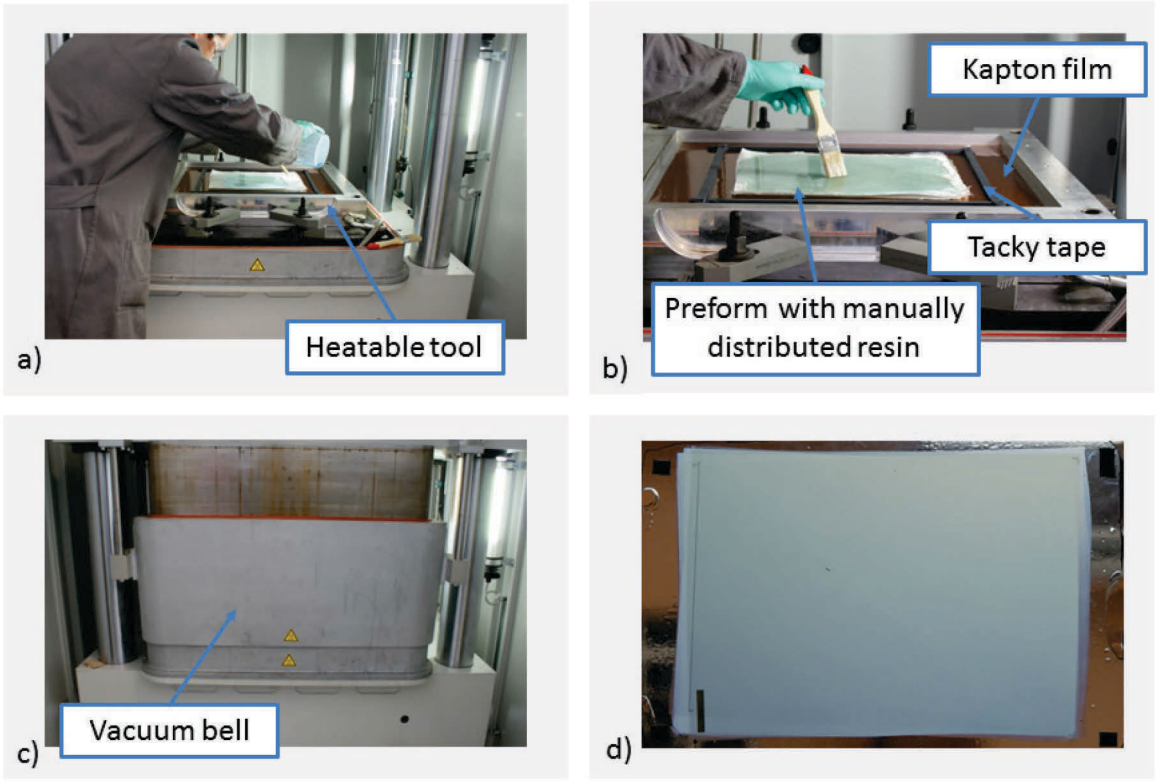

Fig. 3.3: Laminate-manufacturing process by vacuum pressing technology.

Test specimens production

All specimens were tailored with a precision laboratory specimen cutting-path DIADISC 5200 by Mutronic Präzisionsgräetebau (Germany). The geometries for UD [0°] specimens were 200x10x2 mm (length x width x thickness) for quasi-static tension tests and tension-tension fatigue tests; 110x10x2 mm (length x width x thickness) for quasi-static compression tests and compression-compression fatigue tests. All other specimen dimensions are detailed in **Fig. 3.4** and **Fig. 3.5.**

All specimens were tempered in a heating furnace at 80 degrees Celsius for 15 hours according to the manufacturer specifications. Specimen's surfaces and aluminium end tabs were sanded down, and were then degreased with isopropyl alcohol. It is necessary for a good adhesive bond. Specimens, adhesive films 3M™ Scotch-Weld™ Structural Adhesive Film AF 163-2L by 3M Company (Minnesota, USA), and end tabs were pressed for 1 hour at 80 degrees Celsius and 3bar with a laboratory platen press P300E by Dr. Collin (Germany).

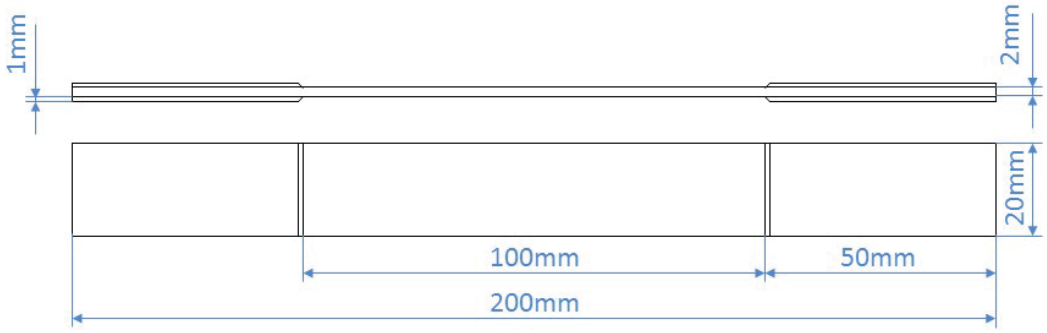

Fig. 3.4: Geometry for off-axis specimens and UD $[90]_{12}$ specimens used in quasi-static tensile tests and tension-tension fatigue tests.

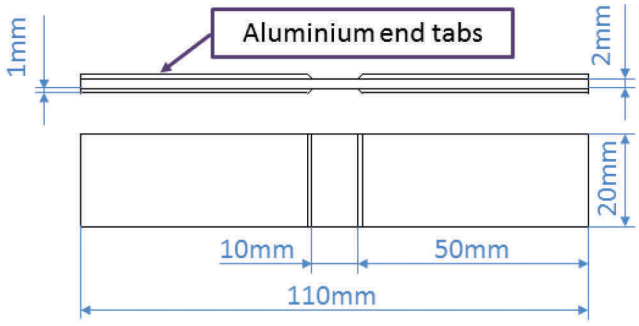

Fig. 3.5: Geometry for off-axis specimens and UD $[90]_{12}$ specimens used in quasi-static compression tests and compression-compression fatigue tests.

Sanding

The edges of specimens A to H (see **Table 3.1**), that were provided for fatigue tests and transmitted light damage monitoring, were sanded by a belt sander to remove any excessive glue. The belt sander's gain was P80. Immediate after the excess glue was removed, markings with an Edding 300 were added to ensure a uniform sanding of the surface. Specimens were sanded with decreasing pressure and alternating angle to the sanding-direction until the markings were not visible any more. They were next sanded with sandpapers with P240, P600 and P1200 grain. This procedure were performed to prevent unintended crack initiation from the specimen's edges.

Light microscopy

All specimens were investigated with a stereomicroscope SZX12 by Olympus (Tokio, Japan), which is equipped with a polarization filter and a ColorView IIIu Soft Imaging System by Olympus (Tokio, Japan). The imaging system enables image acquisition and processing with a supplied software. In this work, all specimens were investigated in transmitted light mode. The angle deviation of the fibres in the laminate from the required angle were determined. A polarization filter was applied to increase the contrast between fibres and matrix to allow the determination of the fibre angle.

3.2 Quasi-static material characterisation

The quasi-static compression tests were performed on a universal material testing machine Z250 by Zwick (Ulm, Germany), which was equipped with a 250kN load cell and hydraulic grips for compression-loads. The hydraulic pressure was adjusted to 150 bar, to avoid specimen slipping. High-precision strain measurement was achieved with an optical 3D deformation analysis system ARAMIS by GOM (Braunschweig, Germany). This is a non-contact and material independent measuring system, which was calibrated before testing. As Digital Image Correlation was used, speckle patterns were produced with graphite sprays on specimens surfaces. Before testing, a specific calibration cube was used for the calibration. The cube has a defined pattern and an adequate size compared to the specimen-size. In addition to the LED lighting system, a cold lighting system COOLT3 Tugsten Light System by Dedocool (Ashley Falls, USA) was positioned. All specimens were loaded in a displacement-controlled way with a test speed of 0.5 mm/min. The tests were performed in conformity to ISO 14126. The test setup can be seen in **Fig. 3.6** (a). **Fig. 3.6** (b) displays a $[45/-45]_s$ specimen after failure.

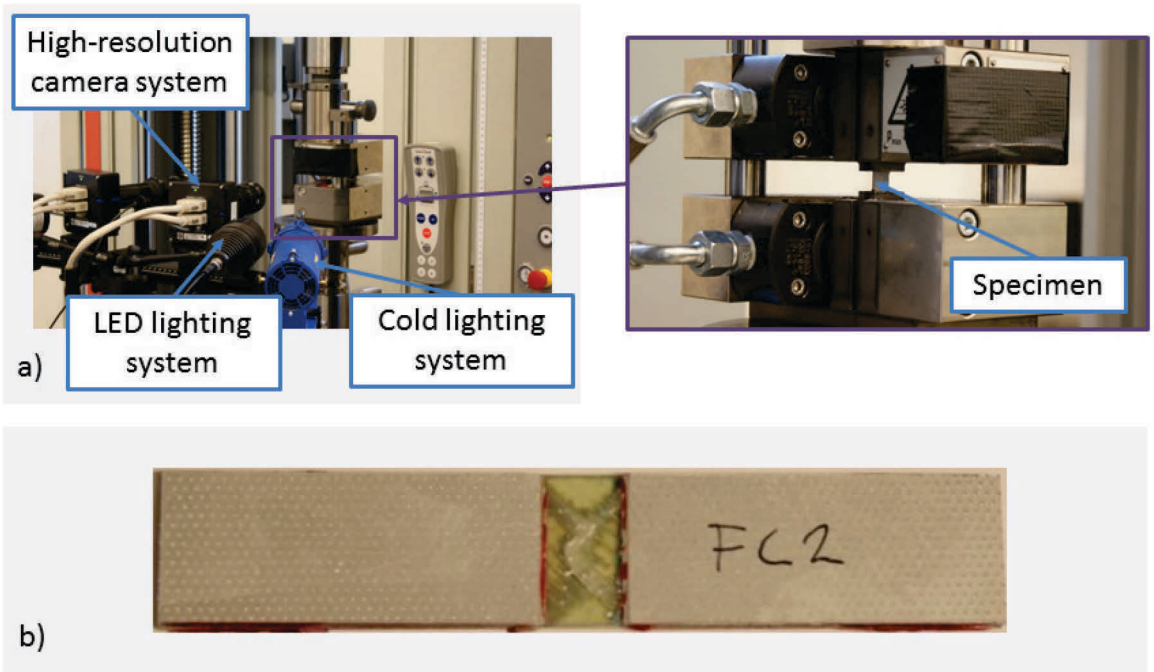

Fig. 3.6: a) Test setup for quasi-static compression tests of glass fibre reinforced specimens; b) failure of a $[45/-45]_s$ specimen after quas-static compression test.

Quasi-static tension tests were performed on a servo-hydraulic material testing system MTS 810 by MTS Systems Corporations (Minnesota, USA). The machine is equipped with a 100kN load cell and MTS 647 Hydraulic Wedge Grips. All specimens were loaded in a displacement-controlled way with a test speed of 0.5 mm/min. An optical 3D deformation analysis system ARAMIS by GOM (Braunschweig, Germany) was implemented for a high-precision strain-measurement. As ARAMIS was used, it was possible to analyse strains in three directions. Hence, the Poisson's ratio was calculated by evaluating the strains longitudinal and transverse to fibre direction with UD 0° specimens according to Brunbauer and Pinter (2015). The MTS 810 was connected with the ARAMIS system via analogue outputs. Specimen with different stacking sequences had different UTS. The gain of the analog outputs was adjusted and documented for each laminate. Thus, the right measuring range was ensured, and the signal noise was minimised. Specimens were positioned using a metal-angle first, and then checked with the software ARAMISv6.3.0 to control, if they were clamped perpendicular to the wedge grips.

To avoid influences of edge effects in the strain evaluation, only central sections were selected for the evaluation. **Fig. 3.7a** gives an overview of the test setup, and **Fig. 3.7b** shows a tested specimen with $[45/-45]_s$ layout.

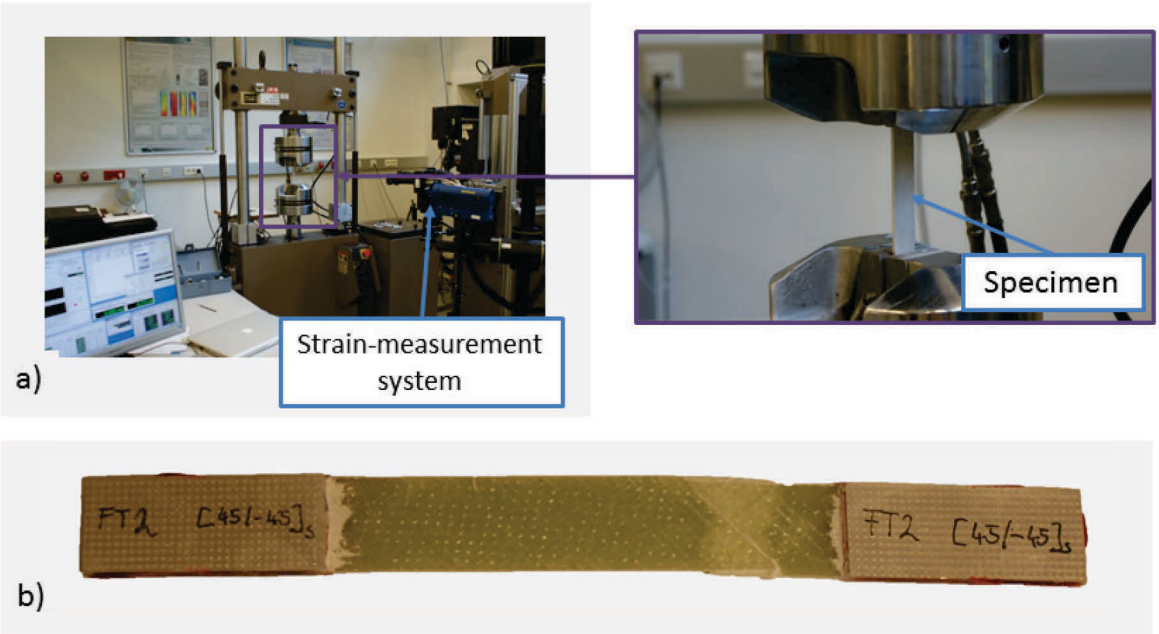

Fig. 3.7: a) Test setup for quasi-static tension tests of glass fibre reinforced specimens; b) failure of a $[45/-45]_s$ specimen after quasi-static tension test.

3.3 Fatigue tests

Cyclic tension-tension tests were performed on a servo-hydraulic material testing system MTS 810 by MTS Systems Corporations (Minnesota, USA). The machine is equipped with a 100kN load cell and MTS 647 Hydraulic Wedge Grips. The Gauge length was 100mm for all specimens and the test frequency was chosen between 5 and 10 Hz. The fatigue tests were performed at lamina-dependent stress levels. Therefore, all specimens were loaded with a load that complied with a safety factor of two for static loads after Puck's approach. The calculations were made by using a composite calculator eLamX, developed by Technische Universität Dresden. With this software, all laminates were designed using the CLT; the factor of safety for each ply was determined by Puck's failure criterion. An optical displacement measurement system CV-X100 by Keyence (Osaka, Japan) was used to enable a transmitted light damage monitoring. Strain measurement techniques like mechanical extensometers, digital image correlation and strain gauges were not used because they hide parts of the specimen. Hence, they disable the transmitted light damage monitoring. Barrier chains were positioned to avoid an inadvertent touching or moving of the optical strain measurement system. The test setup is detailed in **Fig. 3.8**.

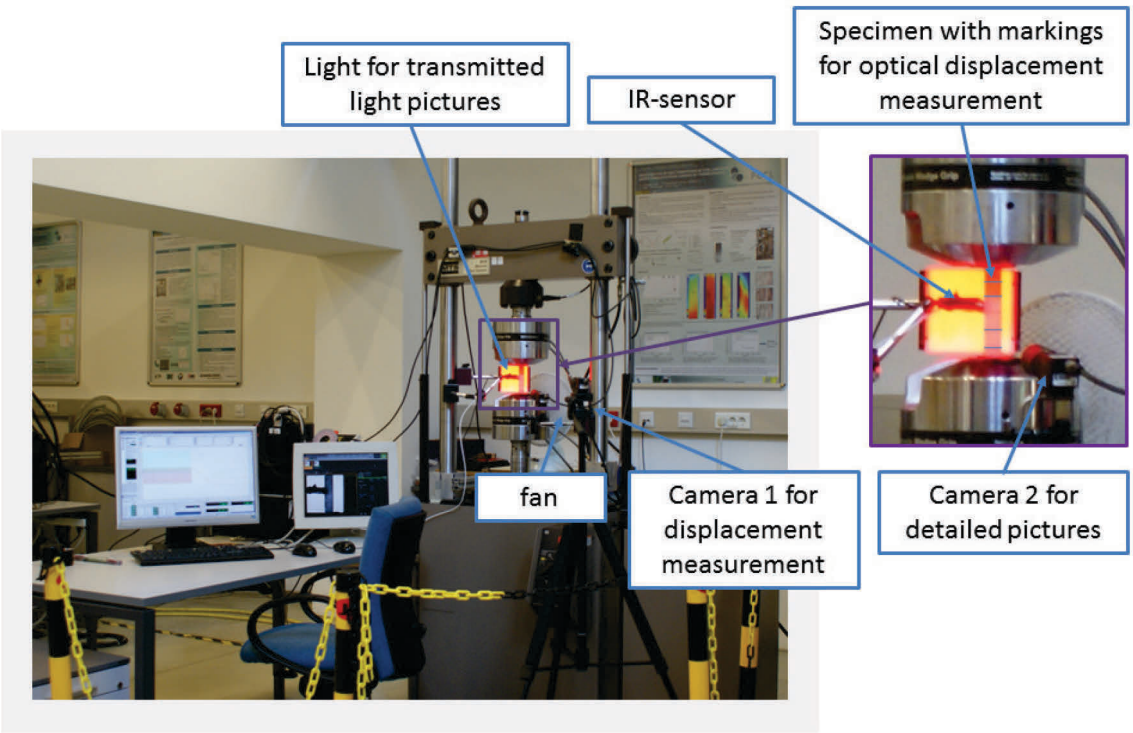

Fig. 3.8: Test setup for cyclic tension-tension fatigue tests of glass fibre reinforced specimens with an optical strain measurement system and damage monitoring with transmitted light

As shown in **Fig. 3.8**, a fan was added to avoid a temperature increase, that is caused by hysteretic heating during fatigue tests of ±45° specimens, as recommended in Brunbauer and Pinter (2014). The temperature of the specimens was additional measured with an IR-sensor that was connected with the controller of the servo-hydraulic machine.

Experimental test procedure

Sinusoidal loads combined with cyclic tensile tests were performed, according to the test procedure presented in Brunbauer et al. (2014). It was adapted to the transmitted light damage monitoring approach as illustrated by **Fig. 3.9**. The test procedure started with a displacement controlled tensile test to determine the Young's modulus of the undamaged specimen. The diagrams in chapter **4.3**, which present the relative Young's moduli over the cycles, were related to that first measured modulus. The load was then introduced sinusoidal for a period of 50 cycles. The quantity of cycles between each cyclic tensile test was increased during the test and tuned to the expected lifetime of each laminate. The maximum range between cyclic tensile tests were 2500 cycles of sinusoidal load.

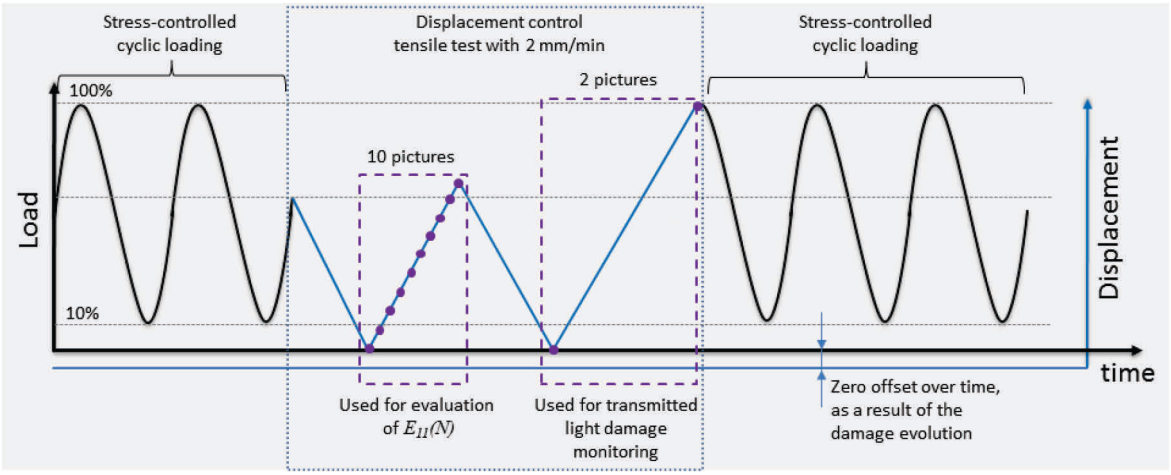

Fig. 3.9: Experimental test procedure 'cyclic tensile tests' and trigger for the optical displacement measurement system, according to Brunbauer et al. (2014)

The optical strain measurement system by Keycence (Osaka, Japan) was adjusted to take 10 pictures for strain measurement during each tensile tests. It was triggered by the servo-hydraulic machine's controller. Tensile tests were started at unloaded conditions of 0N. The maximum displacement performed by the servo-hydraulic machine was 0.35 mm during the tensile test. After the tensile tests, the specimen was unloaded again, because pictures at a load level of 0N and at maximum load were taken after each cyclic tensile

test. After this section of the experimental test procedure, the machine switched to load control and performed again the defined amount of cycles.

Data processing

Since fatigue tests generates a large amount of data, in particular with an optical strain measurement system, it is necessary to have a structured and automated data processing system. Both Keyence cameras generated several thousand pictures, for every fatigue test. The pictures were stored chronological on the SD-card of the Keyence-controller. The first ten pictures taken by the Keyence cameras for each cyclic tensile test were necessary for the strain calculation. The following two pictures were taken for the transmitted light damage monitoring. Therefore a batch-script was written to separate the pictures of the transmitted light damage monitoring from the strain measurement pictures automatically to enable the damage evaluation.

In view of the fact that the sample rate of Keyence strain measurement system with 10 points per modulus evaluation is not equal to the time-depending sample rate of 1 point/ms of the MTS controller, the modulus evaluation $E_{11}(N)$ is not trivial. A MathLab-script was developed to handle this problem. In the first step, the raw data was analysed and filtered, so that every data set logged by the MTS controller was linked to the corresponding data set logged by the Keyence controller. **Fig. 3.10** illustrates a part of the MathLab-script, which solves the problem with different sampling rates. A linear regression of the measured strain **(3.1)** by the Keyence camera system was applied and recalculated with linear equations.

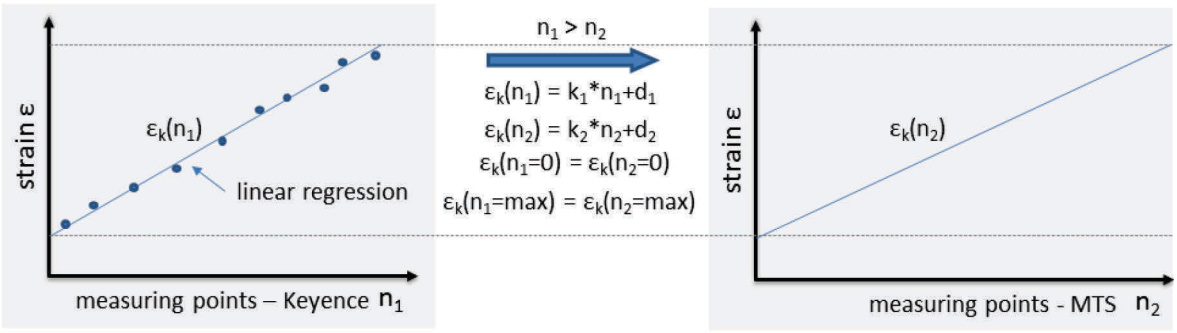

Fig. 3.10: Part of the MathLab-script, it solved the sampling rate problem.

$$\varepsilon_k(n_1) = \frac{l(n_1) - l_0}{l_0} * 100\% \qquad (3.1)$$

Due to the decreasing translucency within a progressive crack accumulation, as found in ±45° specimens, the optical displacement measuring system is limited at that point, as evident from **Fig. 3.11.** Hence, a correction vector was calculated from the beginning of each evaluation, to calibrate the strain, measured by the servo-hydraulic machine, with the correct measured strain by the Keyence strain measurement system. When necessary, the calibrated piston-strain was used for the calculation of the Young's moduli from the cyclic tensile test. The moduli were evaluated by a linear regression of the measured stress $\sigma_{11}(n_2)$ and the strain $\varepsilon_k(n_2)$ or $\varepsilon_{piston,korr}(n_2)$.

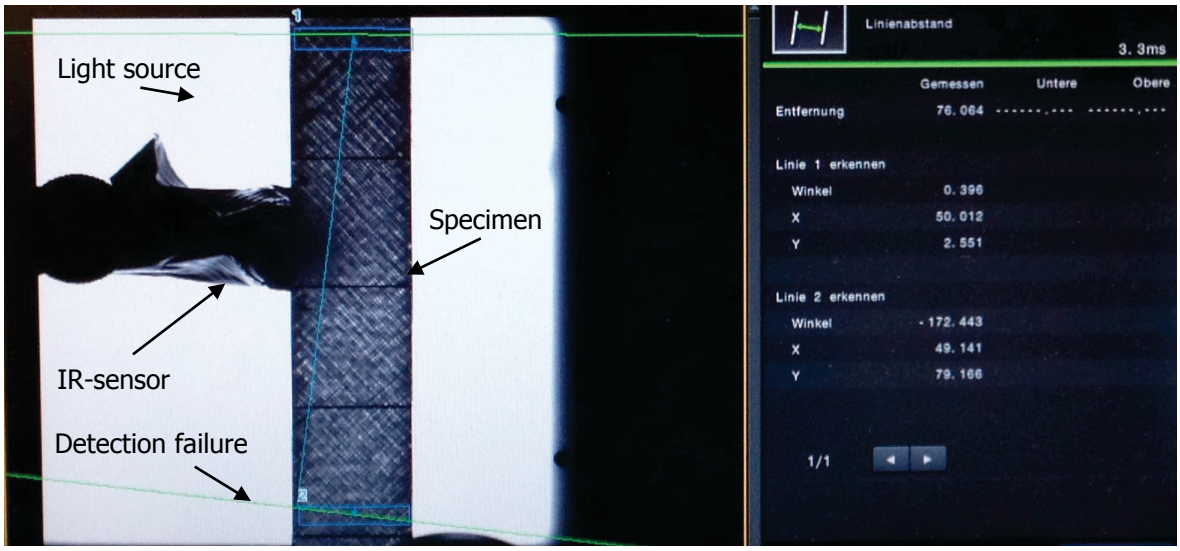

Fig. 3.11: Measurement error of the optical displacement measurement system, because of a decreasing translucency within increasing damage evolution.

In addition, a stress-strain diagram was plotted automatically for each cyclic tensile test. The quality of the calculated data was controlled therefore. The entire time-dependent data set was stored in a .CSV file and was edited with OriginPro 2016.

The MathLab-script performed the preliminary work required to rename the pictures of the transmitted light damage monitoring. Therefore, a second Batch-script was developed which renamed the pictures and linked them to information like Young's modulus, cycles and temperature. The reduction of the relative modulus was assigned to damage events within the specimens.

3.4 Non-destructive testing (NDT)

To create the subjects for the NDT investigations, six specimens with a multiaxial $[0_2|45_2|90_2|-45_2|0_2]_2$ stacking sequence were tested under fatigue loads. This stacking sequence was chosen due to the additional 0° layers, which relieved layers with off-axis fibre angles, as recommended in (Quaresimin et al. 2014). Thus, the crack and delamination accumulation was investigated until specimen failure. The fatigue tests were stopped, at different damage levels. Thereby, different damage levels of the laminate were analysed with common NDT techniques.

Because NDT investigations require specific technical expertise and expensive test equipment, the investigations were performed in cooperation with companies and universities who are specialised in respective NDT-methods.

Thermographic inspection

Thermographic inspections were performed at the chair of automation at Montanuniversität Leoben (Austria). The thermographic tests were carried out by Thomas Grandl, BSc and directed by Priv.-Doz. Dr.techn Beate Oswald-Tranta who is specialized on automated thermographic non-destructive testing. The resolution of the IR-camera is 600x400 pixel. It was connected additionally with a microscope for the attempt of detailed images.

Water-coupled ultrasonic inspection

The water-coupled ultrasonic tests were performed at the TCKT - Transfercenter für Kunststofftechnik GmbH (Wels, Austria). The tests were directed by Dipl.-Ing. Volker Reisecker. The TCKT is equipped with an automated ultrasonic test system in immersion bath. The test equipment is comprised of an OmniScan MX equipped with a 16:64 5 MHz phased array module by Olympus (Osaka, Japan).

Air-coupled ultrasonic testing

Air-coupled ultrasonic tests were performed at department of polymer engineering IKT at the University of Stuttgart (Germany) and directed by Dipl.-Ing. Wolfgang Adebahr, who is specialized on non-destructive ultrasonic testing. Air-coupled UT was performed in

transmission mode with lamb wave excitation (FSTM). Therefore, a specific angle is required between the transmitter and the specimen. This angle is also adjusted between the receiver and the specimen. The transmitted amplitude is up to 10 times higher than a conventional transmitted amplitude in air-coupled normal transmission mode (Döring 2011). The inspections were performed on an automated test system. It is equipped with a linear actor for inspections of the entire specimen.

Computed Tomography (CT)

CT inspections were performed at an international company in Germany that is equipped with a medical CT, CT GE NX/I Pro by GE HealthCare (Little Chalfont, Great Britain), for quality assurance purposes and a micro CT for research issues. The medical CT inspections were performed with 140 kV and 170 mA bremsstrahlung, a gain of 0.5 and an exposure time of 3 s. All specimens were scanned separately.

Micro CT investigations were performed with 160 kV and 140 mA bremsstrahlung, a gain of 1, exposure time of 4 s and a voxel size of 20 µm. Three specimens were scanned at the same time to obtain a volume that is as cylindrical as possible. The experimental test setup is given in **Fig. 3.12**.

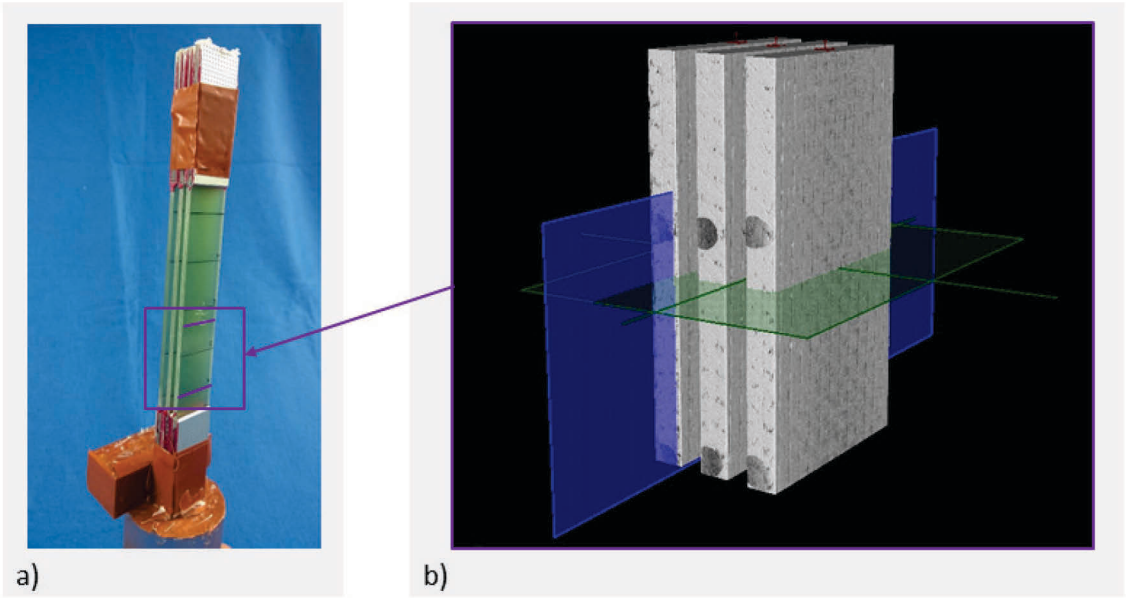

Fig. 3.12: a) Experimental test setup of the micro CT investigations of glass fibre reinforced specimens. b) calculated 3D volume model of the glass fibre reinforced specimens with different damage states.

4 RESULTS

Previous studies like Quaresimin et al. (2014), which are focused on damage evolution under multiaxial stress states, used glass fibre reinforced polymers laminates and tubes in their investigations. GFRP are semi-transparent, and by using a light source, it is possible to observe crack initiation and growth during fatigue tests. A research group at the Montanuniversität Leoben (Brunbauer et al. 2014) presented a test procedure to measure the Young's modulus with cyclic tensile tests during fatigue tests. Böhm and Hufenbach (2010) compared NDT methods under static loads; however their suitability for online damage monitoring during fatigue tests is unclear. In this study, GFRP laminates with different fibre angles were tested under cyclic loads with cyclic tensile tests. The load levels were calculated for each laminate, so that the *RF* after Puck equalled two. After the testing, state of the art NDT methods were checked for their suitability for damage monitoring during fatigue tests.

4.1 Material properties characterisation

Quasi-static tensile and compression tests were performed to determine the static material properties. Those characteristic values were used for the CLT calculations and the determination of the factor of safety. **Fig. 4.1** presents the stress-strain curves of the tested laminates. It can be seen that the [0°] layup has the highest ultimate tensile strength UTS and the highest Young's modulus due to the in load direction oriented fibres (see also **Fig. 4.2** and **Fig. 4.3**). In general, the results of the quasi-static tensile tests were as expected. The mechanical properties decreased with an increasing off-axis fibre angle. The strong decrease of UTS within the range of Θ 0° until ±45° and the minor differences of the UTS between Θ ±45° and 90°, agree with literature. The significantly higher elongation at UTS observed by [45°/-45°] layup (see **Fig. 4.4**) is characteristic for this layup. A "fibre reorientation" caused the high elongation at UTS and low stiffness before failure. The material properties, used for the calculation of the required load according to a safety factor of two are listed in the appendix. The results of the quasi-static compression tests are not presented at this point, because the free inspection area between the end tabs is too small, for a reasonable transmitted light damage monitoring, thus no fatigue tests were performed. The evaluated material properties under quasi-static compression load are listed in the appendix.

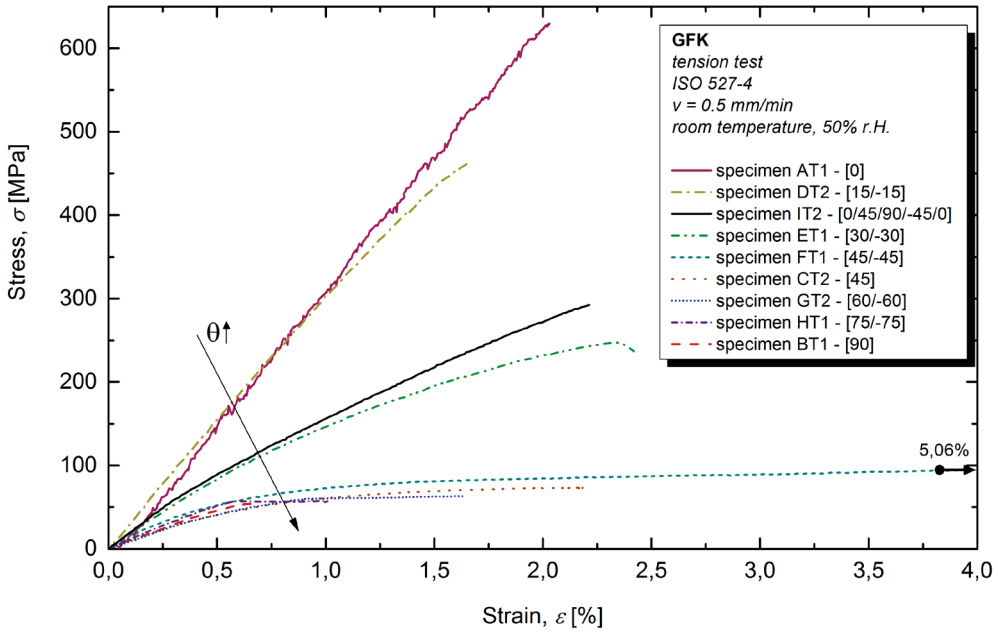

Fig. 4.1: Representative stress-strain diagram from quasi-static tensile tests of glass fibre reinforced specimens with various stacking sequences.

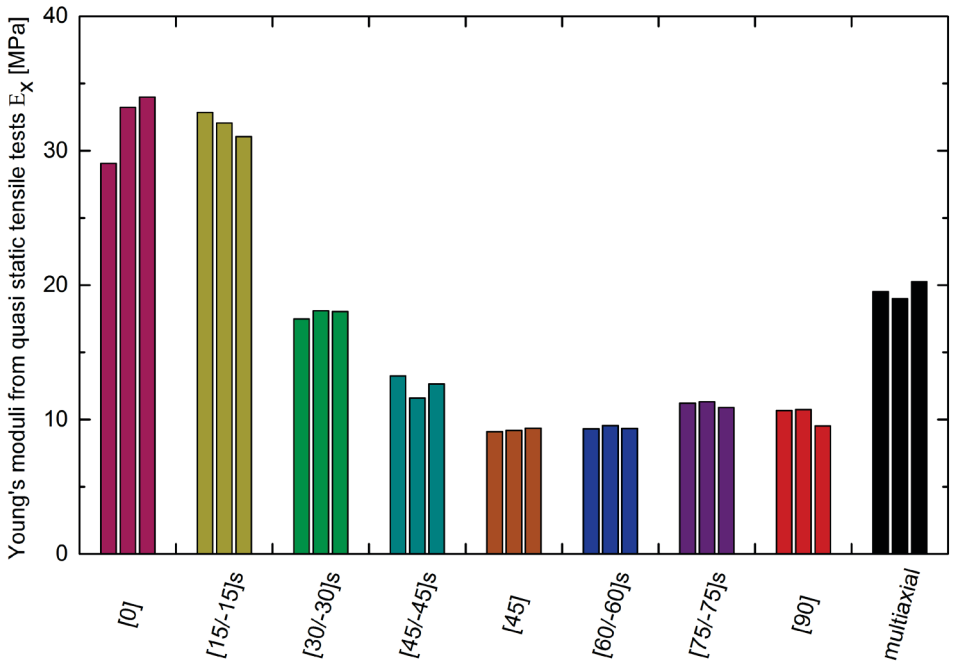

Fig. 4.2: Young's moduli from quasi-static tensile tests in dependence of the laminate layup of glass fibre reinforced specimens, v=0.5 mm/min, DIC, test setup is according to ISO 527-4, multiaxial refers to $[0_2|45_2|90_2|-45_2|0_2]_2$.

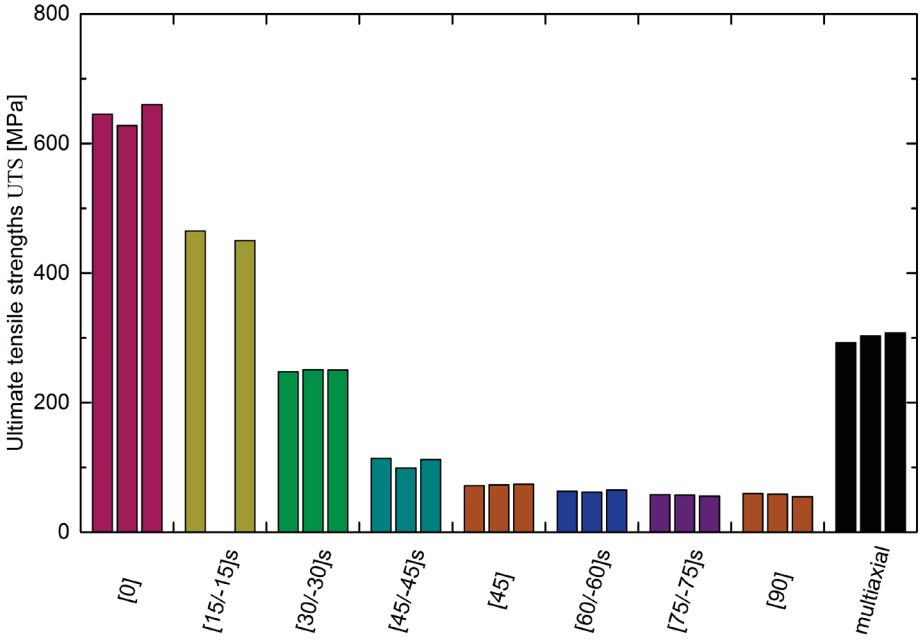

Fig. 4.3: Ultimate tensile strengths from quasi-static tensile tests in dependence of the laminate layup of glass fibre reinforced specimens, v=0.5 mm/min, DIC, according to ISO 527-4, multiaxial refers to $[0_2|45_2|90_2|-45_2|0_2]_2$.

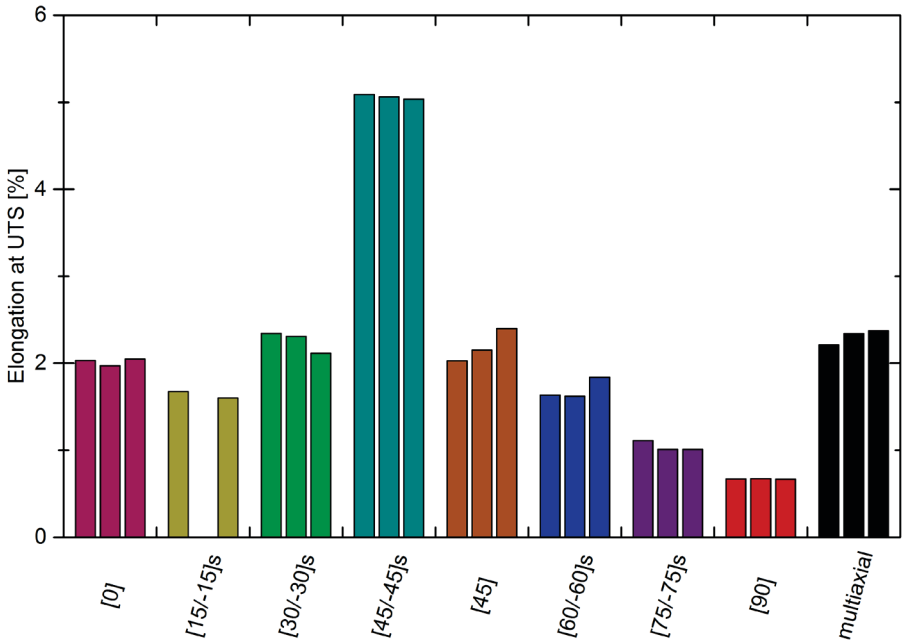

Fig. 4.4: Elongations at ultimate tensile strength from quasi-static tensile tests in dependence of the laminate layup of glass fibre reinforced specimens, v=0.5mm/min, DIC, according to ISO 527-4, multiaxial refers to $[0_2|45_2|90_2|-45_2|0_2]_2$.

Fibre angle deviation

The fibre angle deviation was found within a production-related deviation, as represented in **Fig. 4.5**. These deviations occurred during the stack-laying process. The fibre-angles of the unidirectional glass fibre fabrics shifted slightly, which was caused by transport and handling of the stacks. Fibre wash-out caused by the manufacturing process (vacuum pressing technology, see **3.1**) was not observed. The slightly higher angle-deviation of the [45°] specimen CT5, compared to the [45°] specimen CT1, had no measurable effect on the fatigue properties. The relative moduli from cyclic tensile tests of specimen CT5 were very similar to the relative moduli from cyclic tensile tests of specimen CT1 (see **4.1**).

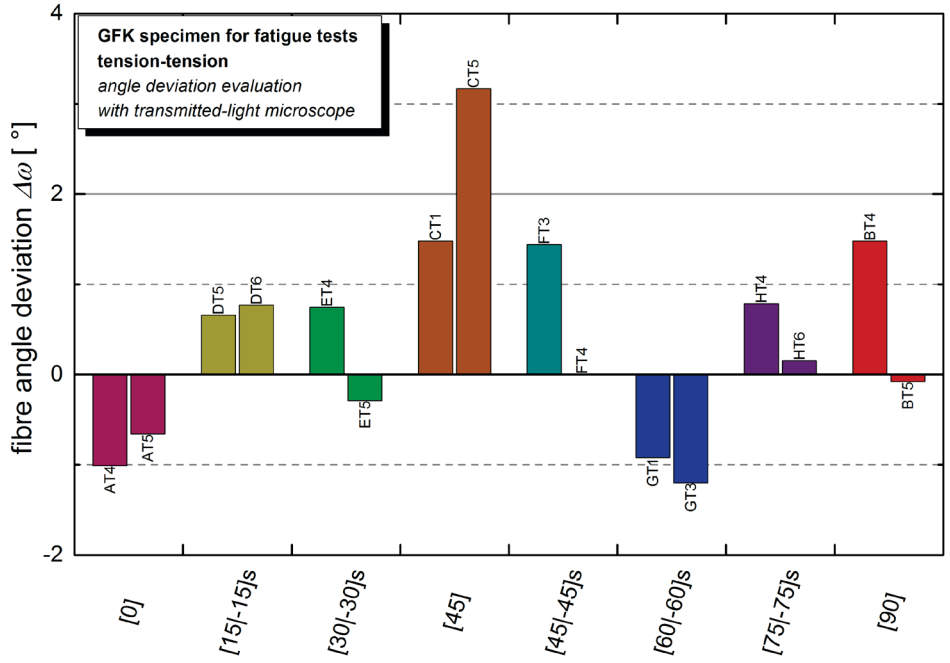

Fig. 4.5: Fibre angle deviation of glass fibre reinforced specimens with fibre-angle varied layup; laminate-manufacturing process by vacuum pressing technology; specimens were used for cyclic tension-tension fatigue tests including cyclic tensile tests.

4.2 Fatigue load level determination

This chapter includes stress-strain curves of each laminate with regard to the fatigue load levels. The fatigue load levels were calculated using the CLT and Puck's failure criterion, so that the RF equalled two for each laminate, to show the differences in the fatigue behaviours of statically equivalent loaded laminates. The failure modes after Puck are 'IFF Mode A' in general, except the [0°] laminate. The [0°] laminate's failure mode is FF-tension. The load levels were adjusted so that the RF equalled two, in general. Exceptions are the [45°] specimens and the $[0°/45°/90°/-45°/0°]_2$ specimens.

The [45°] specimens were accidentally tested with the same test-routine as the [45°/-45°] specimens, thus the factor of safety RF dropped to 1.52. However, the applied maximum stress σ_{max} in the stress-strain curves is in the same range as it is in the case of [45°/-45°] specimens (compare **Fig. 4.8** and **Fig. 4.11**).

The stress-strain curves differed significantly, especially in terms of the lateral strain. The highest lateral strains were found in [45°/-45°] laminates (see **Fig. 4.11**) and [30°/-30°] laminates (see **Fig. 4.10**). In contrast to [45°/-45°] laminates and [30°/-30°] laminates, moderate lateral strains were observed in [15°/-15°] laminates and [60°/-60°] laminates (see **Fig. 4.9** and **Fig. 4.12**, respectively). The lateral strain of [0°], [90] and [75/-75°] were nearly negligible (see **Fig. 4.6**, **Fig. 4.7** and **Fig. 4.13**).

Further similarities were observed in terms of the non-linearity at the fatigue load level. Three groups are to be distinguished. The first group, consisting of [45°], [45°/-45°] and [60°/-60°], had a significant deviation of the stress-strain curve to the linear fit of the modulus evaluation at the fatigue load level (see **Fig. 4.8**, **Fig. 4.11** and **Fig. 4.12**). This indicates that the fatigue load level was in the non-linear range of the stress-strain diagram. The second group, consisting of [15°/-15°], [30°/-30°] and [75°/-75°], had a small deviation of the stress-strain curve to the linear fit of the modulus evaluation at the fatigue load level (see **Fig. 4.9**, **Fig. 4.10** and **Fig. 4.13**). This indicates that the fatigue load level was near the linear range of the stress-strain diagram. The second group, consisting of [0°] and [90°], had almost any deviation of the stress-strain curve to the linear fit of the modulus evaluation at the fatigue load level. This indicates that th e fatigue load level was in the linear range of the stress-strain diagram (see **Fig. 4.6** and **Fig. 4.7**).

The $[0°/45°/90°/-45°/0°]_2$ specimens were tested up to different numbers of cycles for NDT-method comparisons. Those specimens were loaded with a stress σ_{max} of 100 MPa, which equalled an RF of 2.73. This load level was chosen to ensure slower crack accumulation, compared to the crack accumulation at higher stresses. This made it possible to separately identify damage evolution in different plies.

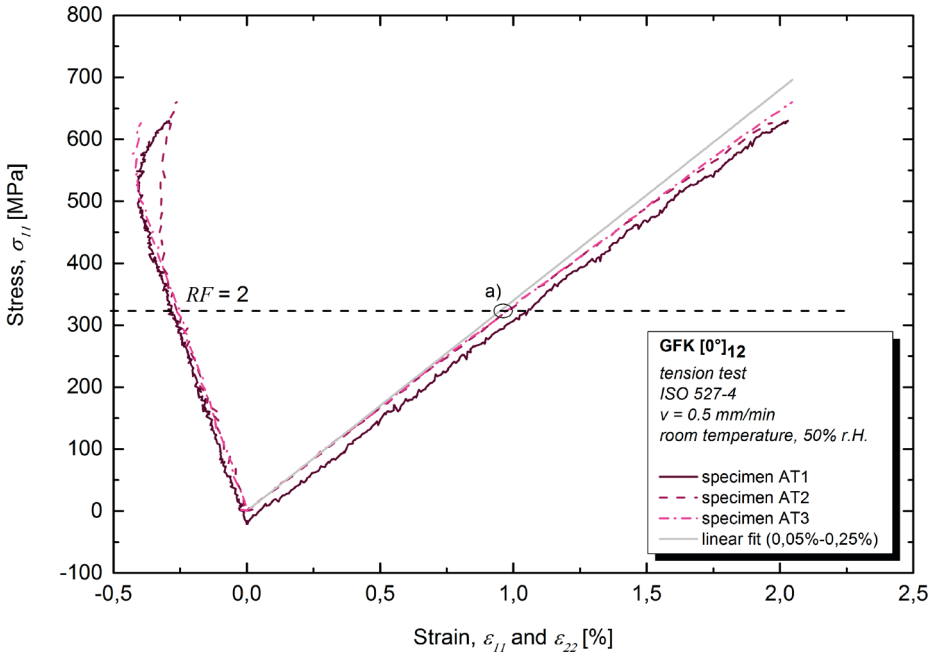

Fig. 4.6: Stress-strain curves of UD [0°] GFRP specimens, RF = 2 for static loads according to Puck's failure criterion, quasi-static tensile test according to ISO 527-4, strain measured with DIC. Almost no deviation combined with moderate applied stress is indicated a).

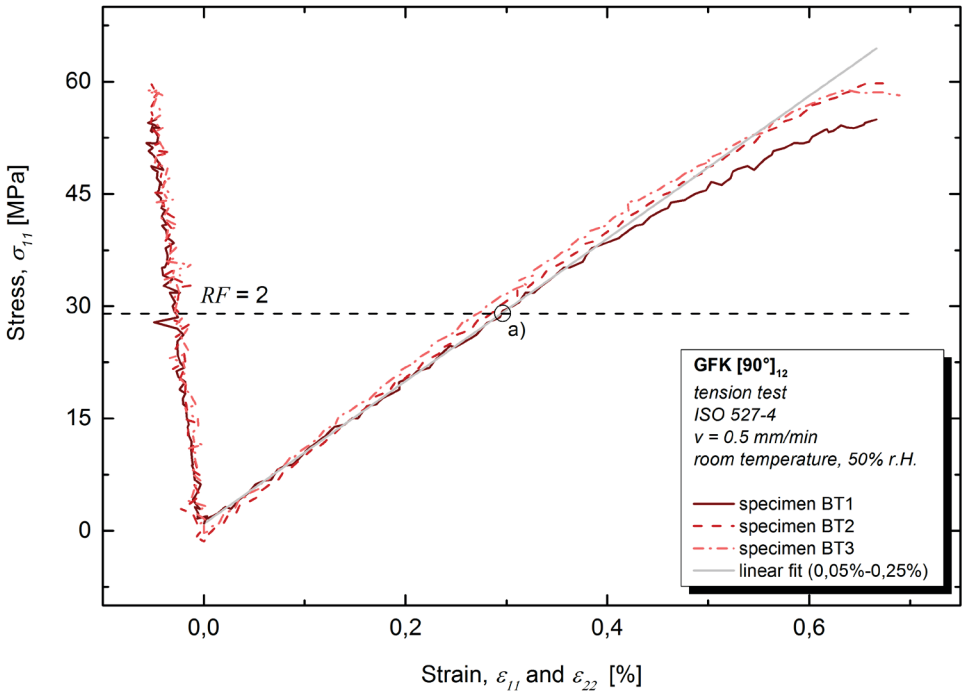

Fig. 4.7: Stress-strain curves of UD [90°] GFRP specimens, RF = 2 for static loads according to Puck's failure criterion, the quasi-static tensile test is according to ISO 527-4, strain was measured with DIC. Almost no deviation combined with moderate applied stress is indicated a).

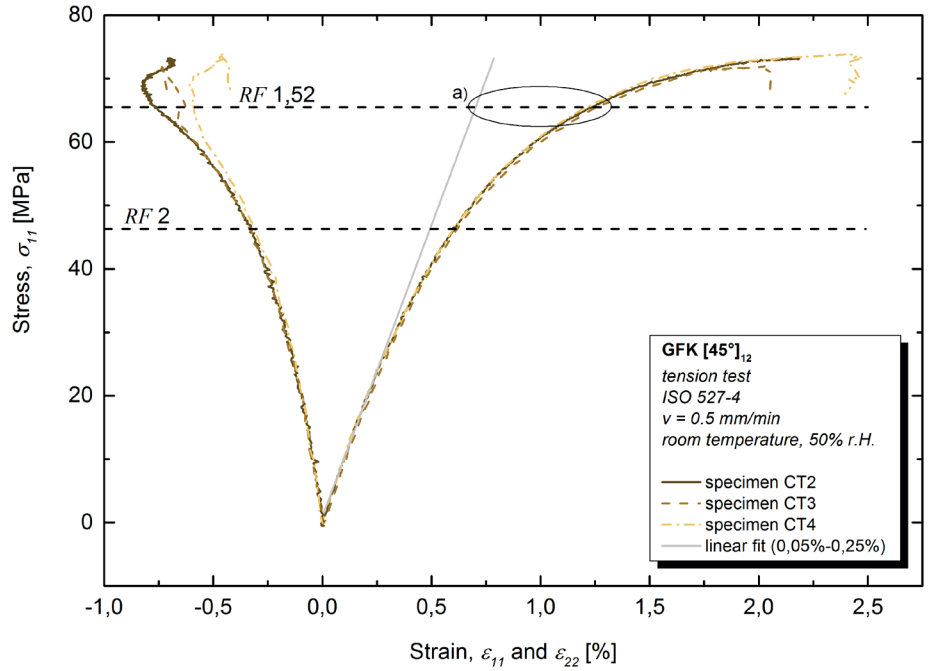

Fig. 4.8: Stress-strain curves of UD [45°] GFRP specimens, RF = 1,52 for static loads according to Puck's failure criterion, the quasi-static tensile test is according to ISO 527-4, strain was measured with DIC. A large deviation combined with high applied stress is indicated a).

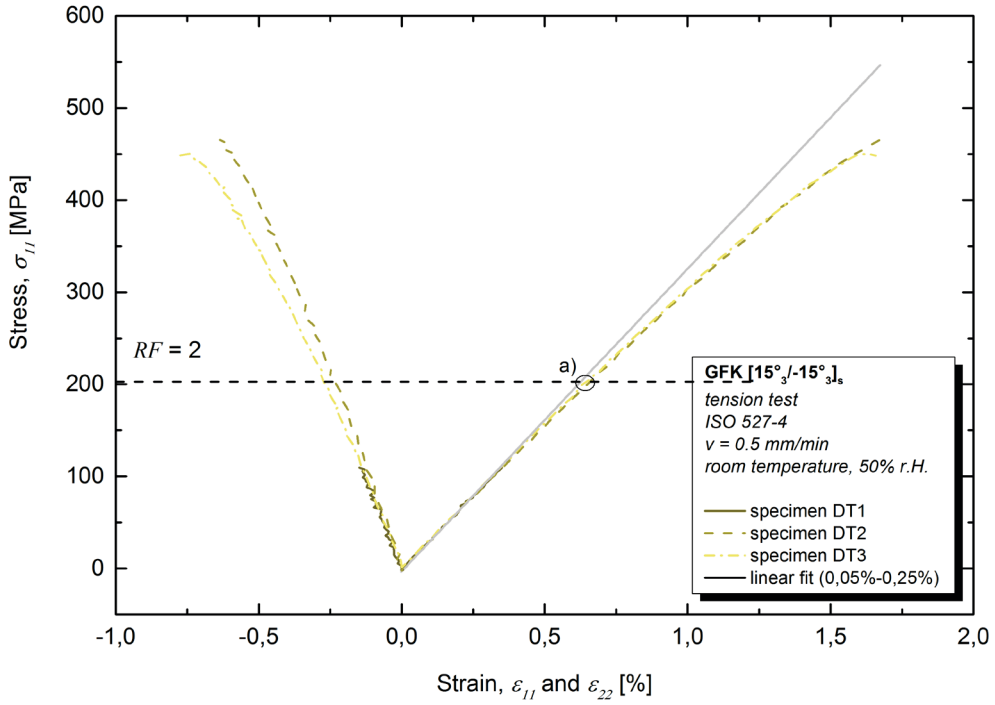

Fig. 4.9: Stress-strain curves of [15°/-15°]$_s$ GFRP specimens, RF = 2 for static loads according to Puck's failure criterion, the quasi-static tensile test is according to ISO 527-4, strain was measured with DIC. A small deviation combined with moderate applied stress is indicated a).

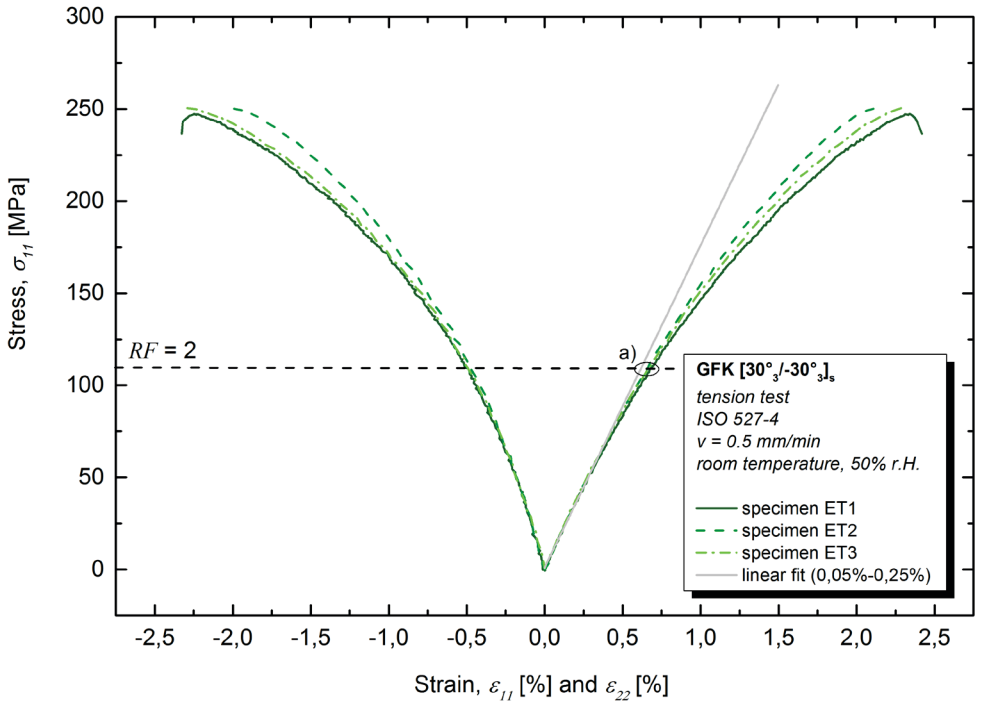

Fig. 4.10: Stress-strain curves of [30°/-30°]$_s$ GFRP specimens, RF = 2 for static loads according to Puck's failure criterion, the quasi-static tensile test is according to ISO 527-4, strain was measured with DIC. A small deviation combined with moderate applied stress is indicated a).

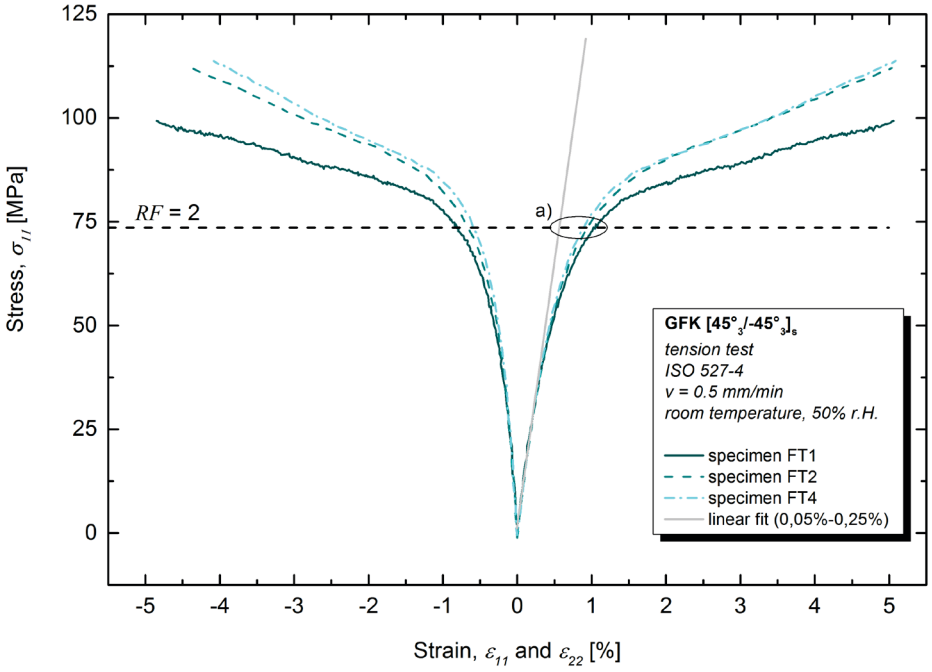

Fig. 4.11: Stress-strain curves of [45°/-45°]s GFRP specimens, RF = 2 for static loads according to Puck's failure criterion, the quasi-static tensile test is according to ISO 527-4, strain was measured with DIC. A large deviation combined with high applied stress is indicated a).

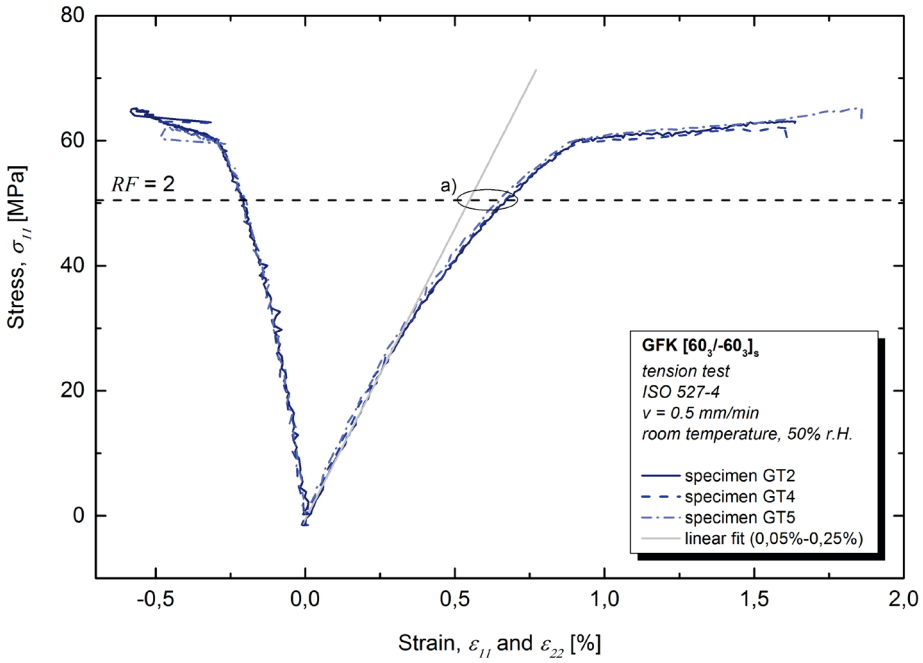

Fig. 4.12: Stress-strain curves of [60°/-60°]s GFRP specimens, RF = 2 for static loads according to Puck's failure criterion, the quasi-static tensile test is according to ISO 527-4, strain was measured with DIC. A large deviation combined with high applied stress is indicated in a).

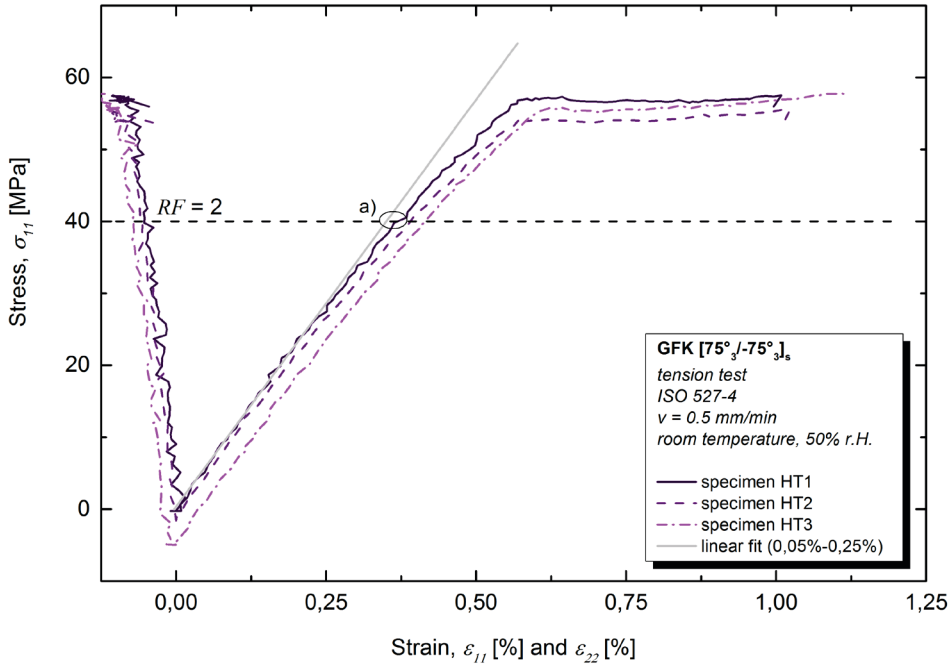

Fig. 4.13: Stress-strain curves of [75°/-75°]s GFRP specimens, RF = 2 for static loads according to Puck's failure criterion, the quasi-static tensile test is according to ISO 527-4, strain was measured with DIC. A small deviation combined with moderate applied stress is indicated in a).

0° dominated multiaxial stacking

The $[0°/45°/90°/-45°/0°]_2$ specimens were provided for the NDT-methods comparison. Those specimens were loaded with a stress σ_{max} of 100 MPa, which equalled an RF of 2.73, as mentioned before. It is apparent that in the case of multiaxial layups (tri-axial and more), each layer has a different RF. Thus, a mean RF was calculated, as illustrated by **Fig. 4.14**. It is likely, that the damage development is going to start in the layers with lowest RF, followed by the layers with the next lowest RF.

The stress strain curves are given in **Fig. 4.15**. A small deviation of the stress-strain curve to the linear fit of the modulus evaluation at the fatigue load level was observed. So the multiaxial laminate can be classified in the prior mentioned second group. The lateral strain is approximately equivalent to the half of the longitudinal strain.

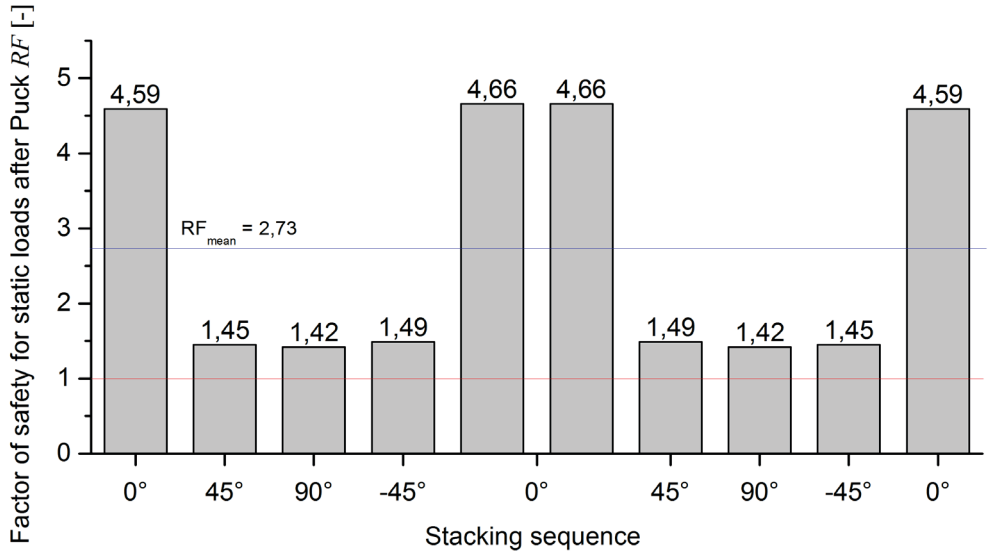

Fig. 4.14: Factors of safety for static loads after Puck of a multiaxial GFRP laminate, the fatigue load level σ_{max} equalled 100 MPa that resulted a RF of 2.73.

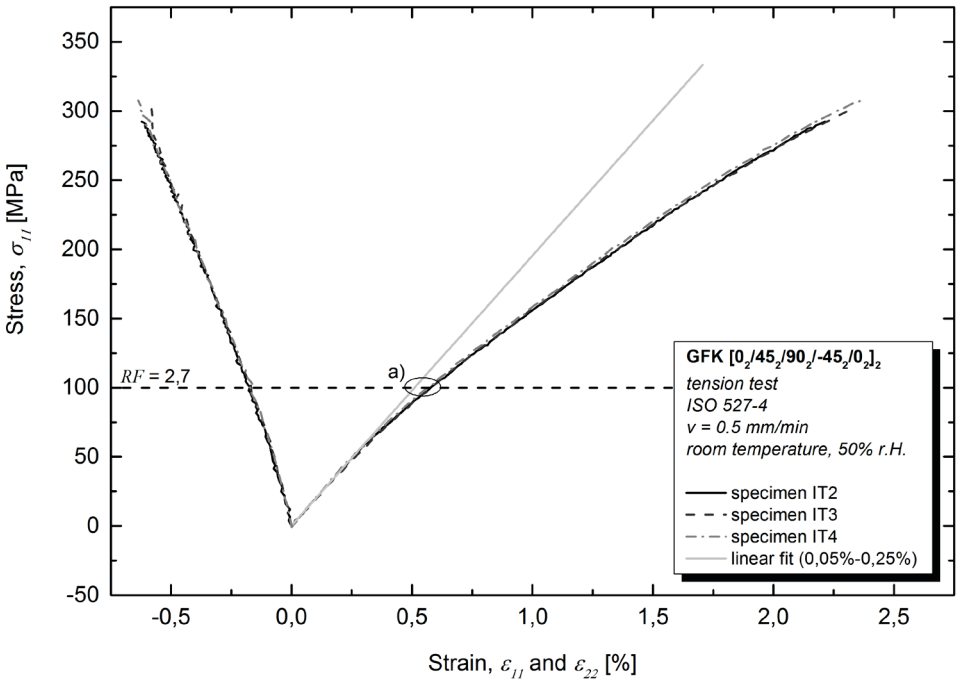

Fig. 4.15: Stress-strain curves of $[0°/45°/90°/-45°/0°]_2$ GFRP specimens, RF = 2.73 for static loads according to Puck's failure criterion, the quasi-static tensile test is according to ISO 527-4, strain was measured with DIC. A small deviation combined with moderate applied stress is indicated in a).

4.3 Fatigue tests

The aim of the tests was to combine meaningful fatigue data with online damage monitoring, in terms of a stiffness degradation that is measured in cyclic tensile tests during a tension-tension fatigue test. Furthermore, the suitability of Puck's criterion, which is designed for static loads, was considered for cyclic loads. Puck's criterion is implemented in common composite calculation software and could thus be wrongly used as indication for dynamic material design. The following figures include pictures of specimens; the pictures were taken during the fatigue tests and were scaled to the specimen's width. Specimen widths are usually 20 mm, except for 0° specimens; 0° specimens have a width of 10 mm.

Fibre angle of 0 degree to load direction

Specimen failure occurred near the end tabs, thus the number of cycles until failure is significantly lower than the expected number of cycles for this layup, as detailed in **Fig. 4.16**.

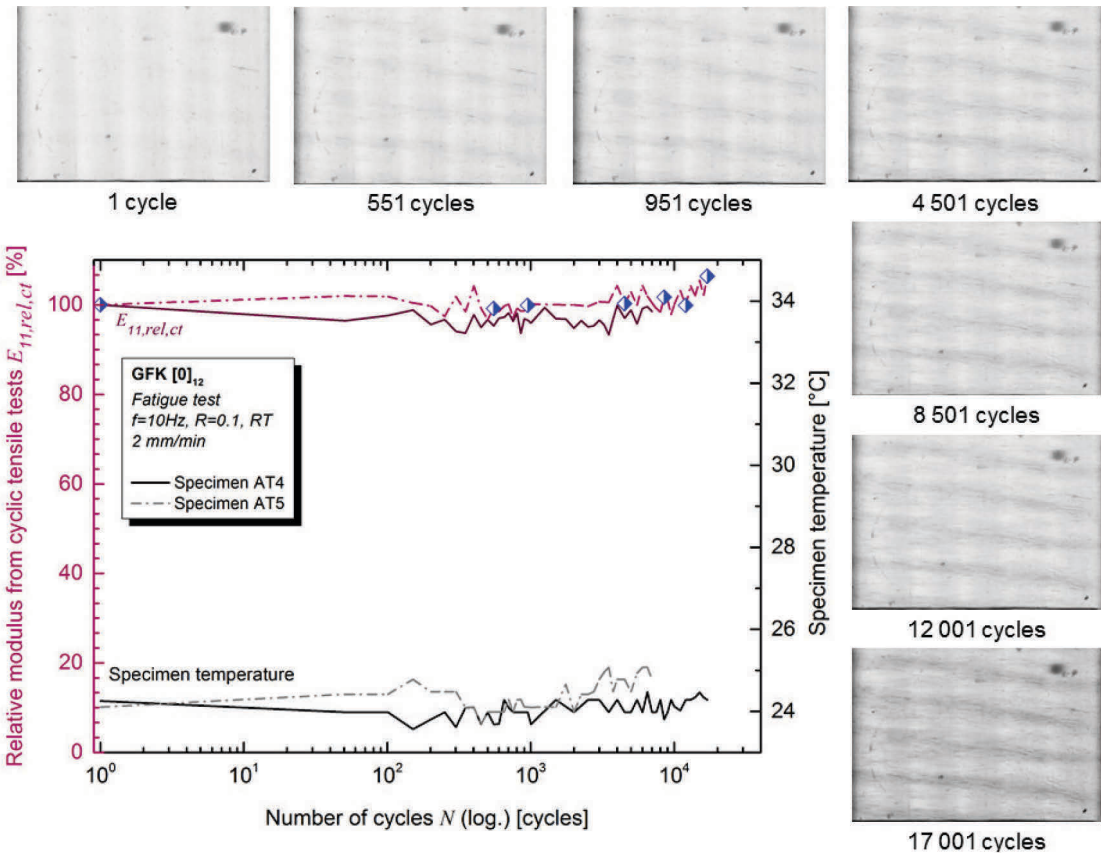

Fig. 4.16: Relative moduli calculated from cyclic tensile tests compared with the damage evolution in the glass fibre reinforced specimen, specimen failure near end tabs, $[0°]_{12}$ laminate, σ_{max} = 323 MPa, equals RF = 2 for static loads, R = 0.1, 2 mm/min in cyclic tensile tests.

As shown in **Fig. 4.16**, fine harmless cracks appeared in [0°] specimens. Those matrix cracks occurred in weft-fibre areas of glass fibre fabric, as detailed in **Fig. 4.17**. Crack accumulation in other areas was not observed. The fine matrix cracks in the weft-fibre areas were not critical for specimen failure; the multiaxial stress state at the clamps and at the end tabs caused the premature failure.

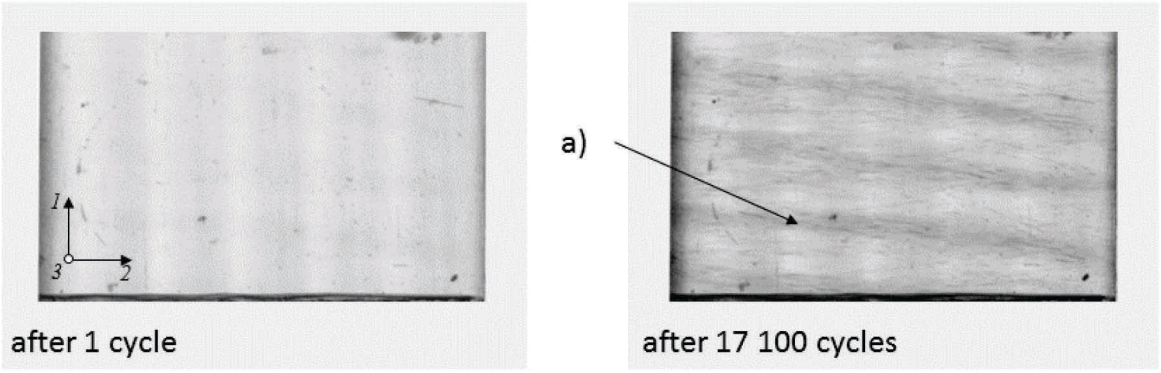

Fig. 4.17: Damage evolution in UD [0°] GFRP specimen displayed in detail, σ_{max} = 323 MPa equals RF = 2 for static loads, R = 0.1; a) saturated matrix cracks are found in weft-fibre areas of the unidirectional glass fibre fabric.

Fibre angle of 90 degree to load direction

Specimens with UD [90°] layup suffered a large number of cycles until failure (see **Fig. 4.18**). An expected slight reduction of the specimens modulus $E_{11,rel,ct}$ did not occur, due to the fracture near the end tabs. Crack initiation and crack growth were detected transversal to the load direction. A detailed view is given in **Fig. 4.19**. Similar to the transmitted light pictures of the [0°] layups, it was possible to separate fibres and matrix visually while using a computer monitor. It is difficult to distinguish between them in a printed version, due to the low contrast between the rovings and the matrix. However, surface scratches and imperfections on the surface did not initiate cracks. Those imperfections are clearly displayed in **Fig. 4.19a**. Surface scratches were found at the specimen's *21-plane* and were caused by the laminate manufacturing process and the specimen preparation. Even though the accurate sanding of the specimen's edges (*13-plane*), crack initiation was found from the specimen's edges (see **Fig. 4.19c**). Beside cracks from the specimen's edges, cracks were found that initiated from the middle of the specimen (see **Fig. 4.19b**).

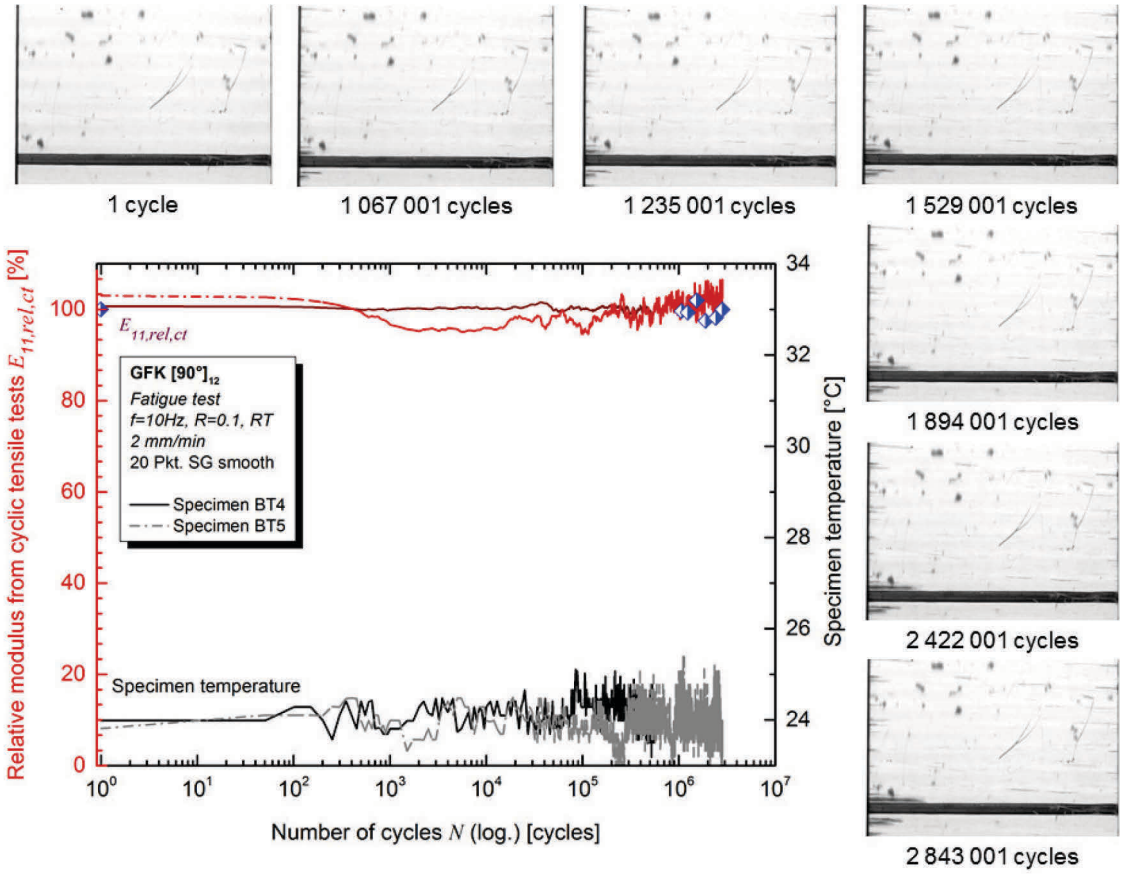

Fig. 4.18: Relative moduli calculated from cyclic tensile tests compared with the damage evolution in the glass fibre reinforced specimen, $[90°]_{12}$ laminate, specimen failure near cap strips, σ_{max} = 29 MPa equals RF = 2 for static loads, R = 0.1, 2mm/min in cyclic tensile tests.

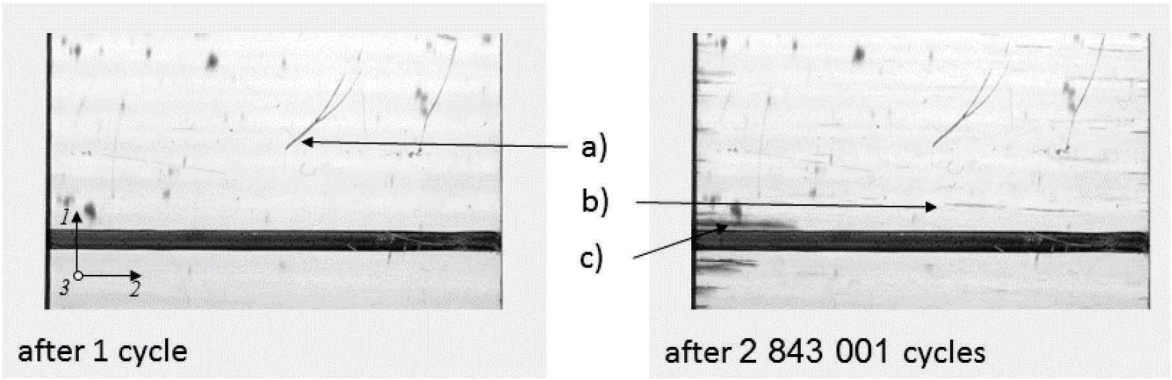

Fig. 4.19: Damage evolution in UD [90°] GFRP specimen displayed in detail, σ_{max} = 29 MPa equals RF = 2 for static loads, R = 0.1;
a) surface scratches caused by the specimen preparation;
b) growing matrix crack started from the middle of the specimen;
c) growing matrix crack started from the specimen's side.

Fibre angle of 45 degree to load direction

The modulus from cyclic tensile tests decreased continuously. Specimens with UD [45°] layup suffered a small number of cycles until failure. They fatigued within a range of 2.8 thousand cycles. The relative modulus from cyclic tensile tests over the number of cycles is displayed in **Fig. 4.20**. Damage evolution in a UD [45°] specimen during a fatigue test can also be observed in **Fig. 4.20**. Continuous crack growth was found in the entire specimen up to the CDS. The CDS occurred within the range of 2500 cycles. Until then, the modulus decreased by 23% of its initial value. After reaching the CDS, existing cracks grew in size until specimen failure. It may give the false impression that there are less cracks in the top left corner of the picture than in the bottom right corner, due to the fact that the cameras were not positioned perfectly parallel to the specimens surface. Transmitted light damage monitoring images are detailed in **Fig. 4.21**. It compares the slightly damaged specimen with the fatigued specimen. Crack accumulation was found near the rovings and within the rovings. Fibre bridging was observed when the specimen fatigued, as presented in **Fig. 4.21**.

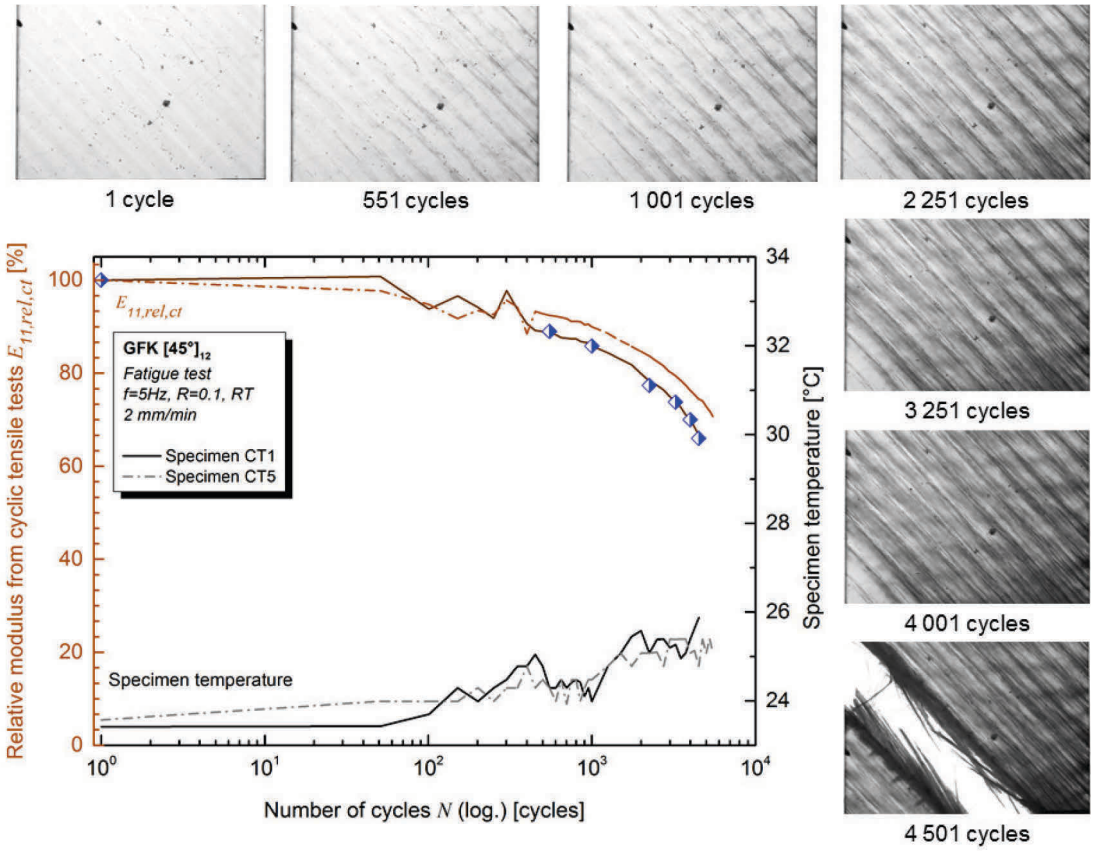

Fig. 4.20: Relative moduli calculated from cyclic tensile tests compared with the damage evolution in the glass fibre reinforced specimen, $[45°]_{12}$ laminate, σ_{max} = 65.5 MPa equals RF = 1.52 for static loads, R = 0.1, 2mm/min in cyclic tensile tests.

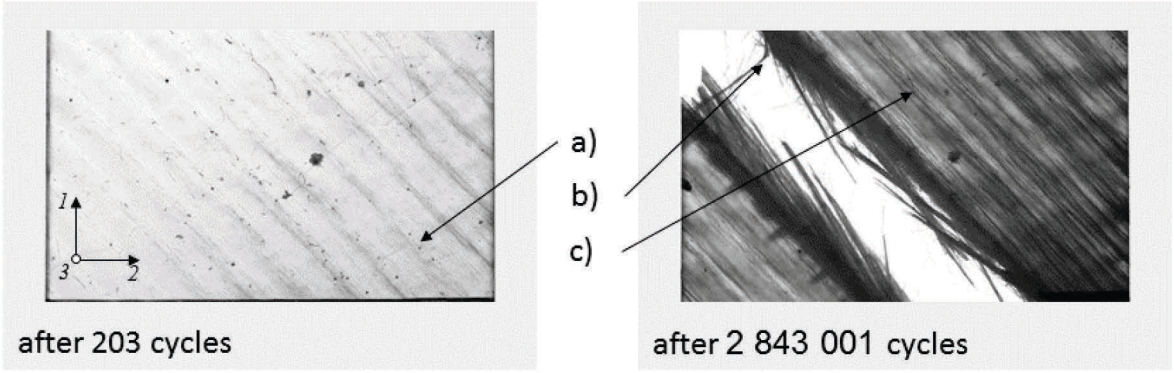

Fig. 4.21: Damage evolution in UD [45°] GFRP specimen displayed in detail, σ_{max} = 65.5 MPa equals RF = 1.52 for static loads, R = 0.1;
a) small matrix cracks near the rovings;
b) fibre bridging at the fracture area;
c) large cracks in the entire specimen.

Fibre angle of ±15 degree to load direction

Specimens with [±15°] layup had different damage mechanics than the previous discussed [45°] specimens. The damage monitoring showed that there is no crack initiation in the middle of the specimen and a CDS was not found. However, there is a delamination based damage mechanism. As evident from **Fig. 4.23**, delaminations began to grow from the specimen's sides during the fatigue test.

The delaminations grew continuously over approximately 500.000 cycles until specimen failure. Matrix cracks in the *12-plane* occurred shortly before failure (see **Fig. 4.23d**). The decrease of $E_{11,rel,ct}(N)$ led a few thousand cycles before the specimen fatigued to an increasing elongation, as detailed in **Fig. 4.22**. The little differences in $E_{11,rel,ct}(N)$ are based on the different initiation points of the main delaminations. In one case, the main delaminations started in the middle of the specimen (see **Fig. 4.23**), so that the end tabs did not hamper the delamination propagation. In the other case, the main delamination started to grow in the last quarter of the specimen; the end tabs limited the delamination propagation after 186.000 applied cycles. Thus, a second delamination started to grow. The damage monitoring of this second delamination is presented in **Fig. 4.22** and detailed in **Fig. 4.24**.

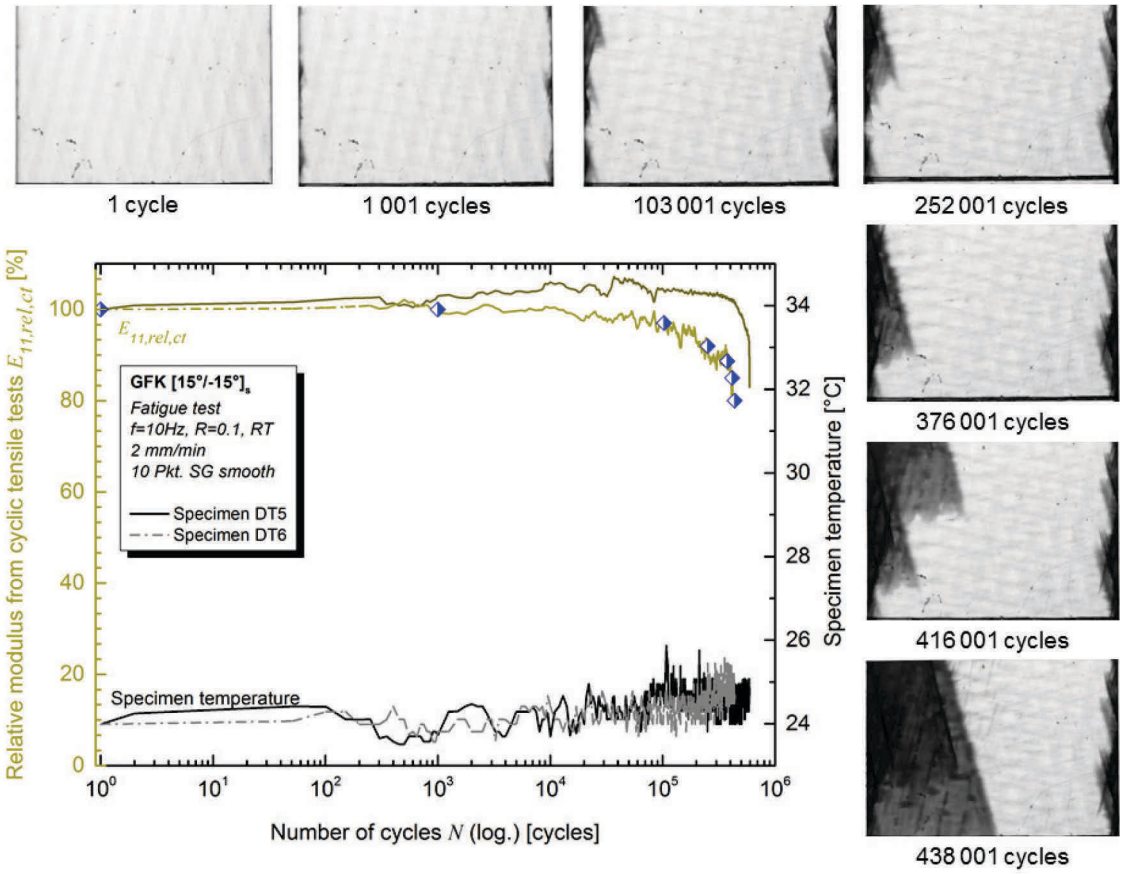

Fig. 4.22: Relative moduli calculated from cyclic tensile tests compared with the damage evolution in the glass fibre reinforced specimen, [15°/-15°]$_s$ laminate, σ_{max} = 202.9 MPa equals RF = 2 for static loads, R = 0.1, 2mm/min in cyclic tensile tests.

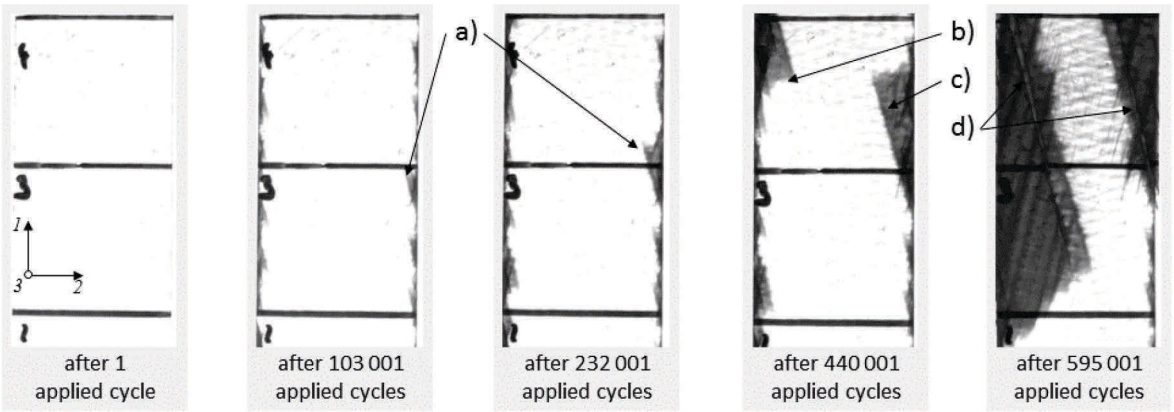

Fig. 4.23: Transmitted light damage monitoring of a glass fibre reinforced specimen during tension-tension fatigue test, [15°/-15°]$_s$ layup, specimen DT5, σ_{max} = 202.9 MPa equals RF = 2 for static loads, R = 0.1
a) delamination initiation and growth from the specimens sides
b), c) fast growing delaminations
d) large matrix cracks evolved in the delaminated areas.

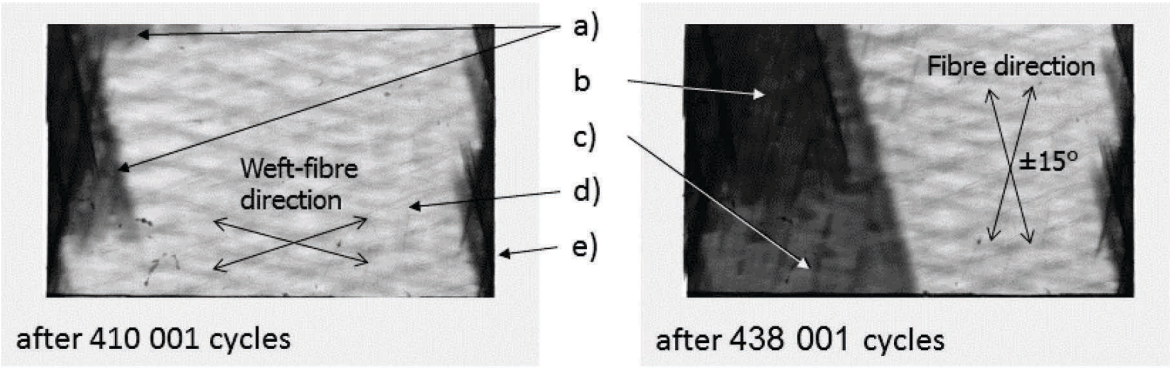

Fig. 4.24: Damage evolution in [15°/-15°] GFRP specimen DT6 displayed in detail, σ_{max} = 202.88 MPa equals RF = 2 for static loads, R = 0.1;
a) separately initiated delaminations;
b) growing delamination in a layer above the delaminations a);
c) delaminations have grown together right before specimen failure ;
d) saturated matrix cracks in weft-fibre areas of the unidirectional glass fibre fabric;
e) slow growing delaminations from the specimen's side.

Saturated matrix cracks in weft-fibre areas of the unidirectional glass fibre fabric of the [15°/-15°] specimen were found, as reported in **Fig. 4.24d**. Small cracks in weft-fibre areas developed a rhomboid crack pattern. Similar localized cracks in weft-fibre areas were found also in the [0°] specimens (compare **Fig. 4.17d** and **Fig. 4.24d**).

Fibre angle of 30/-30 degree to load direction

Specimens with [±30°] layup had very similar damage mechanics than the previous discussed [±15°] specimens. The damage monitoring showed, as it was in the case of the [±15°] specimens, that there is no crack initiation in the middle of the specimen. A CDS was not found. However, there is a delamination based damage mechanism, as shown in **Fig. 4.25**. Relative high numbers of applied cycles N were reached until specimen failure. The modulus $E_{11,rel,ct}(N)$ decreased continuously during the fatigue test. It dropped sharply, when the delamination propagation increased significantly. The continuously decreasing modulus (**Fig. 4.25**) in the fatigue test fits to the increasing deviation, of the stress from the linear fit of the modulus evaluation, in the stress-strain diagram (see **Fig. 4.10**).

A fatigued specimen is given in **Fig. 4.26**. Visible cracks, introduced by the end tabs, were found in [±30°] laminates. These cracks indicate the damaging impact of the multiaxial stress state at the end tabs.

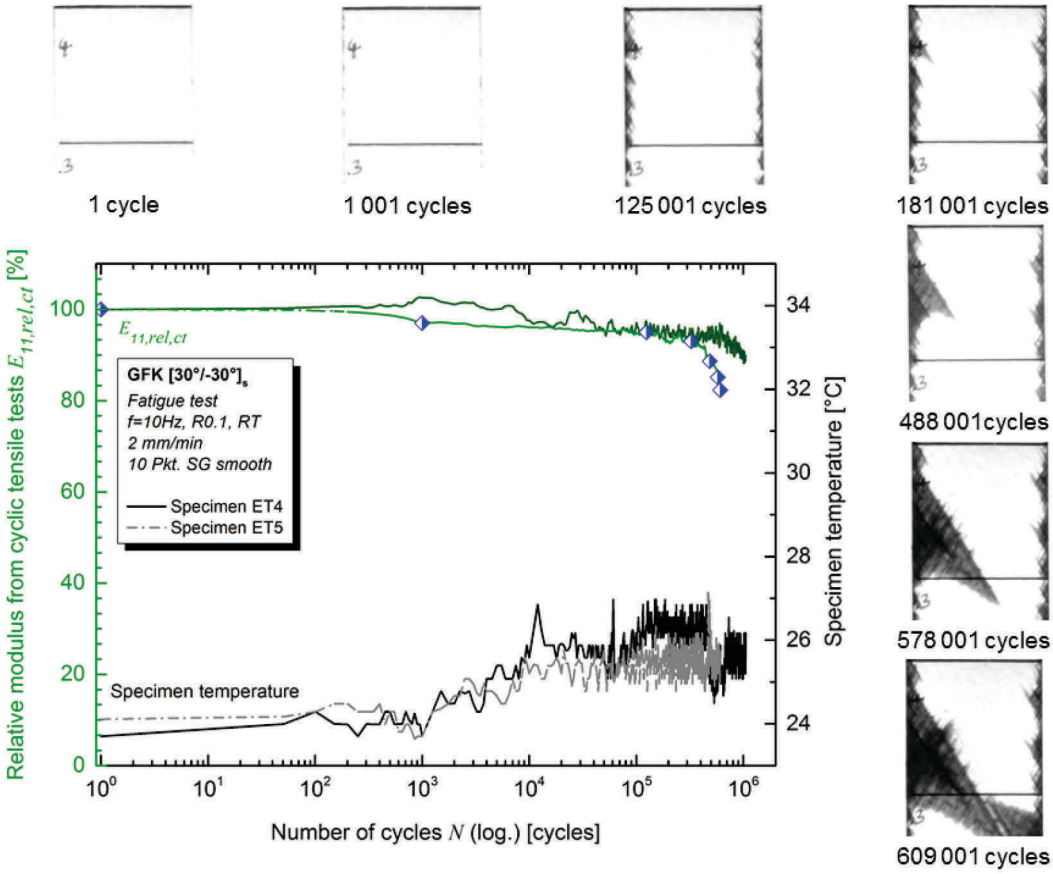

Fig. 4.25: Relative moduli calculated from cyclic tensile tests compared with the damage evolution in the glass fibre reinforced specimen ET5, $[30°/-30°]_s$ laminate, σ_{max} = 109 MPa equals RF = 2 for static loads, R = 0.1, 2mm/min in cyclic tensile tests.

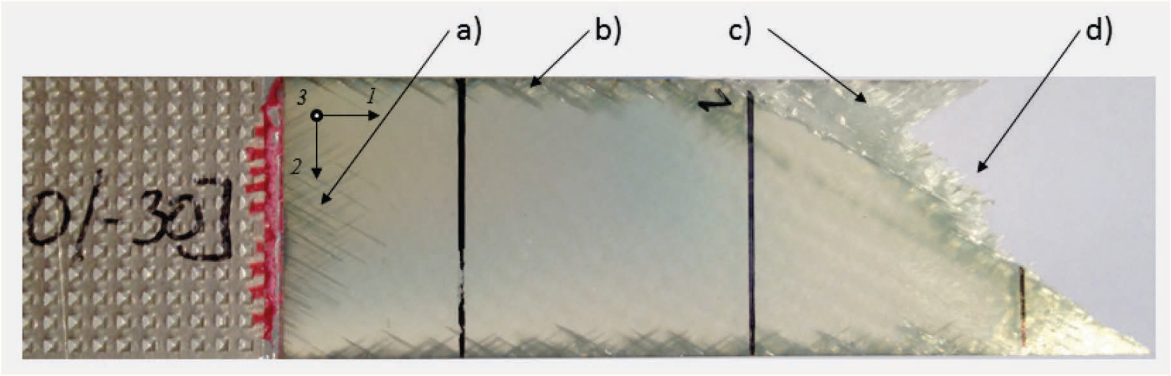

Fig. 4.26: Fractured glass fibre reinforced specimen ET4 after tension-tension fatigue test, [30°/-30°]s layup, specimen fatigued after 1.050.001 applied cycles, σ_{max} = 109 MPa equals RF = 2 for static loads, R = 0.1.
a) matrix cracks due to the multiaxial stress state at the end tabs
b) small delaminated areas, started at the specimen's edges
c) fracture surface: delamination in *12-plane*
d) fracture surface: fibre breakage.

Fibre angle of 45/-45 degree to load direction

Specimens with the [45°/-45°]s layup showed an explicit matrix crack initiated damage mechanism. Crack accumulation was found in the entire specimen. First cracks occurred within a range of 50 to 200 applied cycles. Delaminations in fibre direction occurred after the CDS and finally led to specimen failure, as evident in **Fig. 4.27**.

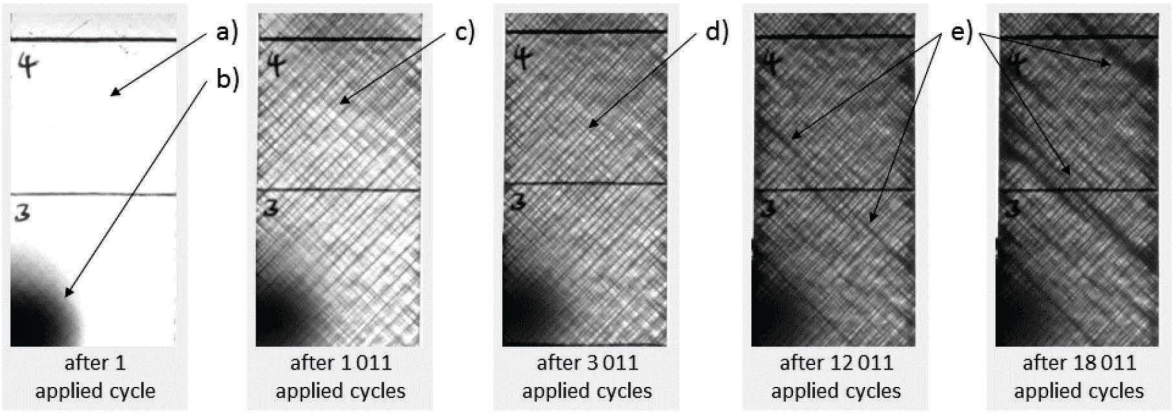

Fig. 4.27: Transmitted light damage monitoring of a glass fibre reinforced specimen during tension-tension fatigue test, $[45°/-45°]_s$ layup, specimen FT3, σ_{max} = 73.6 MPa equals RF = 2 for static loads, R = 0.1
a) undamaged specimen
b) shadow of the IR-camera
c) CDS at 1001 cycles
d) cracks (existed already at c)) were fully developed
e) growing delamination in fibre direction.

Saturated matrix cracks were not found in weft-fibre areas of the unidirectional glass fibre fabric, as shown for [0°], [15°/-15°]s and [30°/-30°] specimens. The CDS occurred after approximately 1000 cycles (visible in **Fig. 4.27c**). The mechanical properties decreased significantly at this point, as detailed in **Fig. 4.28**. The modulus $E_{11,rel,ct}(N)$ decreased to 85% of the initial value after approximately 1000 cycles. After 2000 cycles, the modulus $E_{11,rel,ct}(N)$ stabilized at approximately 75% of its initial value. Besides this modulus stabilisation, a sharp increase of the specimen's temperature was observed within the range of 2000 cycles. It is likely that the temperature increase was accelerated by the increased number of cycle between the cyclic modulus evaluations; the number of cycles between the modulus evaluations multiplied from 50 to 1000 cycles after 1000 applied cycles. Cyclic tensile tests are carried out at significantly lower strain rates (than cyclic tests) and my supported cooling of the specimen. The hysteretic heating is caused by friction due to a slight fibre orientation during the cyclic test.

Fig. 4.29 displays the undamaged and totally damaged specimen. A significant elongation due to the damage propagation is displayed in **Fig. 4.29d**.

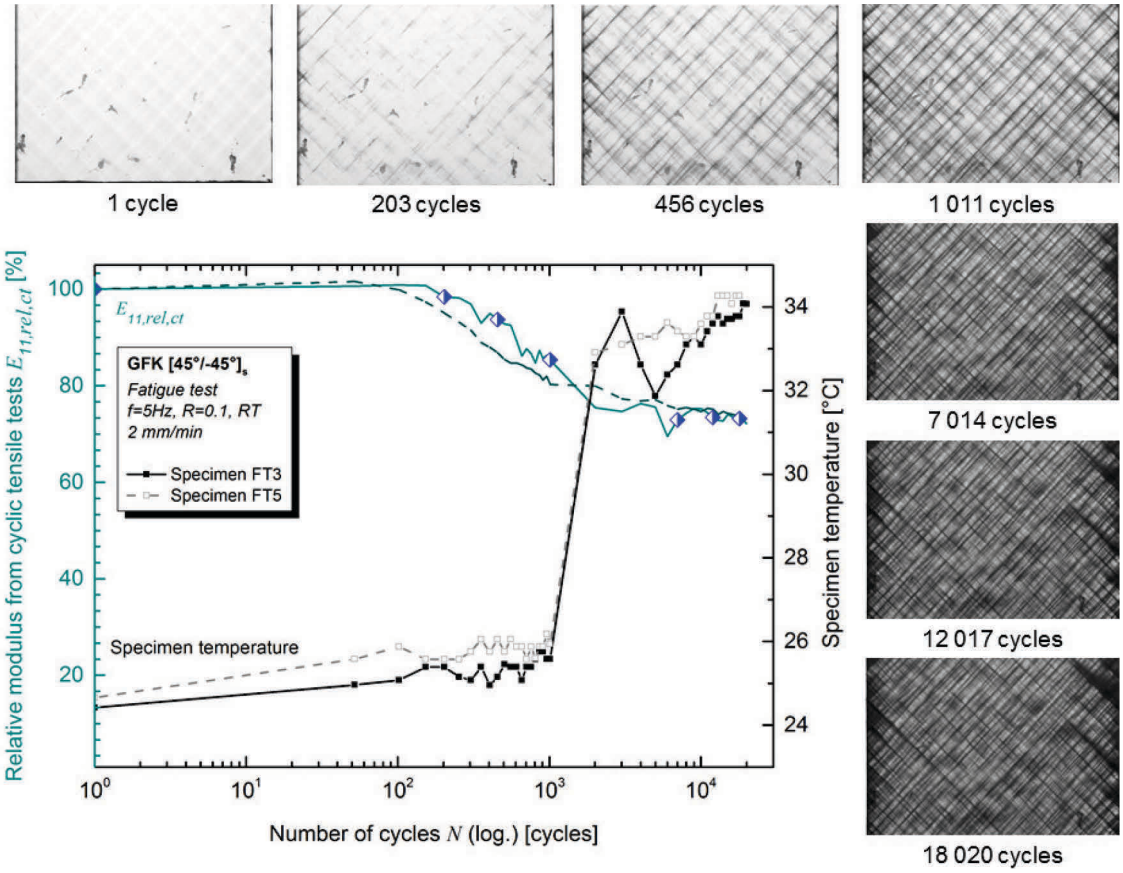

Fig. 4.28: Relative moduli calculated from cyclic tensile tests compared with the damage evolution in the glass fibre reinforced specimen, hysteretic heating, $[45°/-45°]_s$ laminate, σ_{max} = 73.6 MPa equals RF = 2 for static loads, R = 0.1, 2mm/min in cyclic tensile tests.

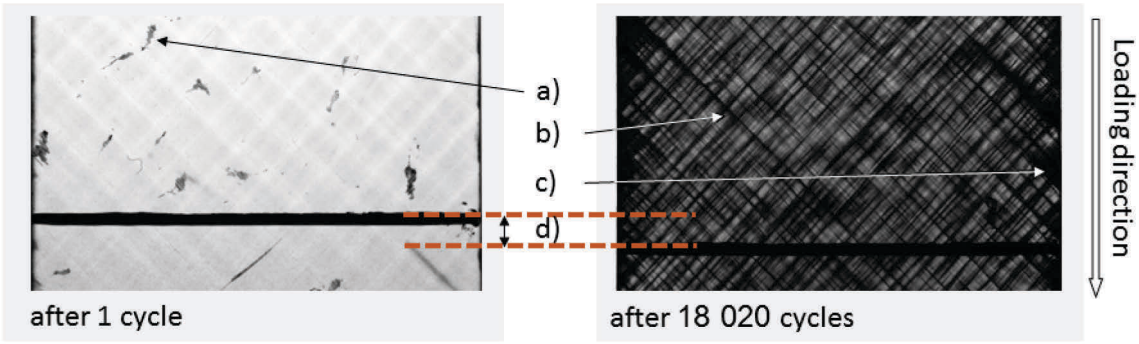

Fig. 4.29: Damage evolution in [45°/-45°]s GFRP specimen displayed in detail, σ_{max} = 73.6 MPa equals RF = 2 for static loads, R = 0.1;
a) manufacturing-caused surface imperfections;
b) large matrix cracks in the entire specimen;
c) small delamination at the specimens edges, introduced by crossing matrix cracks;
d) elongation at maximum strain shortly before failure, due to damage evolution.

Fibre angle of 60/-60 degree to load direction

Specimens with $[60°/-60°]_s$ layup showed, as it was observed in the case of [45°/-45°] specimens, evenly distributed matrix crack accumulation in the entire specimen. A matrix crack initiated damage mechanism is proved, as evident from **Fig. 4.30**. First cracks occurred after 100 applied cycles (N). The CDS occurred after around 1.000 cycles (see **Fig. 4.30**). Small delaminations initiated due to fully developed cracks after 2.173 cycles, as detailed in **Fig. 4.30**. Delaminations in fibre direction evolved at the end of fatigue life and caused specimen failure. An increase of the specimen's temperature was not observed, although the observed damage pattern was similar to the [45°/-45°] specimens, which showed a significant increase in temperature during the fatigue test.

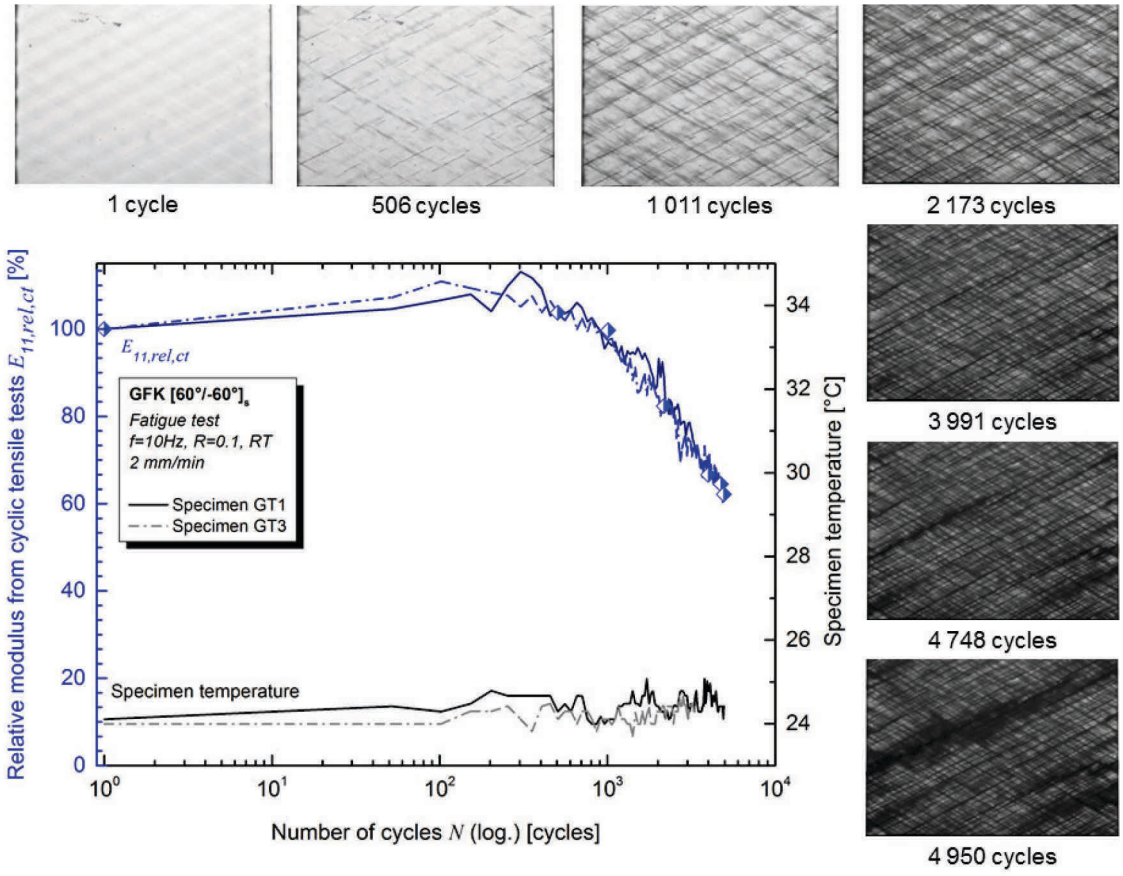

Fig. 4.30: Relative moduli calculated from cyclic tensile tests compared with the damage evolution in the glass fibre reinforced specimen, $[60°/-60°]_s$ laminate, σ_{max} = 50.4 MPa equals RF = 2 for static loads, R = 0.1, 2mm/min in cyclic tensile tests.

The modulus $E_{11,rel,ct}(N)$ decreased significantly after a few thousand cycles, as displayed in **Fig. 4.30**. It is likely that the quick fatigue is linked to the large deviation, of the stress-strain curve to the linear fit of the modulus evaluation (see **Fig. 4.12a**), in the stress-strain diagram and the relatively high applied stress. The fatigued specimen is displayed

in **Fig. 4.31**. It is distinguished between a continuously grown main delamination (**Fig. 4.31b**), and a sudden expansion of the delamination before fracture (**Fig. 4.31c**).

A less damaged area was found near the main delamination. Matrix cracks were not fully developed in this area.

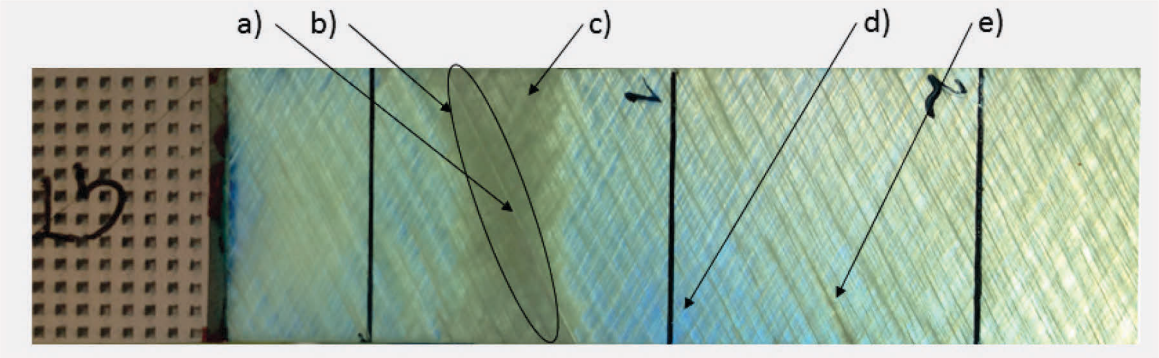

Fig. 4.31: Fractured glass fibre reinforced specimen GT3 after tension-tension fatigue test, $[60°/-60°]_s$ layup, specimen fatigued after 4950 applied cycles, σ_{max} = 50.4 MPa equals RF = 2 for static loads, R = 0.1;
a) large matrix crack through the delamination;
b) main delamination, presented in **Fig. 4.30**;
c) sudden expansion of the delamination at fracture;
d) less damaged area;
e) matrix crack induced evolving delamination.

Fibre angle of 75/-75 degree to load direction

Specimens with $[75°/-75°]_s$ layup showed damage mechanisms, which are different to the damage mechanisms of $[45°/-45°]_s$ and $[60°/-60°]_s$ specimens. In contrast to $[60°/-60°]_s$ specimens, no evenly distributed matrix crack accumulation was found in the entire specimen. A characteristic damage state was not found as well. However, matrix crack accumulation occurred in the specimen in a variously distributed way. Thus, a different matrix crack initiated damage mechanism is assumed, as indicated in **Fig. 4.32**. Single matrix cracks evolved through the entire layers. At the end of the fatigue life, there was a sharp decrease in modulus $E_{11,rel,ct}(N)$, as displayed in **Fig. 4.32**. It is assumed, that the stiffness degradation was caused by two cracks in the +75 layers (layers from the upper and lower specimen surface), so that load was carried only by the -75° layers at the end of the fatigue life. This caused an angle deviation of the fibres in the -75°, as detailed in **Fig. 4.33b**. Besides the angle deviation at the fracture zone, delaminations were observed near this area.

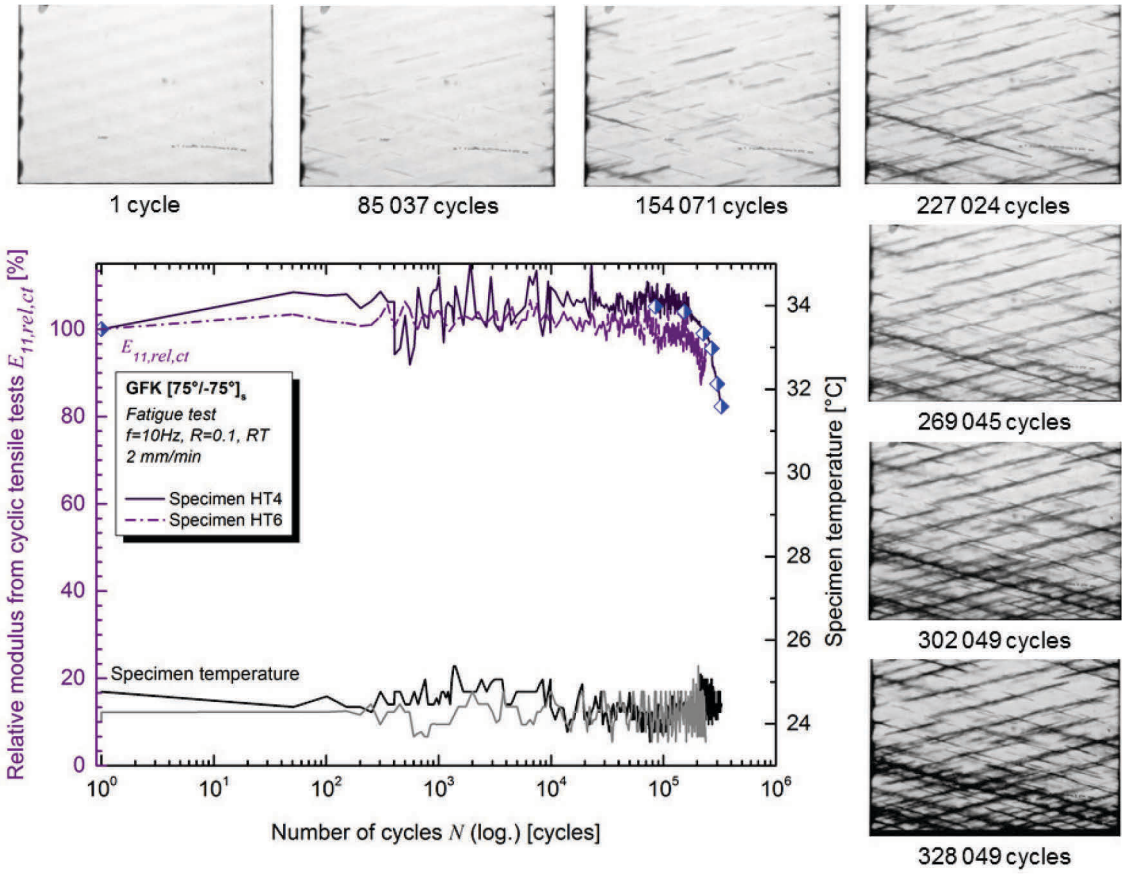

Fig. 4.32: Relative moduli calculated from cyclic tensile tests compared with the damage evolution in the glass fibre reinforced specimen, $[75°/-75°]_s$ laminate, σ_{max} = 40.1 MPa equals RF = 2 for static loads, R = 0.1, 2mm/min in cyclic tensile tests.

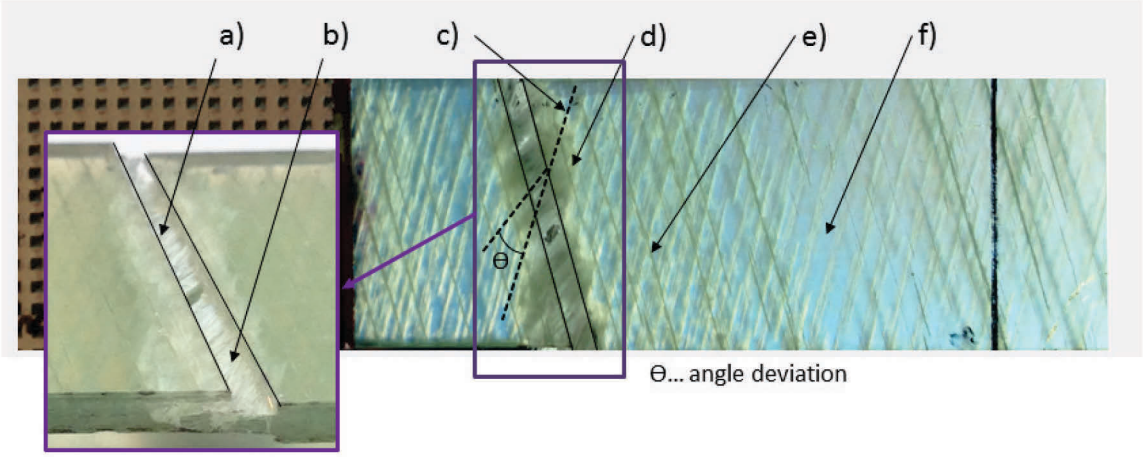

Fig. 4.33: Fractured glass fibre reinforced specimen after tension-tension fatigue test, specimen used for preliminary test, $[75°/-75°]_s$ layup, σ_{max} = 40.1 MPa equals RF = 2 for static loads, R = 0.1;
a) sharp crack in the +75° layer; b) fibre bridge in the -75° layer at the fracture zone;
c) original fibre angle
d) main delamination, equivalent to the delamination in **Fig. 4.31**;
e) large matrix cracks in fibre direction; f) less damaged area.

0 degree dominated multiaxial stacking sequence

Specimens with the $[0°/45°/90°/-45°/0°]_2$ layup showed a crack initiated damage mechanism. Crack accumulation was found in the entire specimen. First cracks in the 90° layer were observed within the first 10 applied cycles. After 4 552 cycles, cracks were reasonably saturated in the 90° layer and cracks in ±45° direction started to evolve. The observed crack accumulation in 45° and -45° layers is similar to the crack accumulation in the previous discussed [±45°]s specimens. CDS occurred after 87 200 cycles in ±45° and 90° plies. The modulus $E_{11,rel,ct}(N)$ decreased by 10% of its initial value, as can be seen in **Fig. 4.34**. First damage hotspots began to grow slightly after the CDS occurred. Growth of the damage hotspots, and their coalescence to delaminations, caused failure after around 330 000 cycles.

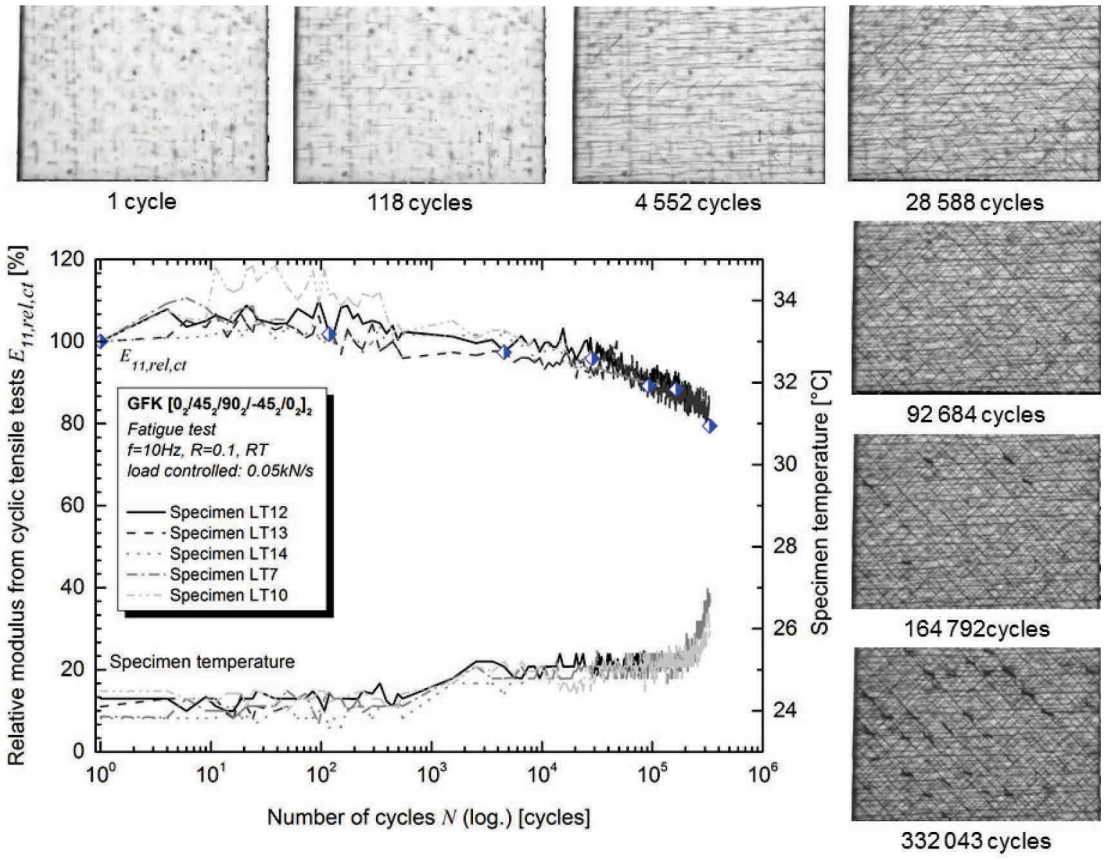

Fig. 4.34: Relative moduli calculated from cyclic tensile tests compared with the damage evolution in the glass fibre reinforced specimen, $[0°/45°/90°/-45°/0°]_2$ laminate, σ_{max} = 100 MPa equals RF = 2.73 for static loads, R = 0.1.

Comparison of the moduli degradations

There are three main groups of moduli courses, as seen in **Fig. 4.35**. The specimens of the first group (see **Fig. 4.35**a) fatigued within a range of fife- to twenty-thousand cycles in the tension-tension fatigue tests. They showed a strong decline of $E_{11,rel,ct}(N)$ as well. Those layups had a high applied stress and a significant deviation of the stress to the linear fit of the modulus evaluation (in the quasi static stress-strain curve at the applied maximum stress of the fatigue test), in common. The specimens of the second group (see **Fig. 4.35b**) fatigued much later. They had a moderate applied maximum stress, and a small deviation, of the stress to the linear fit of the modulus evaluation (in the quasi static stress-strain curve at the applied maximum stress of the fatigue test), in common. The modulus $E_{11,rel,ct}(N)$ of specimens of the third group did not decline during the fatigue test, and had the best fatigue performance, if they did not fracture in end tabs (see **Fig. 4.35c**).

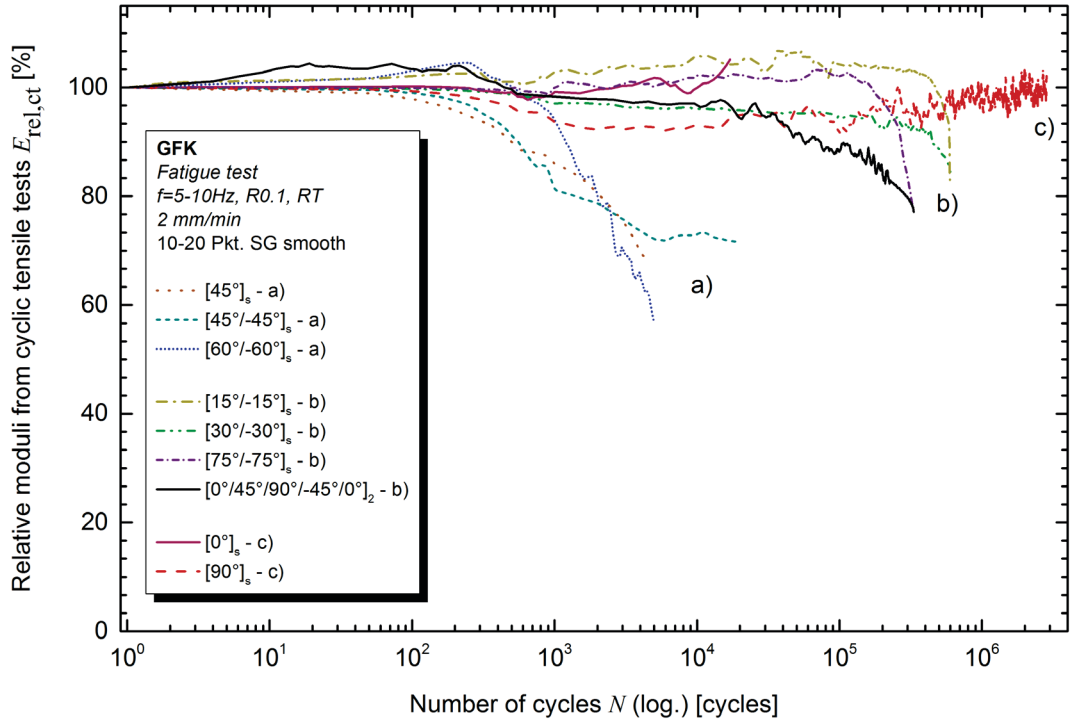

Fig. 4.35: Relative moduli calculated from cyclic tensile tests of glass fibre reinforced specimen with different layup, RF of 2 for static loads, except [45°]s and [0°/45°/90°/-45°/0°]$_2$ laminate, R = 0.1;
a) the fatigue load level was in the non-linear range of the stress-strain diagram;
b) the fatigue load level was near the linear range of the stress-strain diagram;
c) the fatigue load level was in the linear range of the stress-strain diagram.

A context concerning the lateral strain could not be found. **Fig. 4.35** illustrates, that various laminates, whose factors of safety for static loads equaled two, fatigued after

significantly different numbers of cycles. Thus, an RF for static loads does not to give any indication about the fatigue behavior of a composite. The fatigue load level itself is a better indication; if the fatigue load level is within the non-linear range of the stress-strain curve, the degree of non-linearity is inversely proportional to the fatigue life of a composite. It is likely that a fatigue load level within the non-linear range causes non-conservative deformations early.

4.4 Non-destructive testing

Six specimens with the multiaxial $[0_2|45_2|90_2|\text{-}45_2|0_2]_2$ stacking were tested in cyclic tension-tension tests. The tests were stopped at different damage states, as mentioned earlier. Excellent NDT results are already presented in the previous chapter, which are achieved in transmitted light damage monitoring combined with the measurement of the cycle-dependent linear elastic properties, according to Brunbauer et al. (2014). In this chapter, NDT results are presented from micro CT investigations, transmitted-light investigations and air-coupled UT investigations.

Micro CT inspections

The inner structure of the specimens is detected clearly and precisely, as evident from **Fig. 4.36**. Air voids are apparent and distinguishable from resin-rich areas. The detection of cracks, small delaminations and the damage hotspots is challenging. In this study, the detection of cracks were not possible. Cracks could have been detected using radio-opaque liquids, as recommended in Harris (2003).

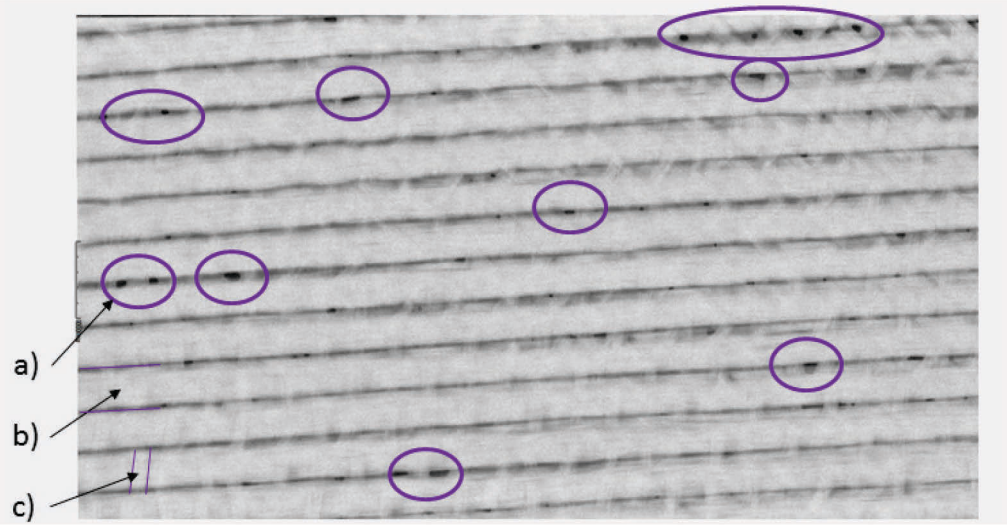

Fig. 4.36: micro CT investigation of a 0° ply of an undamaged specimen, air voids are marked; $[0°/45°/90°/\text{-}45°/0°]_2$ laminate;
a) air voids, b) roving c) weft fibres.

Medical CT inspections

The medical CT inspections failed, because the resolution of the medical CT is too low for small defects in the specimens.

Thermographic inspection

No data were submitted by the chair of automation at Montanuniversity Leoben (Austria). The inner structure and the damage, which occurred during the fatigue tests, were not detectable.

Water-coupled ultrasonic

No data were submitted by the TCKT GmbH (Wels, Austria), because they were not able to detect differences in the received ultrasonic signals of the damaged specimens compared to the undamaged specimen. These results do not correspond with the performance of water-coupled UT as described in literature (Harris 2003).

Air-coupled ultrasonic measurements

The results of the air-coupled ultrasonic measurements in transmission configuration are shown in **Fig. 4.37**. The interpretation is challenging, because the phase velocities of the undamaged specimen and the slightly damaged specimen after 60 cycles distinguish significantly. It is known that the phase velocity decreases with a decreasing modulus, and the modulus decreases with increasing damage. Therefore, the undamaged specimen should have the highest phase velocity and the fatigued specimen should have the lowest phase velocity. This was not the case, because the lowest phase velocity was measured at the undamaged specimen, although the highest phase velocity was expected. Thus, additional measurements with another four undamaged specimens were performed, to exclude a measurement error. The additional measurements are given in **Fig. 4.38**. The horizontal lines in **Fig. 4.38** represent the N-dependent phase velocities from **Fig. 4.37**.

A measurement error can be excluded, as the phase velocities of the addidional undamaged specimens are all within the same range. However, the additional measurements showed, that there is a specimen-depended scattering. Thus, a statement concerning the damage state in different specimens with different damage level could not be made.

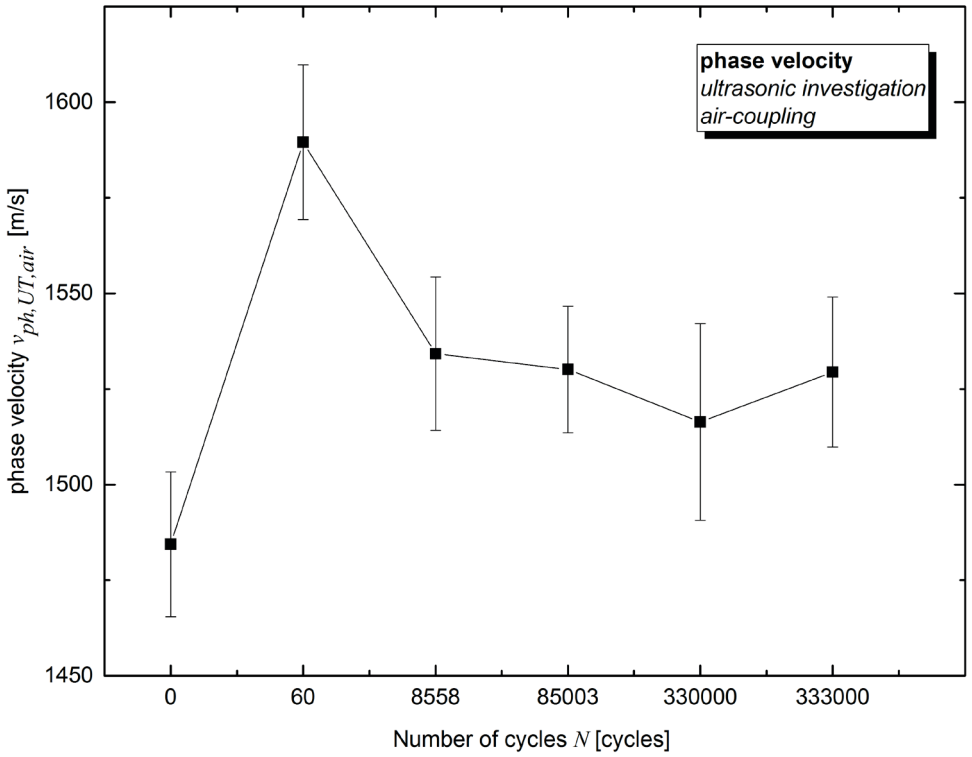

Fig. 4.37: Phase velocity of air-coupled ultrasonic measurements in transmission configuration, in relation to specimens with different damage states; specimen were damaged in cyclic tension-tension fatigue tests.

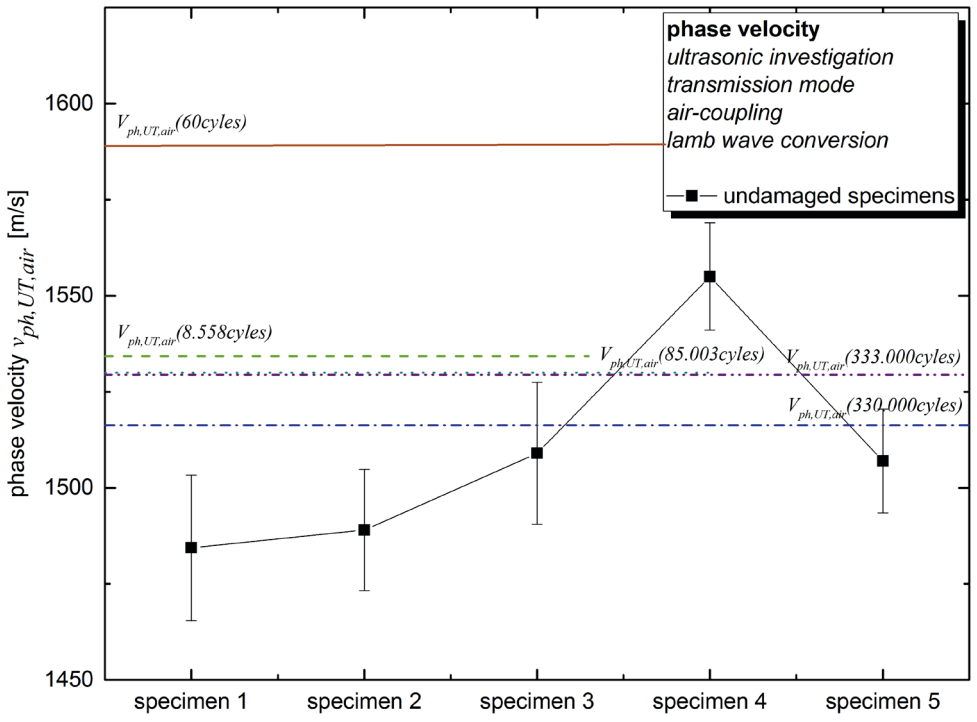

Fig. 4.38: Scattering of phase velocity of undamaged specimens, air-coupled ultrasonic measurements in transmission configuration.

Combination of NDT results

Specimens with the multiaxial $[0_2|45_2|90_2|\text{-}45_2|0_2]_2$ developed so called 'damage hotspots' at the end of the fatigue life (see **Fig. 4.34**). The growth of damage hotspots, and their coalescence to delaminations caused failure. Thus, the initiation and propagation of damage hotspots was investigated with a combination of various NDT methods.

The undamaged specimen with some manufacturing caused imperfection is displayed in **Fig. 4.39a**. Closer observation of the transmitted light damage monitoring records showed that damage hotspots occurred at crossing points of large cracks in 90° layers and large cracks in 45° or -45° layers, as indicated in **Fig. 4.39c**. The micro CT records with superimposed damage pattern reinforced this assumption; damage hotspots were always accompanied by cracks in the middle of a rowing in the 90° layers and ±45° layers (see **Fig. 4.39e** and **Fig. 4.39f**). However, not every crossing point of large cracks led to damage hotspots, but those with small manufacturing-caused imperfections, as shown in **Fig. 4.39a**. Thus, the manufacturing-caused imperfections were observed in detail.

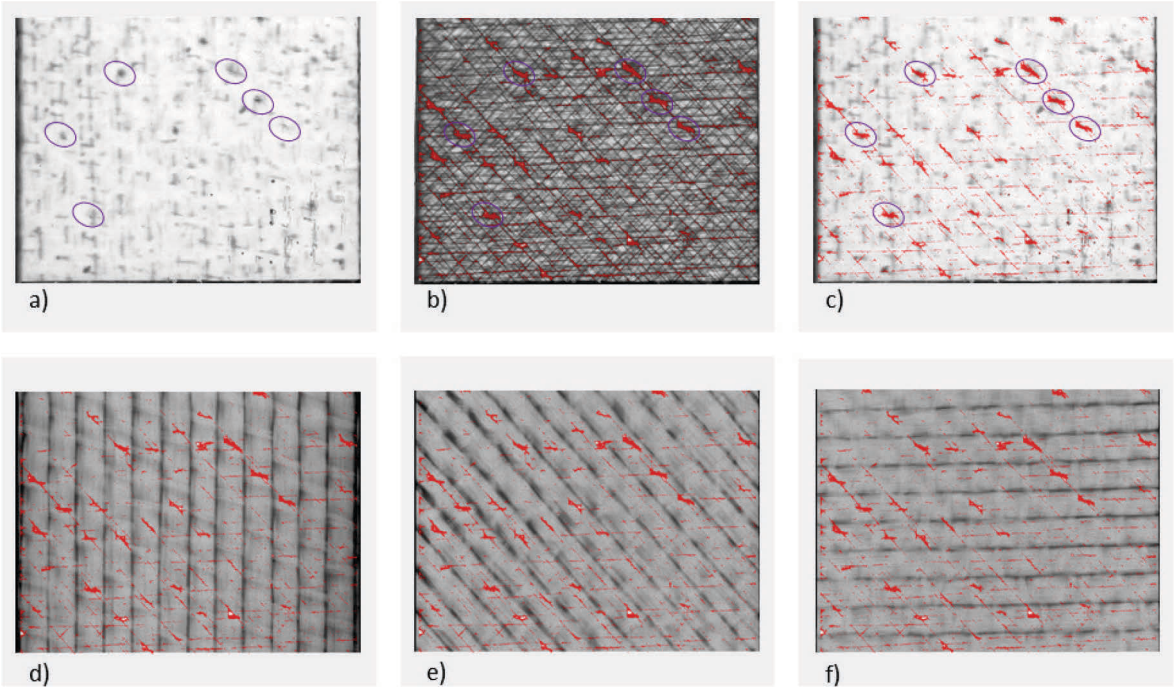

Fig. 4.39: Transmitted light damage monitoring combined with micro CT inspections, visualisation of the damage hotspots that led to specimen failure, $[0°/45°/90°/\text{-}45°/0°]_2$ laminate, specimen fatigued after 332 043 cycles in tension-tension fatigue test, σ_{max} = 100 MPa equals RF = 2.73 for static loads, R = 0.1;
a) transmitted light pictures of the undamaged specimen;
b) and c) transmitted light picture with superimposed damage-pattern of the fatigued specimen;
d), e) and f) micro CT pictures with superimposed damage-pattern.

In **Fig. 4.40** we compare the same damage hotspots, recorded with different analysis techniques. The informative value of each technique is limited. However, a defect classification is possible in combination of transmitted light investigations, micro CT and light microscopy. The transmitted light observation showed the crack accumulation in detail (see **Fig. 4.40a**). With this information, a damage pattern was created using Photoshop CS4. This damage pattern was superimposed with a micro CT record of the specimen's top 0° layer, as detailed in **Fig. 4.40b**. The position assignment was calibrated with air voids that were visible in transmitted light as well as in micro CT pictures. Based on the combination of micro CT record and the superimposed damage pattern, it is assumed, that the damage hotspots occurred between the weft-fibres and the rovings in load direction (see **Fig. 4.40b)**. The focal level of optical microscopy proved that the damage hotspots evolved near the specimen's surface, which is the 0° ply (see **Fig. 4.40c**).

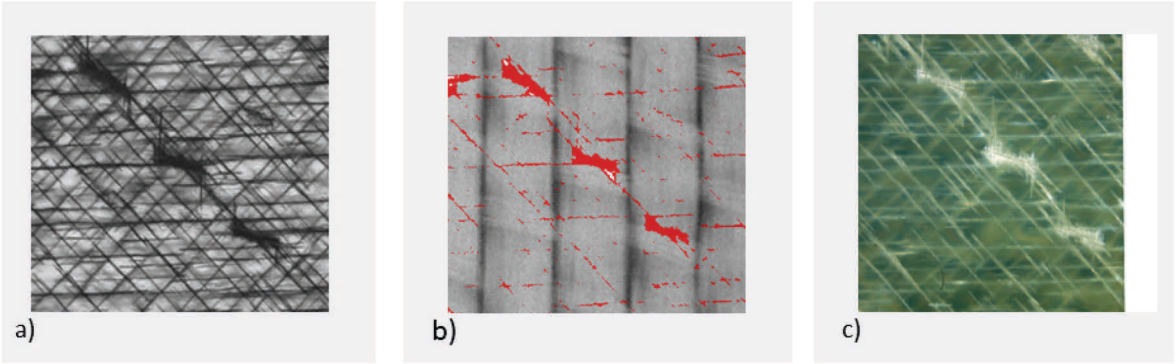

Fig. 4.40: Damage hotspots observed with a) transmitted light, b) micro CT and c) polarized transmitted light microscopy; $[0°/45°/90°/-45°/0°]_2$ laminate, specimen fatigued after 332 043 cycles in tension-tension fatigue test, σ_{max} = 100 MPa equals RF = 2.73 for static loads, R = 0.1.

Fig. 4.39e and **Fig. 4.39f** suggested, that large cracks in fibre direction occurred not between the rovings but within the rovings. To proof this assumption, the crack accumulation in the 90 degree plies was investigated in detail. Therefore, a damage pattern was derived after 13 000 cycles in the tension-tension fatigue test, due to the large cracks in 90° direction. The damage pattern was derived from the transmitted light investigations, which included these large cracks in the 90° plies and a starting crack accumulation in the ±45° layers. The transmitted light investigation is presented in **Fig. 4.41a**; the derived damage pattern is shown in **Fig. 4.41b**.

$[0°/45°/90°/-45°/0°]_2$ specimens consist of four 90° plies; in **Fig. 4.41**, there are for each ply micro CT records displayed. Each micro CT record is superimposed with the derived damage pattern. Therefore, large matrix cracks were found, which did not occur between rovings in any of the four analysed 90° layers; these cracks were marked. The marked cracks evolved within rovings of 90° plies.

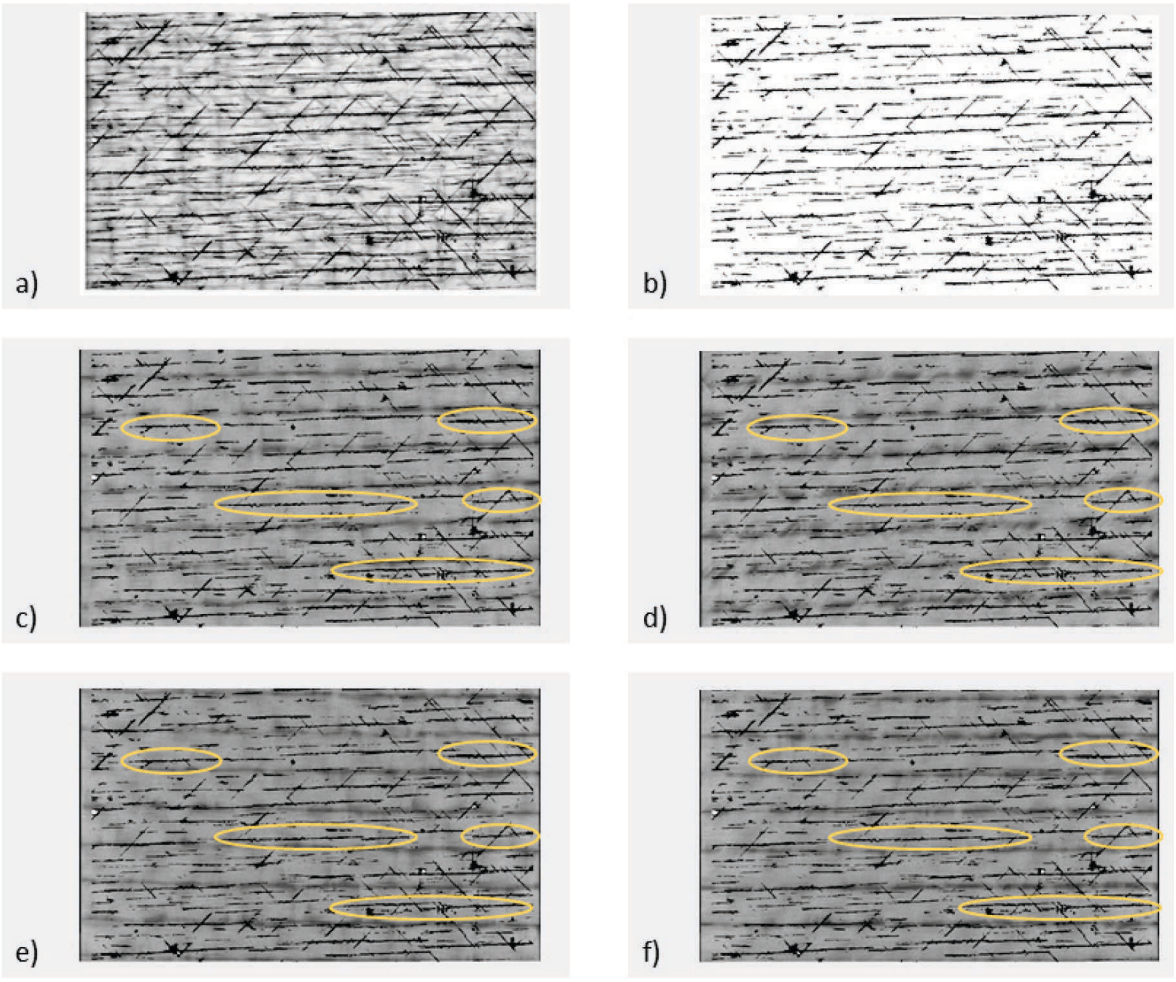

Fig. 4.41: Transmitted light damage monitoring combined with micro CT investigations to visualize crack propagation in the 90° layers; $[0°/45°/90°/-45°/0°]_2$ laminate; damage pattern after 13 000 cycles in tension-tension fatigue test, σ_{max} = 100 MPa equals RF = 2.73 for static loads, R = 0.1;
a) transmitted light investigation after 13 000 applied cycles;
b) derived damage-pattern;
c), d), e), f) micro CT pictures with superimposed damage-pattern of the specimen's four different 90° plies; cracks are marked, which did not occur between rovings.

5 SUMMARY, CONCLUSION AND OUTLOOK

In this study, semi-transparent GFRP laminates with various fibre angles were tested under cyclic loads in cyclic tension-tension tests. Therefore, unidirectional layups, biaxial layups from ±15° to ±75° in 15° steps and a 0° dominated multiaxial layup were manufactured using the vacuum pressing technology. These laminates were first tested under quasi-static conditions, to characterize their basic material properties. The material properties were used to calculate the fatigue load levels, which equalled an RF of two after Puck for each laminate. Fatigue-load-level-dependent cyclic tension-tension tests, combined with cyclic tensile tests and transmitted-light damage monitoring, were then performed to investigate the laminate's stiffness degradation caused by damage propagation. After the fatigue tests, six specimens with the 0° dominated multiaxial stacking were investigated with common NDT-methods to evaluate their applicability to damage monitoring during fatigue tests.

It was found that it is essential to be careful during the specimen manufacturing process and during the specimen preparation process. In some cases, imperfections on the specimen's surfaces may lead to premature specimen failure. This might be the case for 0° dominated multiaxial laminates, where damage-hotspots occurred at imperfections on the specimen's surface. These imperfections were identified as localized resin poor areas in weft fibres on the specimen's surface. Particularly in the case of biaxial laminates, preliminary tests showed that it is necessary to sand and polish the specimen's edges to prevent specimen-preparation-caused crack accumulation or delamination propagation from the edges.

Most notably, this is the first study to the knowledge of the author to investigate various laminate's fatigue behaviours related to fatigue load levels, which are calculated using Puck's approach for static loads. The results provide compelling evidence that various laminates, whose factors of safety for static loads equalled two, fatigued after significantly different numbers of cycles. Numbers of cycles until specimen failure range from $5 \cdot 10^3$ to $2 \cdot 10^6$. Thus, an RF for static loads does not to give any indication about the fatigue behavior of a composite.

Analyses of the calculated fatigue load levels indicate that there is a context between the degree of non-linearity in the stress-strain diagram at the fatigue load level and the fatigue life. When comparing the results from the cyclic tensile tests, three main groups

can be distinguished. Specimens of each group fatigued after almost the same numbers of cycles (see **Fig. 4.35**). Specimen, whose fatigue load level was within the non-linear range of the of the stress-strain curve, fatigued within a range of $5 \cdot 10^3$ to $20 \cdot 10^3$ cycles. Specimens, whose fatigue load level was close to the linear range the of the stress-strain curve, fatigued within a range of $3 \cdot 10^5$ to $6 \cdot 10^5$ cycles. Specimen, whose fatigue load level was within the linear range the of the stress-strain curve, fatigued after $2 \cdot 10^6$ cycles. A fatigue load level within the linear range of the stress-strain curve will yield (to the best knowledge of the author) the longest fatigue life. If, however, a fatigue load level has to be defined, the load level immediately before the range of non-linearity in the stress-strain curve can be an indicator for a still acceptable fatigue load level. Yes, this load level need to be verified in fatigue tests with an R-ratio, according to the intended purpose. For reliable material design of dynamically loaded components, the fatigue tests should be combined with cyclic tensile tests, to obtain information about the stiffness degradation during the fatigue life. This is especially necessary, if load-bearing components have to meet specific stiffness requirements.

Transmitted light online damage monitoring and cyclic tensile tests have shown that the stiffness degradation during a fatigue test is linked to damage propagation within the specimen. Different damage mechanisms were observed in various $[\pm\Theta]_s$ specimens. Damage mechanisms with crack accumulation, which develop a characteristic damage state (CDS), can be distinguished from delamination based damage mechanisms without CDS. Since the prediction of the fatigue behaviour is a recent research topic, the formation of different damage mechanisms are not implemented in current fatigue models. However, the damage evolution will have an influence on future fatigue life calculation models.

Based on high-resolution damage monitoring with transmitted light, the comparison to usual NDT-methods is disillusioning. Besides transmitted light investigations, micro-CT investigations promise results in a high resolution as well. Smallest size air voids were found within the specimens, due to the difference in density. Cracks and small delaminations were not found; this is a significant limitation for online damage monitoring. The water-coupled UT investigations failed, contrary to expectations. Since the water-coupled ultrasonic technique is widespread and various researchers published considerable results like Hillger and von Wachter (1991), delaminations in the fatigued specimen should have been found. The interpretation of the results from air-coupled

ultrasonic investigations is challenging, because the phase velocities of the undamaged specimen and the slightly damaged specimen contradicted each other.

The transmitted light technique in combination with semi-transparent GFRP is the only recommended approach for online damage monitoring in research issues. It delivers the best results and does not require a high level of investment costs. A limitation is the use of semi-transparent laminates.

6 REFERENCES

ISO 13003:2003 (EN), "Fibre-reinforced plastics — Determination of fatigue properties under cyclic loading conditions.

AVK - Industrievereinigung Verstärkte Kunststoffe e.V. (2015), "Der GFK-Markt Europa 2015.

BMW Group (6/10/2015), "Produktionsstart der neuen BMW 7er Reihe im Werk Dingolfing Klares Bekenntnis zum High-Tech-Standort Deutschland. Mehr als eine halbe Milliarde Euro Investitionen in neue, effiziente Produktionstechnologien am größten deutschen BMW Group Produktionsstandort. Integration von CFK- und Elektrifizierungskompetenz in die be-stehende Fertigungsinfrastruktur Technologietransfer von BMW i in Kernmarke BMW erfolgt, München.

Böhm, R., Hufenbach, W. (2010). Composites Science and Technology **70**, "Experimentally based strategy for damage analysis of textile-reinforced composites under static loading", S. 1330–1337. DOI: 10.1016/j.compscitech.2010.04.008.

Brunbauer, J., Arbeiter, F. et al. (2014), "Stiffness based fatigue characterisation of CFRP.", S. 166–171. DOI: 10.4028/www.scientific.net/AMR.891-892.166.

Brunbauer, J., Pinter, G. (2014). Polymer Testing **40**, "On the strain measurement and stiffness calculation of carbon fibre reinforced composites under quasi-static tensile and tension-tension fatigue loads", S. 256–264. DOI: 10.1016/j.polymertesting.2014.09.014.

Brunbauer, J., Pinter, G. (2015). Composites Part B: Engineering **70**, "Fatigue life prediction of carbon fibre reinforced laminates by using cycle-dependent classical laminate theory", S. 167–174. DOI: 10.1016/j.compositesb.2014.11.015.

Busse (2007), "Zerstörungsfreie Prüfung von Werkstoffen und Bauteilen Vorlesung, Universität Stuttgart, Stuttgart.

Carbon Composites e.V. (2015), "Composites-Marktbericht 2015 Marktentwicklungen, Trends, Ausblicke und Herausforderungen.

Döring, D. (2011), "Luftgekoppelter Ultraschall und geführte Wellen für die Anwendung in der Zerstärungsfreien Werkstoffprüfung Dissertation, Institut für Kunststofftechnik, Universität Stuttgart, Stuttgart.

Ehrenstein, G. W. (1995), "Mit Kunststoffen konstruieren Eine Einführung ; mit 33 Tabellen, Hanser, München, Wien.

Ehrenstein, G. W. (2006), "Faserverbund-Kunststoffe Werkstoffe, Verarbeitung, Eigenschaften, Hanser, München.

G. Slayter (1962). Scientific America, "Two-phase Materials.

GE Measurement & Control Solutions (2010), "X-ray inspections Computed tomography and 3D metrology. Online verfügbar unter http://www.ge-mcs.com/download/x-ray/phoenix-x-ray/GEIT-31104EN_2D_insp_CT_3D_metrology-brochure_12_10.pdf, zuletzt geprüft am 20160502.

Grellmann, W. Seidler, S. (2011), "Kunststoffprüfung, Hanser, München.

Haibach, E. (2006), "Betriebsfestigkeit Verfahren und daten zur bauteilberechnung, Springer, Berlin.

Harris, B. (2003), "Fatigue in composites Science and technology of the fatigue response of fibre-reinforced plastics, CRC Press; Woodhead, Boca Raton, Fla., Cambridge, U.K.

Helfen (2014), "Nichtlinearer Ultraschall zur Charakterisierung von Ermüdungsschäden während der Hochfrequenz-Beanspruchung von C-Faser-Kunststoffverbunden Dissertation, Universität des Saarlandes, Saarbrücken.

Henning, F. Moeller, E. (2011), "Handbuch Leichtbau Methoden, Werkstoffe, Fertigung, Hanser, München.

Hillger (2014), "Air-coupled Ultrasonic Testing-Method, System and practical Applications, 11th European Conference on Non-Destructive Testing.

Hillger, W., von Wachter (1991). Mat.-wiss. u. Werkstofftech. **22**, "Ultraschallprüfung an Faserverbundkunststoffen Grundlagen, Methoden der

bildhaften Darstellung und Ergebnisse", S. 217–224. DOI: 10.1002/mawe.19910220607.

Moser, K. (1992), "Faser-Kunststoff-Verbund Entwurfs- und Berechnungsgrundlagen, VDI-Verl., Düsseldorf.

Puck (1997). Materials and Corrosion **48**, "Festigkeitsanalyse von Faser-Matrix-Laminaten. Von A. Puck, 224 Seiten, Carl Hanser Verlag, München, Wien 1996, DM 128,00, ISBN 3-446-18194-6", S. 461. DOI: 10.1002/maco.19970480709.

Quaresimin, M., Carraro, P. et al. (2014). Composites Part B: Engineering **61**, "Damage evolution under cyclic multiaxial stress state: A comparative analysis between glass/epoxy laminates and tubes", S. 282–290. DOI: 10.1016/j.compositesb.2014.01.056.

Radaj, D. (2003), "Ermüdungsfestigkeit Grundlagen für Leichtbau, Maschinen- und Stahlbau, Springer, Berlin.

Reifsnider, K. L. (1991), "Fatigue of composite materials (R. B. Pipes,Series ed.), (Composite materials series, 4), Elsevier, Amsterdam, New York.

Rheinfurth, M., Schmidt, F. et al. (2011). Composites Science and Technology **71**, "Air-coupled guided waves combined with thermography for monitoring fatigue in biaxially loaded composite tubes", S. 600–608. DOI: 10.1016/j.compscitech.2010.12.012.

Schürmann, H. (2007), "Konstruieren mit Faser-Kunststoff-Verbunden, Springer-Verlag Berlin Heidelberg, Berlin, Heidelberg.

Steinberger, R., Valadas Leitao, T. et al. (2006). International Journal of Fatigue 28, "Infrared thermographic techniques for non-destructive damage characterization of carbon fibre reinforced polymers during tensile fatigue testing", S. 1340–1347.

Vassilopoulos, A. P. (2010), "Fatigue life prediction of composites and composite structures, Woodhead Publishing, Oxford.

APPENDIX

Table 7.1: Parameters evaluated in quasi-static tension and compression test in fibre direction.

Youngs modulus in fibre direction [GPa]	32.1
Elastic Poisson's ratio [-]	0.28
Ultimate tensile strength (UTS) [MPa]	644.4
Elaongation at UTS [%]	2
Tensile strength at 0.2% strain [MPa]	61.7
Ultimate compression strength (UCS) [MPa]	980.3
Elongation at UCS [%]	2.1
Compression strength at 0.2% strain [MPa]	103.7

Table 7.2 Parameters evaluated in quasi-static tension and compression test transverse to fibre direction.

Youngs modulus transverse fibre direction [GPa]	10.3
Ultimate tensile strength (UTS) [MPa]	57.9
Elaongation at UTS [%]	0.67
Tensile strength at 0.2% strain [MPa]	21
Ultimate compression strength (UCS) [MPa]	181.2
Elongation at UCS [%]	2.78
Compression strength at 0.2% strain [MPa]	26.8

Table 7.3 Quasi-static shear parameters evaluated in tension tests of ±45° specimens.

In-plane shear modulus [GPa]	12.5
In-plane shear strength [MPa]	108.4
In-plane shear strength at 0.2% strain [MPa]	27.5

Table 7.4 Quasi-static shear parameters evaluated in compression tests of ±45° specimens.

In-plane shear modulus [GPa]	14.4
In-plane shear strength [MPa]	158.6
In-plane shear strength at 0.2% strain [MPa]	32.5